

Search for the $B_s^0 \rightarrow \eta' \phi$ decay and prospects for the study of selected charmless B decays at LHCb

THÈSE N° 7955 (2017)

PRÉSENTÉE LE 15 SEPTEMBRE 2017
À LA FACULTÉ DES SCIENCES DE BASE
LABORATOIRE DE PHYSIQUE DES HAUTES ÉNERGIES 2
PROGRAMME DOCTORAL EN PHYSIQUE

ÉCOLE POLYTECHNIQUE FÉDÉRALE DE LAUSANNE

POUR L'OBTENTION DU GRADE DE DOCTEUR ÈS SCIENCES

PAR

Sebastiana GIANÌ

acceptée sur proposition du jury:

Prof. C. Hébert, présidente du jury
Prof. O. Schneider, Dr F. Blanc, directeurs de thèse
Prof. K. Trabelsi, rapporteur
Dr V. Vagnoni, rapporteur
Dr K. Vervink, rapporteuse



ÉCOLE POLYTECHNIQUE
FÉDÉRALE DE LAUSANNE

Suisse
2017

To my beloved uncle and grandpa.

Wherever you are now,
I hope I made you proud.

Abstract

This work explores charmless B decays using the LHCb detector. LHCb is one of the four main experiments at the Large Hadron Collider (LHC) located at CERN, and is designed to perform CP violation measurements and to study rare decays of hadrons containing b or c quarks. Among charmless B decays, the B_s^0 decay modes to final states with two light resonances (η , η' , ω , ϕ) are particularly interesting in view of time-dependent CP violation studies. More specifically they can be used to measure the CP-violating phase difference between the B_s^0 – \bar{B}_s^0 mixing amplitude and the $b \rightarrow s\bar{s}s$ decay amplitude. Among these, $B_s^0 \rightarrow \phi\phi$ has been exploited by LHCb through an angular analysis of the vector-vector final state. The other modes have lower measured or expected event yields, but don't require an angular analysis. We present the results of a search for the yet unobserved $B_s^0 \rightarrow \eta'\phi$ decay using 3 fb^{-1} of data collected by LHCb during the LHC Run 1 (2011–2012). The decay $B_s^0 \rightarrow \eta'\phi$ has been studied in several theoretical frameworks and the predictions for its branching fraction cover a wide range, typically from 0.05×10^{-6} to 20×10^{-6} .

In the analysis presented in this thesis the $B^+ \rightarrow \eta'K^+$ decay is used as normalisation in the computation of the branching fraction for the searched mode. The $B_s^0 \rightarrow \eta'\phi$ signal yield is obtained from a simultaneous two-dimensional fit of the reconstructed B and η' invariant masses of the $B_s^0 \rightarrow \eta'\phi$ and $B^+ \rightarrow \eta'K^+$ candidates in Run 1 data. No significant signal is found and, for the first time, an upper limit on the $B_s^0 \rightarrow \eta'\phi$ branching fraction is set:

$$\mathcal{B}(B_s^0 \rightarrow \eta'\phi) < 0.82 (1.01) \times 10^{-6} \quad \text{at 90\% (95\%) CL.}$$

Although large theoretical uncertainties make most predictions compatible with the result of this analysis, the upper limit is significantly smaller than the central values of most of the predictions, which tends to favour the lower end of the range of predictions.

Furthermore, prospect studies using the Run 2 data collected in 2015 and 2016, are presented for $B_s^0 \rightarrow \eta'\phi$ and for two other decay modes already studied with Run 1 data, $B_s^0 \rightarrow \eta'\eta'$ and $B^+ \rightarrow \phi\pi^+$. The $B^+ \rightarrow \eta'K^+$ and $B^+ \rightarrow \phi K^+$ decay modes are used as normalisation channels. The study shows that at least the full Run 2 dataset, to be collected until the end of 2018, will be needed to aim at an observation of the $B_s^0 \rightarrow \eta'\phi$ and $B^+ \rightarrow \phi\pi^+$ decays, taking into account also the wide range of predictions for these modes, while for the already established $B_s^0 \rightarrow \eta'\eta'$ decay the statistics collected by the end of Run 2 will allow a measurement of the B_s^0 lifetime.

Keywords: B physics, LHCb, LHC, charmless quasi-two-body B decays.

Résumé

Ce travail de thèse présente l'étude des désintégrations des mésons B en des particules non charmées, avec le détecteur LHCb. LHCb est l'une des principales expériences du grand collisionneur de hadrons (LHC) au CERN, destinée à mesurer la violation CP et étudier les désintégrations rares de hadrons contenant des quarks b ou c . Parmi les désintégrations des mésons B ne produisant pas de particules charmées, les désintégrations des mésons B_s^0 en deux résonances légères (η , η' , ω , ϕ) sont d'un grand intérêt pour l'étude de la violation CP dépendante en temps. Plus particulièrement, elles peuvent être utilisées pour mesurer le déphasage lié à la violation CP entre l'amplitude de mélange des états B_s^0 et \bar{B}_s^0 et l'amplitude de désintégration $b \rightarrow s\bar{s}$. La désintégration $B_s^0 \rightarrow \phi\phi$ a déjà été étudiée à LHCb par l'analyse angulaire de l'état final comportant deux mésons vecteurs. Les autres modes ont des taux d'événements mesurés ou prédits plus faibles mais ne requièrent pas d'étude par analyse angulaire. Nous présentons ici les résultats de la recherche de la désintégration $B_s^0 \rightarrow \eta'\phi$, en utilisant 3 fb^{-1} de données collectées par LHCb en 2011 et 2012 (Run 1). Diverses approches théoriques prédisent une large gamme de facteurs d'embranchement pour cette désintégration, allant de 0.05×10^{-6} à 20×10^{-6} .

Dans l'analyse présentée dans cette thèse la désintégration $B^+ \rightarrow \eta'K^+$ est utilisée comme normalisation pour le calcul du facteur d'embranchement de $B_s^0 \rightarrow \eta'\phi$. Le taux d'événements provenant des désintégrations de $B_s^0 \rightarrow \eta'\phi$, dans les données du Run 1, est obtenu par ajustement simultané d'un modèle sur les masses reconstruites des mésons B et η' des candidats des désintégrations $B_s^0 \rightarrow \eta'\phi$ et $B^+ \rightarrow \eta'K^+$. Aucun signal significatif n'est observé et, pour la première fois, une limite supérieure pour le facteur d'embranchement de $B_s^0 \rightarrow \eta'\phi$ est calculée :

$$\mathcal{B}(B_s^0 \rightarrow \eta'\phi) < 0.82 (1.01) \times 10^{-6} \quad \text{at 90\% (95\%) CL.}$$

Bien que le résultat soit compatible avec la plupart des prédictions, dû aux larges incertitudes théoriques, la limite supérieure est pourtant plus petite que la plupart des valeurs centrales prédites, favorisant ainsi la partie inférieure de l'intervalle des prédictions. De plus, les chances d'observer la désintégration $B_s^0 \rightarrow \eta'\phi$ avec les données du Run 2, ainsi que les désintégrations $B_s^0 \rightarrow \eta'\eta'$ et $B^+ \rightarrow \phi\pi^+$ déjà étudiées pour le Run 1, sont examinées en utilisant les données collectées en 2015 et 2016. Les désintégrations $B^+ \rightarrow \eta'K^+$ et $B^+ \rightarrow \phi K^+$ sont utilisées comme normalisation. Il résulte que toutes les données du Run 2, collectées jusqu'en 2018, seront nécessaire pour espérer observer les désintégrations $B_s^0 \rightarrow \eta'\phi$ et $B^+ \rightarrow \phi\pi^+$, en tenant compte

du large éventail des valeurs de facteur d'embranchement prédites, et permettront de mesurer le temps de vie du B_s^0 avec la désintégration $B_s^0 \rightarrow \eta'\eta'$.

Mots clefs : Physique du B , LHCb, LHC, désintégrations sans charme à deux corps.

Sommario

Questo lavoro di tesi esamina alcuni decadimenti *charmless* (senza la presenza del quark c) del mesone B usando il rivelatore LHCb. LHCb è uno dei quattro principali esperimenti al Large Hadron Collider (LHC) situato al CERN, ed è stato progettato per realizzare misure di violazione di CP e per studiare decadimenti rari di adroni contenenti i quarks b o c . Tra i decadimenti charmless del mesone B sono particolarmente interessanti i decadimenti del mesone B_s^0 in stati finali costituiti da due risonanze leggere ($\eta, \eta', \omega, \phi$), in vista di possibili studi di violazione di CP dipendente dal tempo. Più precisamente, questi decadimenti possono essere utilizzati per misurare la violazione di CP nella differenza di fase tra l'ampiezza di *mixing* $B_s^0-\bar{B}_s^0$ e l'ampiezza del decadimento $b \rightarrow s\bar{s}$. Tra questi modi di decadimento, $B_s^0 \rightarrow \phi\phi$ è stato studiato ad LHCb tramite un'analisi angolare dello stato finale vettore-vettore. Gli altri canali appartenenti a questa famiglia presentano un numero di eventi di segnale misurato o atteso di molto inferiore, ma d'altra parte non richiedono un'analisi angolare. Di seguito presentiamo i risultati della ricerca del decadimento $B_s^0 \rightarrow \eta'\phi$, fino ad oggi mai osservato, utilizzando i 3 fb⁻¹ di dati raccolti con il rivelatore LHCb durante il primo periodo di presa dati (Run 1) (2011–2012). Il decadimento $B_s^0 \rightarrow \eta'\phi$ è stato studiato con diversi modelli teorici che forniscono previsioni per la probabilità di diramazione in un ampio intervallo, da 0.05×10^{-6} a 20×10^{-6} .

Nell'analisi presentata in questa tesi, il decadimento $B^+ \rightarrow \eta'K^+$ è usato come canale di normalizzazione per il calcolo del rapporto di diramazione. Il numero di candidati di segnale del decadimento $B_s^0 \rightarrow \eta'\phi$ è ottenuto da un fit simultaneo in due dimensioni delle masse invarianti dei mesoni B ed η' . Poiché il numero di eventi ottenuto non è significativo, è stato calcolato un limite superiore per il rapporto di diramazione:

$$\mathcal{B}(B_s^0 \rightarrow \eta'\phi) < 0.82 (1.01) \times 10^{-6} \quad \text{at 90\% (95\%) CL.}$$

Le previsioni teoriche, affette da grandi incertezze, sono compatibili con questo risultato. Tuttavia il limite superiore ottenuto è significativamente più piccolo dei valori centrali delle previsioni, e sembra favorire i valori più piccoli nell'intervallo di queste ultime.

In aggiunta, questo lavoro di tesi esamina le prospettive future per lo studio del decadimento $B_s^0 \rightarrow \eta'\phi$ e di altri due canali, $B_s^0 \rightarrow \eta'\eta'$ e $B^+ \rightarrow \phi\pi^+$, già esaminati con i dati del Run 1. Lo studio, svolto utilizzando i dati raccolti nel 2015 e 2016 e usando come canali di riferimento i decadimenti $B^+ \rightarrow \eta'K^+$ e $B^+ \rightarrow \phi K^+$, mostra che sarà necessaria tutta la statistica disponibile alla fine del Run 2 (2015–2018) per una possibile osservazione dei decadimenti $B_s^0 \rightarrow \eta'\phi$ e

$B^+ \rightarrow \phi\pi^+$. Tale statistica permetterà inoltre una misura del tempo di vita media del mesone B_s^0 usando il decadimento $B_s^0 \rightarrow \eta'\eta'$.

Parole chiave: fisica del mesone B , LHCb, LHC, decadimenti charmless a due corpi.

Acknowledgements

This page is by far the most difficult to write as there are so many people who I wanted to thank. Firstly, I would like to thank my supervisor, Olivier Schneider, for always finding the time to check on the progress of my work, despite his many duties and commitments.

A big thanks goes to Fred Blanc, my co-supervisor. Thank you Fred for everything you taught me during these years. Despite my shyness, I always felt I could knock at your door and ask a question. Thanks for having always encouraged me and trusting my abilities, even when I didn't. Working with people so motivated and passionate about their work was a great opportunity.

Thanks to the entire LPHE group, to Tatsuya Nakada, for his challenging questions at the Monday meeting and the nice and interesting discussions during lunches, and to Aurelio Bay, for always being available for any kind of advice. I want also to thank Esther and Erika. The lab could not run so well without your priceless work.

A sincere thank you goes to Karim Trabelsi. It was an honor for me working with you. Thanks for having been my "highly qualified post-doc", a mentor, and at the very end, the external expert of the jury. Thanks for the endless amount of things that you taught me, for pushing me when needed, for having fun with me and of me, and for the long and nice discussions about physics and random topics.

Thanks to Guido Haefeli, for having guided me during the first year of work on hardware, and for all the nice conversations we had during these years. Thanks to Albert, Maurizio and Preema for being always available when I needed help on physics, computing or thesis writing and for the nice coffee breaks. Thanks to Mark Tobin, for his natural British humour and for having been my special english teacher, in particular during my first year at EPFL. Thanks to Jessica. Every time I needed any kind of advise or help, I know that I could count on her. Thanks to Zhirui, Violaine and Vincenzo, for being fantastic colleagues and for having shared a lot of nice moments during these four years. The LPHE lab consists of a big group of great people and I will miss each of them.

Thanks to my friends, the ones of an entire life and the fantastic UNICT group. Thanks for being a support in the hard times and for being always ready to have fun together during holidays.

Thanks to my family. Grazie mamma e papà, Lucy e Niki. Grazie per tutti i sacrifici, e per essermi stati vicini nei momenti difficili. Grazie alla mitica famiglia Gianì e alla sua roccia, nonno Meno. Sono consapevole di essere davvero fortunata. In questo anno difficilissimo per tutti noi, la vostra presenza e il vostro affetto non sono mai venuti meno.

Acknowledgements

Infine un grazie infinito a Giovanni, per aver condiviso ogni momento di questi quattro anni. Per aver gioito con me dei piccoli successi e per avermi incoraggiato quando pensavo di non potercela fare. Ma soprattutto per tutto l'amore che non ha mai smesso di donarmi.

Lausanne, 18 August 2017

Rita

Contents

Abstract (English/Français/Italian)	i
Acknowledgements	vii
Context and outline	1
1 Theory and phenomenology overview	3
1.1 The Standard Model of particle physics	3
1.2 Flavour sector and CKM matrix	5
1.2.1 Experimental knowledge of the CKM matrix elements	7
1.2.2 Unitarity triangles	7
1.3 CP violation	11
1.3.1 Direct CP violation	11
1.3.2 CP violation in mixing	11
1.3.3 CP violation in interference	12
1.4 Charmless B decays	12
1.4.1 $B_{(s)} \rightarrow (\phi, \eta', \eta) X$ decays	14
1.4.2 $B_s^0 \rightarrow \eta' \phi$ decays in the family $B_s^0 \rightarrow hh (h = \eta', \phi)$	15
2 LHCb detector	19
2.1 The Large Hadron Collider project	19
2.2 The LHCb experiment	20
2.3 Tracking system	23
2.3.1 The dipole magnet	24
2.3.2 Vertex Locator	24
2.3.3 Silicon Tracker	24
2.3.4 Outer Tracker	26
2.3.5 Track reconstruction	27
2.4 Particle identification systems	28
2.4.1 RICH detectors	28
2.4.2 Calorimeters	30
2.4.3 Muon system	32
2.5 Trigger	33
2.5.1 Hardware trigger (L0)	33

Contents

2.5.2	Software trigger (HLT)	34
2.5.3	Trigger in Run 2	35
2.6	Analysis software	36
2.7	Upgrade for Run 3	36
3	$B_s^0 \rightarrow \eta' \phi$ and $B^+ \rightarrow \eta' K^+$ selection	39
3.1	Selection strategy	39
3.2	Simulation	40
3.3	Trigger and preselection requirements	40
3.3.1	Trigger requirements	40
3.3.2	Stripping	41
3.3.3	Preselection	42
3.3.4	Particle identification requirements	43
3.4	Multivariate analysis	44
3.4.1	Input variables and data samples	45
3.4.2	Verifications on data-MC compatibility	47
3.4.3	BDT performance and optimization	47
3.5	Physics background studies	48
3.6	Multiple candidates and final sample size	54
3.7	Selection efficiencies	56
3.7.1	Breakdown of the efficiencies	56
3.7.2	PID efficiencies	58
3.7.3	Trigger efficiencies	58
3.7.4	Data-MC discrepancies	59
3.8	Efficiency ratio and systematic uncertainties	61
3.9	Expected yields	64
4	$B_s^0 \rightarrow \eta' \phi$ signal extraction and results	67
4.1	Maximum likelihood method	67
4.2	Fit model description	68
4.3	Fit model validation	71
4.3.1	Studies with fully simulated events	71
4.3.2	Validation with data	73
4.3.3	Fit validation using fast simulation	77
4.4	Search for the $B_s^0 \rightarrow \eta' \phi$ signal	81
4.4.1	Fit result	81
4.4.2	Fit systematic uncertainties	86
4.4.3	Branching fraction limit and final result	89
5	Prospects for $B \rightarrow \phi X$ and $B \rightarrow \eta' X$ modes	93
5.1	Simulation	94
5.2	Projection for $B^+ \rightarrow \phi h^+$ modes	94
5.2.1	$B^+ \rightarrow \phi h^+$ selection	95

5.2.2	$B^+ \rightarrow \phi K^+$ observed yield	98
5.2.3	$B^+ \rightarrow \phi \pi^+$ expected yield	100
5.3	Projection for $B_{(s)} \rightarrow \eta' X$ modes	102
5.3.1	$B^+ \rightarrow \eta' K^+$ observed yield	102
5.3.2	$B_s^0 \rightarrow \eta' \phi$ expected yield	104
5.3.3	$B_s^0 \rightarrow \eta' \eta'$ observed and expected yield	104
5.4	Discussion	105
 Conclusion		 109
 Bibliography		 111
 Curriculum Vitae		 119

Context and outline

The work presented in this thesis has been performed in the framework of the LHCb collaboration. After an introduction to the Standard Model, with a focus on flavour physics and charmless B decays, presented in Chapter 1 and a description of the experimental facility in Chapter 2, the rest of the thesis presents the work that has been the central part of my PhD studies, and for which I have performed all hands-on aspects.

Chapters 3 and 4 are dedicated to the description of the main analysis of my PhD work: the search for the yet unobserved $B_s^0 \rightarrow \eta' \phi$ decay. The analysis is performed using the pp collision data collected with the LHCb detector at 7 and 8 TeV centre-of-mass energies. The $B^+ \rightarrow \eta' K^+$ decay is used as normalisation channel in the computation of the $B_s^0 \rightarrow \eta' \phi$ branching fraction. Chapter 3 describes the strategy used in the selection and the efficiency computation for both modes while Chapter 4 describes in detail the technique used to extract the signal, the fit model, the uncertainty evaluation and the limit computation. The results obtained from this analysis have been published as an article in the Journal of High Energy Physics [1] and I had the opportunity to present them at a high-profile conference, the International Workshop on the CKM Unitarity Triangle, which took place in Mumbai in December 2016.

Chapter 5 aims at giving an overview of the future possibilities to study charmless B decays in LHCb with the data collected during the Run 2 data taking period (2015 – 2018). Using $B^+ \rightarrow \eta' K^+$ and $B^+ \rightarrow \phi K^+$, two well studied modes with large yields, projections are drawn for some of the rarest charmless modes for which the yield in Run 1 is either not significant or too small for further studies. Finally, a discussion on the results and on future prospects is given in the Conclusions.

This thesis describes a large fraction but not the totality of my contribution to the LHCb collaboration. During two years I served as trigger liaison, acting as a go-between for the Charmless physics working group and the Trigger group. During another year I contributed to the R&D studies for the scintillating fibre tracker that is now being constructed as part of the experiment upgrade and will be installed during the next LHC long shutdown, as described at the end of Chapter 2. In particular I have contributed to the characterisation of the first silicon photomultiplier prototypes testing their performance and their radiation hardness. Moreover I developed a fast simulation used to predict the detectors behaviour in various conditions. Part of this R&D work is described in the Technical Design Report for the LHCb Tracker Upgrade [2].

1 Theory and phenomenology overview

1.1 The Standard Model of particle physics

The Standard Model (SM) is the theory that describes the laws ruling the universe around us at low energy scales. This is done in terms of three forces (the weak, electromagnetic and strong interactions) and two categories of elementary particles, leptons and quarks, which are subjects to those forces.

The SM is a relativistic quantum field theory, and it can be considered as one of the great achievements of modern physics. Indeed, it gives a rather complete and experimentally well validated description of the fundamental nature of a wide variety of physics phenomena. This theory is symmetric under the local gauge transformations of the group $SU(3)_C \times SU(2)_L \times U(1)_Y$, where C denotes the generator of the colour charge, Y the generator of the weak hypercharge, and L the generator of the weak isospin. It includes three of the four fundamental interactions, the electromagnetic and weak interactions, unified in the electroweak interaction based on the $SU(2)_L \times U(1)_Y$ gauge group, and the strong interaction, described by the Quantum Chromodynamic (QCD) gauge field theory, corresponding to the symmetry group $SU(3)_C$.

The elementary constituents of matter are fermions, particles with half-integer spin, and are divided into leptons and quarks. There are three generations of fermions, each of which contains an up-type and a down-type quark, a charged lepton and a neutrino. Fermions of different generations have the same quantum charges but are characterised by different flavours. The properties of all those particles are summarized in Tables 1.1 and 1.2. To each particle corresponds an antiparticle with opposite charges. The interactions among fermions proceed through the exchange of spin-1 particles, named bosons, responsible for mediating the forces.

The electroweak theory includes a set of V-A (“vector minus axial-vector”) charged-current weak interactions, mediated by the W^\pm bosons that act only on left-handed fermions, a neutral weak interaction mediated by the Z^0 boson and a pure electromagnetic part, which is a parity-conserving interaction acting through photon exchange.

The $SU(3)$ gauge symmetry of QCD acts on triplets of quark fields, where the three components

Table 1.1 – Lepton properties: name, mass, electric charge and lepton flavours.

Lepton	Mass	Electric charge	L_e	L_μ	L_τ
e^-	$0.511 \text{ MeV}/c^2$	$-1e$	1	0	0
μ^-	$105.65 \text{ MeV}/c^2$	$-1e$	0	1	0
τ^-	$1777.03 \text{ MeV}/c^2$	$-1e$	0	0	1
ν_e	$< 3 \text{ eV}/c^2$	0	1	0	0
ν_μ	$< 0.19 \text{ MeV}/c^2$	0	0	1	0
ν_τ	$< 18.2 \text{ MeV}/c^2$	0	0	0	1

Table 1.2 – Quark properties: name, mass, electric charge, isospin and quark flavour.

Quark	Mass	Electric charge	Isospin (I_3)	Flavour
u	$1 - 5 \text{ MeV}/c^2$	$+\frac{2}{3}e$	$+\frac{1}{2}$	–
d	$3 - 9 \text{ MeV}/c^2$	$-\frac{1}{3}e$	$-\frac{1}{2}$	–
c	$1.15 - 1.35 \text{ GeV}/c^2$	$+\frac{2}{3}e$	0	Charm = +1
s	$75 - 170 \text{ MeV}/c^2$	$-\frac{1}{3}e$	0	Strangeness = –1
t	$174 \text{ GeV}/c^2$	$+\frac{2}{3}e$	0	Top = +1
b	$4.0 - 4.4 \text{ GeV}/c^2$	$-\frac{1}{3}e$	0	Bottom = –1

have different values of the colour charge. Eight massless gauge bosons, the gluons (g), are the mediators of the strong force, interacting only with the quark fields and by self-interaction. The SM also includes the BEH boson (better known as the Higgs boson), which generates masses for the fundamental particles. More precisely, the Higgs field is a two-component complex field that gives masses to the weak-gauge bosons through a spontaneous symmetry breaking (SSB), while keeping the photon massless. The Higgs field interacts with all the fermionic fields via the so-called Yukawa interaction. The Yukawa couplings may be large or small. The top quark Yukawa coupling is very large, of order one, which makes the top quark heavy. On the contrary, the Yukawa couplings with the neutrinos is almost zero, which keeps the neutrinos essentially massless.

The SM Lagrangian describing the theory can be written as

$$\mathcal{L} = \mathcal{L}_{\text{EW}} + \mathcal{L}_{\text{QCD}} + \mathcal{L}_{\text{Higgs}} + \mathcal{L}_{\text{Yukawa}}. \quad (1.1)$$

The first two terms describe the electroweak interaction and the strong interaction, respectively, while the $\mathcal{L}_{\text{Higgs}}$ and $\mathcal{L}_{\text{Yukawa}}$ terms give mass to the bosons and to the fermions, respectively.

The SM has a total of 26 independent parameters that need to be measured: the masses of the twelve fermions, eight parameters defining the quark and neutrino mixing matrices, coupling constants for the $SU(3)$, $SU(2)$ and $U(1)$ parts of the theory, two parameters relating to the Higgs field and one angle, θ_{QCD} , that sets the strength of CP (charge conjugation - parity) violation in the strong interaction. The measurements of θ_{QCD} indicate it is very small or zero,

but the SM offers no explanation of why this should be the case. This is the so-called strong CP problem.

The SM has been tested by a large number of precision measurements and proved to be a very precise theory of elementary particles and interactions. However, it is not able to explain all observations and there are still several questions that need an answer:

- How can gravity be incorporated in the SM?
- Several experimental evidences have lead to the hypothesis of the existence of the so-called “dark” matter. For instance it has been observed that the rotational speed of galaxies is so high that they could not hold together only thanks to the known matter. An extra mass, responsible for an additional gravity effect, is therefore needed to explain this phenomenon. This matter, which has an obscure behaviour and has not been directly detected so far (i.e. is invisible), is therefore called “dark”. What is its nature?
- The masses of the elementary fermions span from less than 1 eV to more than 10^{11} eV. Is there any mechanism producing this pattern (mass hierarchy problem)?
- Are the neutrinos Dirac fermions or Majorana fermions, i.e. distinct or identical to their antiparticles?
- Why is matter much more abundant than antimatter in the universe?

All these facts and questions tell us that the SM is an incomplete theory and can only be considered as an effective theory, i.e. an approximation at low energy of a more complete theory. Therefore it is necessary to look for new physics (NP) beyond the SM (BSM).

1.2 Flavour sector and CKM matrix

After this introduction on the basics of the SM, it is interesting to focus more deeply on the flavour sector of the SM and how new physics can manifest itself in this sector.

The flavour quantum numbers were introduced to explain the non-observation of some decays, allowed from the kinematical point of view. A quantum number is assigned to each generation of leptons, L_i ($i = e, \mu, \tau$), which is always conserved within the SM. Several other flavour numbers are introduced for hadrons: strangeness (s), charm (c), bottom (b) and top (t). Those are defined as the difference between the number of quarks of a certain flavour and the corresponding anti-quark, more precisely as $-(n_i - \bar{n}_i)$, for ($i = s, b$), and as $(n_j - \bar{n}_j)$, for ($j = c, t$).

In the SM only the weak interaction violates quark flavour conservation, and only when it is mediated by the charged W^\pm bosons. Measuring branching fractions of weak decays such as $\pi^+ \rightarrow \mu^+ \nu_\mu$ and $K^+ \rightarrow \mu^+ \nu_\mu$ suggested the existence of more than one coupling constant. Indeed if the coupling to the W boson would be the same for the $\bar{u}s$ (kaon decay) and the $\bar{u}d$ (pion decay) quark pairs, the difference in branching fraction could be accounted for by

phase-space effects. But the measured ratio between the semi-leptonic decay rates of the kaon and the pion is smaller than expected by an order of magnitude.

Nicola Cabibbo, in order to preserve the universality of weak interactions, suggested that the differences could arise from the fact that the doublets participating in the weak interactions are an admixture of the mass eigenstates. To describe this superposition of states, he introduced an angle, θ_C , commonly called the Cabibbo angle, such that mass eigenstates participating in the weak interaction are rotated with respect to the flavour eigenstates using the following matrix:

$$V_C = \begin{pmatrix} \cos\theta_C & \sin\theta_C \\ -\sin\theta_C & \cos\theta_C \end{pmatrix}. \quad (1.2)$$

The nature of V_C allowed to explain the suppression of flavour-changing neutral currents (FCNC) and historically has put the basis for the discovery of the charm quark [3].

In a six quark system, one angle is not sufficient to describe any rotation. Quark mixing can be generalised using a 3×3 unitary matrix [4], the so-called CKM matrix, from the names of Cabibbo, Kobayashi and Maskawa. In the case of three generations, there are 4 real parameters. Three of them can be interpreted as rotation angles in three dimensions (e.g. three Euler angles) and the fourth is an irreducible phase. Among the possible conventions, the standard way to parameterize the CKM matrix is:

$$V_{\text{CKM}} = \begin{pmatrix} V_{ud} & V_{us} & V_{ub} \\ V_{cd} & V_{cs} & V_{cb} \\ V_{td} & V_{ts} & V_{tb} \end{pmatrix} = \begin{pmatrix} c_{12}c_{13} & s_{12}c_{13} & s_{13}e^{-i\delta} \\ -s_{12}c_{23} - c_{12}s_{23}s_{13}e^{i\delta} & c_{12}c_{23} - s_{12}s_{23}s_{13}e^{i\delta} & s_{23}c_{13} \\ s_{12}s_{23} - c_{12}c_{23}s_{13}e^{i\delta} & -c_{12}s_{23} - s_{12}c_{23}s_{13}e^{i\delta} & c_{23}c_{13} \end{pmatrix}, \quad (1.3)$$

where $s_{ij} = \sin\theta_{ij}$, $c_{ij} = \cos\theta_{ij}$ and δ is the CP-violating phase. All the θ_{ij} angles can be chosen to lie in the first quadrant, so $s_{ij}, c_{ij} \geq 0$, and the mixing between two quark generations i and j vanishes if the corresponding angle θ_{ij} is equal to zero. In particular, in the case $\theta_{13} = \theta_{23} = 0$ the third generation would decouple and the CKM matrix would take the form of V_C in Eq. 1.2. Since the term s_{12} is small, it is possible to write the CKM matrix as an expansion of the parameter $\lambda = s_{12} \sim 0.22$ and three other parameters A , η and ρ , defined as

$$A = s_{23}/\lambda^2, \quad \rho = \cos\delta s_{13}/\lambda s_{23}, \quad \eta = \sin\delta s_{13}/\lambda s_{23}. \quad (1.4)$$

This expansion leads to the so-called Wolfenstein parametrization of the CKM matrix [5],

$$V_{\text{CKM}} = \begin{pmatrix} 1 - \frac{\lambda^2}{2} - \frac{\lambda^4}{8} & \lambda & A\lambda^3(\rho - i\eta) \\ -\lambda + A^2\frac{\lambda^5}{2}[1 - 2(\rho + i\eta)] & 1 - \frac{\lambda^2}{2} - \frac{\lambda^4}{8}(1 + 4A^2) & A\lambda^2 \\ A\lambda^3[1 - (1 - \frac{\lambda^2}{2})(\rho + i\eta)] & -A\lambda^2 + \frac{1}{2}A\lambda^4[1 - 2(\rho + i\eta)] & 1 - A^2\frac{\lambda^4}{2} \end{pmatrix} + \mathcal{O}(\lambda^6). \quad (1.5)$$

The parameters of the mixing matrix, which are among the free parameters of the SM, arise because the quark mass eigenstates are not identical to the eigenstates that interact by the weak interaction.

1.2.1 Experimental knowledge of the CKM matrix elements

The determination of the modulus of the CKM matrix elements is possible using several experiments, for which the difficulty increases moving from top left to bottom right of the matrix. Moreover the difficulty is increased by the fact that there is no such thing as a free quark. Among the nine elements, seven can be determined directly by tree-level processes:

- $|V_{ud}|$: nuclear beta decays, driven by the transition $d \rightarrow ue\bar{\nu}_e$ [6, 7];
- $|V_{cd}|$: neutrino interaction with matter leading to charm production ($\nu + d \rightarrow \mu + c$) [8, 9]. It is possible to use also semileptonic charm decays, using theoretical knowledge of the form factors [10, 11];
- $|V_{us}|$: semileptonic kaon decays such as $K \rightarrow \pi l \bar{\nu}$ ($s \rightarrow ul\bar{\nu}$ transitions) [12];
- $|V_{ub}|$: exclusive and inclusive semileptonic b -hadron decays ($b \rightarrow ul\bar{\nu}$ transitions) [13];
- $|V_{cs}|$: semileptonic D decays ($c \rightarrow sl\nu$ transitions) and leptonic D_s decays ($c\bar{s} \rightarrow l\nu$) [14, 15];
- $|V_{cb}|$: exclusive and inclusive semileptonic B decays with a charm quark in the final state ($b \rightarrow cl\bar{\nu}$) [13];
- $|V_{tb}|$: branching fraction of the $t \rightarrow Wb$ decay (assuming CKM matrix unitarity) [16, 17] or top-quark production cross-section [18, 19].

The V_{td} and V_{ts} elements are not measurable using tree-level processes. In order to determine their magnitude, experiments sensitive to one-loop diagrams are needed. The cleanest way to obtain them is to extract the quantity $V_{td(s)}^* V_{tb}$ from B (B_s^0) mixing processes, which are mediated by box diagrams where top quarks circulate as virtual particles.

It is an experimental fact that transitions within the same generation of quarks are ruled by V_{CKM} elements of order 1, while interactions between the first and second generations are suppressed by an order of magnitude; those between the second and third generations are suppressed by a factor 10^2 , and those between the first and third generations are strongly suppressed by a factor 10^3 . Figure 1.1 (left) shows a pictorial view of the hierarchy among the magnitudes of the matrix elements.

1.2.2 Unitarity triangles

The first important feature of the CKM matrix is its unitarity, with $V_{\text{CKM}} V_{\text{CKM}}^\dagger = V_{\text{CKM}}^\dagger V_{\text{CKM}} = \mathbb{1}$. Such a condition determines the number of free parameters of the matrix. The unitary imposes

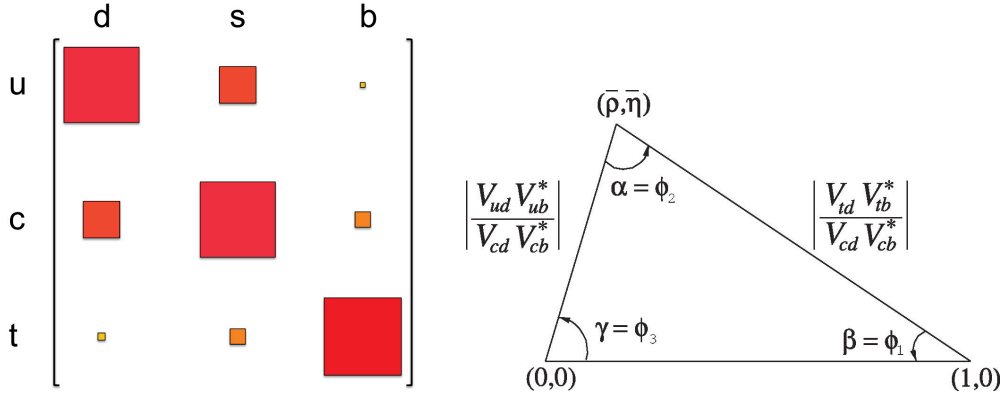


Figure 1.1 – Left: graphical representation of the CKM matrix elements. The area of the square is proportional to the element magnitude. The hierarchy in magnitude is expressed also through the colour scale, from red (bigger element) to yellow (smaller element). Right: unitarity triangle defined by Eq. 1.7 [13].

nine orthonormality conditions: three imply that the total probability of an up-type quark transition to any down-type quark is equal to one (weak universality). The other six conditions state that different rows (or columns) of the CKM matrix must be orthogonal. This leads to six equations:

$$V_{ud}^* V_{us} + V_{cd}^* V_{cs} + V_{td}^* V_{ts} = 0, \quad (1.6)$$

$$V_{ud}^* V_{ub} + V_{cd}^* V_{cb} + V_{td}^* V_{tb} = 0, \quad (1.7)$$

$$V_{us}^* V_{ub} + V_{cs}^* V_{cb} + V_{ts}^* V_{tb} = 0, \quad (1.8)$$

$$V_{cd}^* V_{ud} + V_{cs}^* V_{us} + V_{cb}^* V_{ub} = 0, \quad (1.9)$$

$$V_{td}^* V_{ud} + V_{ts}^* V_{us} + V_{tb}^* V_{ub} = 0, \quad (1.10)$$

$$V_{td}^* V_{cd} + V_{ts}^* V_{cs} + V_{tb}^* V_{cb} = 0. \quad (1.11)$$

These equations can be represented in the complex plane as triangles, but most of them include terms in which λ appears at different orders of magnitude and are therefore almost flat. Only two out of the six unitarity triangles have sides of the same order of magnitude: they are described by Eqs. 1.7 and 1.10. The triangle resulting from Eq. 1.7, known as “the unitarity triangle” (UT) or B^0 triangle, is illustrated in Fig. 1.1 (right). All triangles have the same area, equal to $J_{CP}/2$, where J_{CP} is the Jarlskog parameter quantifying the amount of CP violation due to SM weak interactions in the quark sector [20]. If there were no CP violation the elements of the CKM matrix would all be real implying the collapse of the triangles. If the CP symmetry is violated, $J_{CP} \neq 0$ as confirmed from the experimentally measured value $J_{CP} = (3.10_{-0.06}^{+0.05}) \times 10^{-5}$ [21]. The three internal angles of the UT are defined as

$$\alpha \equiv \arg\left(-\frac{V_{tb}^* V_{td}}{V_{ub}^* V_{ud}}\right) = \arg\left(-\frac{1 - \rho - i\eta}{\rho + i\eta}\right) + \mathcal{O}(\lambda^2), \quad (1.12)$$

$$\beta \equiv \arg\left(-\frac{V_{cb}^* V_{cd}}{V_{tb}^* V_{td}}\right) = \arg\left(-\frac{1}{1-\rho-i\eta}\right) + \mathcal{O}(\lambda^4), \quad (1.13)$$

$$\gamma \equiv \arg\left(-\frac{V_{ub}^* V_{ud}}{V_{cb}^* V_{cd}}\right) = \arg(\rho+i\eta) + \mathcal{O}(\lambda^2). \quad (1.14)$$

The three sides of the UT are normalised by the term $V_{cd}^* V_{cb}$. In terms of the Wolfenstein parameters, the coordinates of the triangle corners are $(0, 0)$, $(1, 0)$ and $(\bar{\rho}, \bar{\eta})$, where

$$\bar{\rho} = \rho\left(1 - \frac{\lambda^2}{2}\right) \quad \text{and} \quad \bar{\eta} = \eta\left(1 - \frac{\lambda^2}{2}\right). \quad (1.15)$$

The freedom to define the origin and the orientation of the triangle allows corners (or vertices) to fix two of the three apices, while the third one remains undetermined.

Precision measurements of each of the three angles and sides of the UT are fundamental in order to test the unitary condition of Eq. 1.7 by over-constraining it. If $\alpha + \beta + \gamma \neq 180^\circ$ or one of the sides is measured to be different from expectation, this would be a signature of NP.

The angle α (Eq. 1.12) can be accessed through tree $b \rightarrow u\bar{u}d$ decays. However the $b \rightarrow d$ penguin contribution can be sizable, which makes the determination of α complicated (e.g. $B^0 \rightarrow \pi^+\pi^-$). The precision on α is currently driven by measurements with $B^0 \rightarrow \rho^+\rho^-$ decays, where the angle is determined from the oscillation amplitude of the CP asymmetry as a function of the B^0 decay time. This information is combined with the determination of the branching fraction and CP violation of $B^0 \rightarrow \rho^0\rho^0$ and $B^+ \rightarrow \rho^0\rho^+$ (isospin analysis). The angle β (Eq. 1.13) can be measured using $B^0 \rightarrow J/\psi K^0$ ($b \rightarrow c\bar{c}s$) decays, where there is interference between the amplitude for a direct decay, $B^0 \rightarrow J/\psi K^0$, and the case when the B^0 meson has mixed before decaying, $B^0 \rightarrow \bar{B}^0 \rightarrow J/\psi K^0$. As with measurements of α , the value of β determines the oscillation amplitude of the time-dependent CP asymmetry. The angle γ (Eq. 1.14) does not depend on CKM elements involving the top quark, so it can be measured in tree-level dominated B decays. This is an important distinction from the measurements of the other two angles and implies that the measurements of γ are unlikely to be affected by physics beyond the SM. Its determination is performed with $B \rightarrow D^{(*)}K^{(*)}$ decays, whose transitions are mediated by V_{ub} and V_{cb} .

Equation 1.8 defines the B_s^0 unitarity triangle. One of its angles, denoted as β_s , is defined as [22]

$$\beta_s \equiv \arg\left(-\frac{V_{tb}^* V_{ts}}{V_{cb}^* V_{cs}}\right) = \lambda^2 \bar{\eta} + \mathcal{O}(\lambda^4) = -\frac{\phi_s}{2}. \quad (1.16)$$

This angle is very important since it is linked to the size of CP violation in the B_s^0 sector and to the parameter $\phi_s^{c\bar{c}s}$, which represents the phase difference between the B_s^0 mixing amplitude and the $b \rightarrow c\bar{c}s$ decay amplitude ($\phi_s^{c\bar{c}s} = -2\beta_s$ in the SM neglecting penguin contributions).

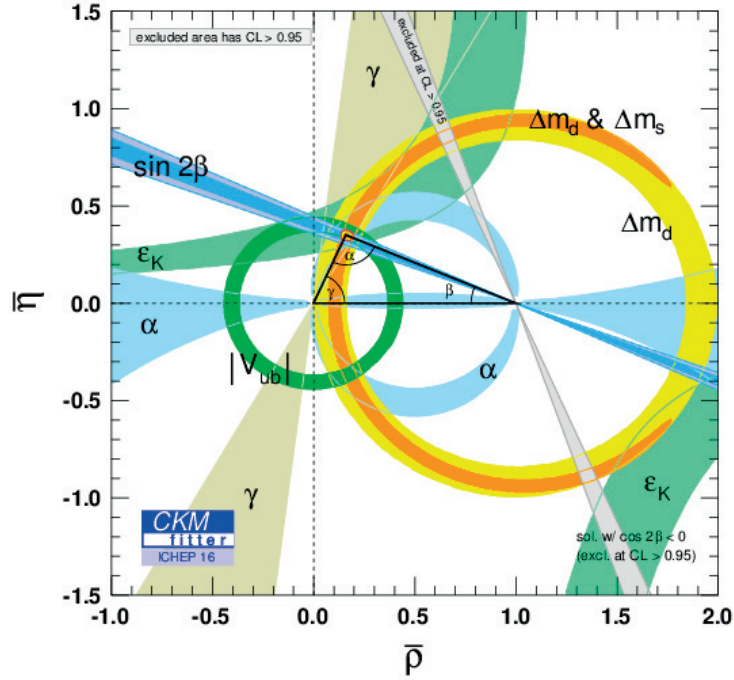


Figure 1.2 – Experimental constraints in the $(\bar{\rho}, \bar{\eta})$ plane. The tiny red hashed region represents the position of the triangle apex at 68% CL from the combination of all the constraints [21].

The CKM matrix elements can be determined with a high precision from a global fit of all the available measurements mentioned above and imposing the SM constraints such as the unitarity. The fit includes also theory predictions for the hadronic matrix elements (mentioned further in the text), which often present significant uncertainties. The experimental values obtained for the Wolfenstein parameters are

$$\lambda = 0.22496 \pm 0.00048, \quad A = 0.823 \pm 0.013, \quad \bar{\rho} = 0.141 \pm 0.019, \quad \bar{\eta} = 0.349 \pm 0.012, \quad (1.17)$$

while the fit results for the amplitudes of the nine CKM elements are

$$\begin{pmatrix} 0.97434^{+0.00011}_{-0.00012} & 0.22506 \pm 0.00050 & 0.00357 \pm 0.00015 \\ 0.22492 \pm 0.00050 & 0.97351 \pm 0.00013 & 0.0411 \pm 0.0013 \\ 0.00875^{+0.00032}_{-0.00033} & 0.0403 \pm 0.0013 & 0.99915 \pm 0.00005 \end{pmatrix}. \quad (1.18)$$

Figure 1.2 shows the experimental constraints on the $(\bar{\rho}, \bar{\eta})$ plane, i.e. the current knowledge of the UT triangle.

1.3 CP violation

Given any local Lagrangian field theory, the product of three transformations, the charge conjugation C (which changes any particle with its antiparticle), the parity P (which reverses the spatial coordinates) and the time-reversal T (which swaps initial and final states), known as CPT, is an exact symmetry. However CP, unlike CPT, can be violated. This phenomenon was observed for the first time in 1964 [23] and is linked to the presence of the complex phase δ in the CKM matrix (with a value different from 0 and π) as mentioned in the previous section. CP violation can manifest itself in three different ways:

- CP violation in the decay, or direct CP violation;
- CP violation in the mixing amplitude, or indirect CP violation;
- CP violation in the interference between the decay and mixing amplitudes.

1.3.1 Direct CP violation

CP violation in the decay, as opposed to the other two types that are specific to the neutral-flavoured meson systems, can occur also for charged mesons and for baryons. It appears as a difference in the rate between a given process and its CP-conjugate. CP violation in the decay is only possible if at least two amplitudes contribute. In case of exactly two amplitudes, the total amplitudes A and \bar{A} for the decay and its CP conjugate can be written as

$$\begin{aligned} A &= a_1 e^{i\phi_1} e^{i\delta_1} + a_2 e^{i\phi_2} e^{i\delta_2}, \\ \bar{A} &= a_1 e^{-i\phi_1} e^{i\delta_1} + a_2 e^{-i\phi_2} e^{i\delta_2}, \end{aligned}$$

where a_i are real numbers, ϕ_i and δ_i are the so-called weak and strong phases, respectively. A weak phase changes sign under CP conjugation, while a strong phase is invariant. The difference in rates follows as

$$|A|^2 - |\bar{A}|^2 = 2A_1 A_2 \sin(\phi_1 - \phi_2) \sin(\delta_1 - \delta_2). \quad (1.19)$$

It is important to note that both the weak and strong phases need to be different for the two terms in the amplitude, in order to generate CP violation.

1.3.2 CP violation in mixing

A second type of CP violation occurs in the mixing of neutral flavoured mesons, because the mass eigenstates are not CP eigenstates. The two mass eigenstates (heavy H and light L) can be written as

$$P_{H(L)} = pP_0 \pm q\bar{P}_0, \quad (1.20)$$

where P_0 and \bar{P}_0 are the flavour eigenstates and $|p|^2 + |q|^2 = 1$. If CP was an exact symmetry then the two CP eigenstates $(P_0 \pm \bar{P}_0)/\sqrt{2}$ would have to be the mass eigenstates, and thus $|q/p| = 1$. In the SM CP violation in mixing appears for the neutral B^0 (B_s^0) system only at the 10^{-3} (10^{-4}) level. CP violation in B^0 mixing, which has not been observed yet, can be assessed by comparing the $B^0 \rightarrow \bar{B}^0$ and $\bar{B}^0 \rightarrow B^0$ mixing rates.

1.3.3 CP violation in interference

A third type of CP violation occurs in the interference of the direct and mixed decay amplitudes. It is possible to observe this phenomenon when a neutral meson can decay to both a final state f or its CP conjugate \bar{f} (for example a CP eigenstate $f = \bar{f}$). In other words a generic meson P^0 at time $t = 0$ can reach the final state f at time $t > 0$ either with a direct decay ($P^0 \rightarrow f$) or after mixing ($P^0 \rightarrow \bar{P}^0 \rightarrow f$). The interference between two different paths results in a time-dependent asymmetry in the rates for the initial P^0 and \bar{P}^0 mesons to produce the state f .

1.4 Charmless B decays

Although CP violation in the B -meson sector was initially measured in a $\bar{b} \rightarrow c\bar{c}\bar{s}$ quark transition, the decays of B mesons to final states without a charm quark (charmless decays) are equally important for a complete understanding of the CP violation phenomenon. Studying both branching fractions and angular distributions of such decays probes the dynamics of weak and strong interactions. Moreover, the measurement of the weak phases in principle gives access to the CKM angles α , β and γ . However, studying the weak non-leptonic decays of heavy mesons from a theoretical approach is not trivial. One of the reasons is the necessity to account for the interplay of short-distance (SD) and long-distance (LD) QCD effects. For this purpose low-energy effective Hamiltonians (\mathcal{H}_{eff}) are used. They are calculated by making use of the operator product expansion, which allows the transition matrix elements from the initial state i to the final state f to be written as [24, 25]

$$\langle f | \mathcal{H}_{\text{eff}} | i \rangle = \frac{G_F}{\sqrt{2}} \lambda_{\text{CKM}} \sum_k C_k(\mu) \langle f | Q_k(\mu) | i \rangle. \quad (1.21)$$

In this way it is possible to factorize each contribution in a SD part, described by a perturbative Wilson coefficient function $C_k(\mu)$, and a LD part represented by the non-perturbative hadronic matrix elements $\langle f | Q_k(\mu) | i \rangle$, respectively. As usual, G_F is the Fermi constant, λ_{CKM} is a combination of relevant CKM elements, and μ is a renormalisation scale separating the two regimes. The renormalisation scale is typically chosen to be of the order of the mass of the decaying heavy quarks, a few GeV in case of B (or D) meson decays [25]. Considering a B meson decaying through a $\bar{b} \rightarrow \bar{s}$ transition the effective Hamiltonian can be written as [24, 25]

$$\mathcal{H}_{\text{eff}} = \frac{G_F}{\sqrt{2}} \left[\lambda_u^{(s)} (C_1(\mu) Q_1^{us} + C_2(\mu) Q_2^{us}) + \lambda_c^{(s)} (C_1(\mu) Q_1^{cs} + C_2(\mu) Q_2^{cs}) - \lambda_t^{(s)} \sum_{i=3}^{10} C_i(\mu) Q_i^s \right], \quad (1.22)$$

where $\lambda_i^{(s)} = V_{is} V_{ib}^*$, and Q_i are the different operators. The $\bar{b} \rightarrow \bar{d}$ transition can be represented in the same way, taking care of replacing s with d in the above formula. The current-current operators $Q_{u,s}^{1,2}$ and $Q_{c,s}^{1,2}$ have the form

$$Q_1^{cs} = (\bar{s}_\alpha c_\alpha)_{V-A} (\bar{c}_\beta b_\beta)_{V-A}, \quad Q_2^{cs} = (\bar{s}_\alpha c_\alpha)_{V-A} (\bar{c}_\beta b_\beta)_{V-A}, \quad (1.23)$$

$$Q_1^{us} = (\bar{s}_\alpha u_\alpha)_{V-A} (\bar{u}_\beta b_\beta)_{V-A}, \quad Q_2^{us} = (\bar{s}_\alpha u_\alpha)_{V-A} (\bar{u}_\beta b_\beta)_{V-A}, \quad (1.24)$$

while Q_i (with $i = 3, \dots, 6$) represent the QCD-penguin operators

$$Q_3^s = (\bar{s}_\alpha b_\alpha)_{V-A} \sum_q (\bar{q}_\beta q_\beta)_{V-A}, \quad Q_4^s = (\bar{b}_\alpha s_\beta)_{V-A} \sum_q (\bar{q}_\beta q_\alpha)_{V-A}, \quad (1.25)$$

$$Q_5^s = (\bar{s}_\alpha b_\alpha)_{V-A} \sum_q (\bar{q} q)_{V+A}, \quad Q_6^s = (\bar{s}_\alpha b_\beta)_{V-A} \sum_q (\bar{q}_\beta q_\alpha)_{V+A}, \quad (1.26)$$

and Q_i^s (with $i = 7, \dots, 10$) the EW-penguin operators

$$Q_7^s = \frac{3}{2} (\bar{s}_\alpha b_\alpha)_{V-A} \sum_q e_q (\bar{q}_\beta q_\beta)_{V+A}, \quad Q_8^s = \frac{3}{2} (\bar{s}_\alpha b_\beta)_{V-A} \sum_q e_q (\bar{q}_\beta q_\alpha)_{V+A}, \quad (1.27)$$

$$Q_9^s = \frac{3}{2} (\bar{s}_\alpha b_\alpha)_{V-A} \sum_q e_q (\bar{q}_\beta q_\beta)_{V-A}, \quad Q_{10}^s = \frac{3}{2} (\bar{s}_\alpha b_\beta)_{V-A} \sum_q e_q (\bar{q}_\beta q_\alpha)_{V-A}. \quad (1.28)$$

In these expressions $q = u, d, s, c, b$, $V \pm A$ indicates the vector-axial Lorentz current $\gamma^\mu = (1 \pm \gamma^5)$, α and β identify the $SU(3)_C$ colour of quarks and e_q is the electrical charge of quark q . Although one would expect a very minor contribution of EW penguins with respect to QCD penguins (the ratio of QED and QCD couplings being $\mathcal{O}(10^{-2})$), there are several decays where the effects of the EW penguin contributions are not negligible. This is due to the fact that the Wilson coefficient C_9 increases significantly with the mass of the top quark. This method allows the description of various B decays governed by these transitions, and the only differences between modes are due to the hadronic matrix elements related to the four-quark operators. The computation of the hadronic matrix elements represents the most challenging task and the principal source of theoretical uncertainties. Many models have been developed to address this problem, following various approaches: perturbative QCD (pQCD) [26], QCD factorisation (QCDF) [27], soft-collinear effective theory (SCET) [28], QCD light-cone sum-rule [29] and the factorisation-assisted topological approach (FAT) [30].

Table 1.3 – Averages of measurements performed at the B factories for some $B \rightarrow \eta^{(\prime)} X$ modes [13]: \mathcal{B} is the branching fraction, A_{CP} is the CP asymmetry between the \bar{B} and B decay rates, and S and C are the time-dependent CP-violation parameters in the SM.

Decay mode	\mathcal{B} (10^{-6})	A_{CP}	S	C
$B^+ \rightarrow \eta' K^+$	70.6 ± 2.5	$+0.013 \pm 0.017$		
$B^+ \rightarrow \eta K^+$	2.4 ± 0.4	-0.37 ± 0.08		
$B^+ \rightarrow \eta' K^*(892)^+$	4.8 ± 1.7	-0.26 ± 0.27		
$B^+ \rightarrow \eta K^*(892)^+$	19.3 ± 1.6	$+0.02 \pm 0.06$		
$B^+ \rightarrow \eta' \pi^+$	2.7 ± 0.9	$+0.06 \pm 0.16$		
$B^+ \rightarrow \eta \pi^+$	4.02 ± 0.27	-0.14 ± 0.07		
$B^+ \rightarrow \eta' \rho^+$	9.7 ± 2.2	$+0.26 \pm 0.17$		
$B^+ \rightarrow \eta \rho^+$	7.0 ± 2.9	$+0.11 \pm 0.11$		
$B^0 \rightarrow \eta' K^0$	66 ± 4		$+0.63 \pm 0.06$	-0.06 ± 0.04
$B^0 \rightarrow \eta K^0$	1.23 ± 0.26			
$B^0 \rightarrow \eta' K^*(892)^0$	2.8 ± 0.6	-0.07 ± 0.18		
$B^0 \rightarrow \eta K^*(892)^0$	15.9 ± 1.0	$+0.19 \pm 0.05$		
$B^0 \rightarrow \eta' \pi^0$	1.2 ± 0.6			
$B^0 \rightarrow \eta \pi^0$	$< 1.5(90\%CL)$			
$B^0 \rightarrow \eta' \rho^0$	$< 1.3(90\%CL)$			
$B^0 \rightarrow \eta \rho^0$	$< 1.5(90\%CL)$			

1.4.1 $B_{(s)} \rightarrow (\phi, \eta', \eta) X$ decays

Charmless B -meson decays are useful to test the SM (study CP violation and look for signal of possible new physics beyond the SM). Of particular interest are the charmless quasi-two body modes in which the B meson decays to Pseudoscalar-Pseudoscalar (PP), Pseudoscalar-Vector (PV) or Vector-Vector (VV) final states involving light resonances. The Belle and BaBar collaborations have largely studied PP and PV modes where one of these light resonances is an¹ $\eta^{(\prime)}$. Theory predictions for PP and PV branching fractions are typically a few per million and up to $\sim 70 \times 10^{-6}$ for the decay² $B^+ \rightarrow \eta' K^+$. Decays such as $B^0 \rightarrow \eta' K_S^0$, $B^0 \rightarrow K^+ K^- K_S^0$ and³ $B^0 \rightarrow \phi K_S^0$ are interesting because they are expected to have the same time-dependent CP-violation parameter $S = \sin 2\beta$ in the SM as the $B^0 \rightarrow J/\psi K_S^0$ decay. It is indeed useful to compare this parameter in the case of $b \rightarrow s\bar{s}s$, $b \rightarrow s\bar{u}u$ and $b \rightarrow s\bar{d}d$ transitions with respect to $b \rightarrow c\bar{c}s$.

The study of these decays together with several others of the family $B \rightarrow \eta^{(\prime)} X$ provides some of the most precise time-integrated and time-dependent CP-violation measurements, as shown in Table 1.3. For example, the time-dependent asymmetry in $B^0 \rightarrow \eta' K_{S,L}^0$ is found to be large (see quantity S of Table 1.3), and is consistent with that obtained in $B^0 \rightarrow J/\psi K_{S,L}^0$ [31].

Other interesting neutral decays are modes with final states $\eta' K^*$ and ηK , for which the

¹The notation η' refers to the $\eta'(958)$ meson.

²For all the decays charge conjugation is implied throughout this document.

³The notation ϕ refers to the $\phi(1020)$ meson.

branching fractions are suppressed with respect to $\eta'K$ and ηK^* . In the latter cases, the penguin $b \rightarrow s$ contributions interfere constructively, while the interference is destructive for $B \rightarrow \eta'K^+$ and $B \rightarrow \eta K$ [32]. In the SM the CP charge asymmetry in charged decays, such as $B^+ \rightarrow \eta'K^+$, is expected to be small. Recently, the CP-violating charge asymmetry for the $B^+ \rightarrow \eta'K^+$ decay mode has been measured precisely at LHCb, $A_{CP} = -0.002 \pm 0.013$ [33]. On the other hand, much larger asymmetries have been measured for $B^+ \rightarrow \eta K^+$, $B^+ \rightarrow \eta\pi^+$, $B^+ \rightarrow \eta'K^*(892)^+$ and $B^+ \rightarrow \eta'\rho^+$ decays. Indeed, for those decay modes, the $b \rightarrow s$ penguin amplitudes are of the same size as the $b \rightarrow u$ tree amplitude, leading to the possibility of large CP-violating asymmetries.

1.4.2 $B_s^0 \rightarrow \eta'\phi$ decays in the family $B_s^0 \rightarrow hh$ ($h = \eta', \phi$)

With respect to the B^0 and B^+ decays, much less is known about the $B_s^0 \rightarrow \eta^{(\prime)}X$ decays. Of particular interest is the family $B_s^0 \rightarrow XY$, where X and Y are each either a η , η' or ϕ meson. These modes can all be used for time-dependent CP violation studies. Most of them are dominated by the $b \rightarrow s\bar{s}s$ gluonic penguin diagram. The “golden mode” of this family is $B_s^0 \rightarrow \phi\phi$, which has a branching fraction of $(1.84 \pm 0.05$ (stat) ± 0.07 (syst) ± 0.11 (f_s/f_d) ± 0.12 (norm)) $\times 10^{-5}$, where f_s/f_d represents the ratio of the B_s^0 and B^0 production cross-sections, and the $B^0 \rightarrow \phi K^*(892)^0$ mode is used for normalisation [34]. The CP-violating phase in $B_s \rightarrow \phi\phi$, measured using data collected in 2011 and 2012 by the LHCb detector, is found to be $\phi_s^{s\bar{s}s} = -0.17 \pm 0.15$ (stat) ± 0.03 (syst) [35]. The experimental result, which still has an uncertainty significantly larger than that of the CP-violating phase $\phi_s^{c\bar{c}s}$ measured in $B_s^0 \rightarrow J\psi K^+ K^-$ or $B_s^0 \rightarrow J\psi\pi^+\pi^-$ [36], shows that no large CP violation is present neither in $B_s^0 - \bar{B}_s^0$ mixing nor in the $b \rightarrow s\bar{s}s$ decay amplitude, as expected in the Standard Model. This measurement required an angular analysis to extract the CP content of the vector-vector final state.

In 2015, LHCb made the first observation of the $B_s^0 \rightarrow \eta'\eta'$ decay mode, with a branching fraction of $(33.1 \pm 6.4$ (stat) ± 2.8 (syst) ± 1.2 (norm)) $\times 10^{-6}$ [33], where the third uncertainty comes from the $B^+ \rightarrow \eta'K^+$ branching fraction used as normalisation. The CP-violating phase $\phi_s^{s\bar{s}s}$ can also be measured using the $B_s^0 \rightarrow \eta'\eta'$ decay. This mode being a pure CP eigenstate, there is no need for an angular analysis as in $B_s^0 \rightarrow \phi\phi$. Unfortunately, at present the signal yield is still too small for CP measurements.

All the other modes of the family (except $B_s^0 \rightarrow \phi\phi$) are also pure CP-even final states and therefore do not require an angular analysis. However, this advantage is diluted by a low reconstruction efficiency, due to the presence of neutrals in the final state of the experimentally relevant η or η' decays. Despite that CP measurements are not possible at the moment with these modes, it is already important to measure their branching fraction in view of future studies. Among these modes the $B_s^0 \rightarrow \eta'\phi$ is of particular interest. Figure 1.3 shows the dominant Feynman diagrams of the decay. The experimental inefficiency introduced by the presence of the neutral particle in the η' resonance decay is compensated by the high reconstruction efficiency for the ϕ meson. Theoretical predictions for this mode span a wide range (see Table 1.4) due to the poor knowledge of several parameters used as inputs to the

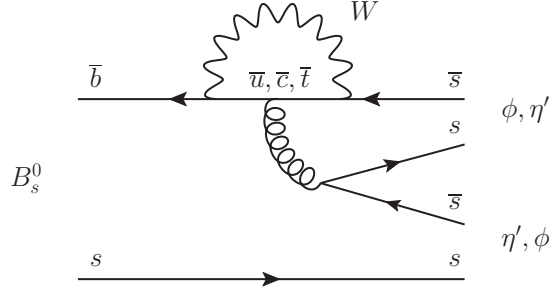


Figure 1.3 – Lowest-order diagrams for the $B_s^0 \rightarrow \eta' \phi$ decay. The spectator quark can become part of either the η' or the ϕ meson, forming two different amplitudes (called PV and VP in the text).

Table 1.4 – Theoretical predictions for the $B_s^0 \rightarrow \eta' \phi$ branching fraction.

Theory approach	\mathcal{B} (10^{-6})	Reference
QCD factorisation	$0.05^{+1.18}_{-0.19}$	[27]
QCD factorisation	$2.2^{+9.4}_{-3.1}$	[37]
Perturbative QCD	$0.19^{+0.20}_{-0.13}$	[38]
Perturbative QCD	$20.0^{+16.3}_{-9.1}$	[39]
SCET	$4.3^{+5.2}_{-3.6}$	[40]
SU(3) flavour symmetry	5.5 ± 1.8	[41]
FAT	13.0 ± 1.6	[30]

model, such as form factors, the charm penguin contributions, gluonic penguins and the $\omega - \phi$ mixing [27, 37, 38, 39, 40, 41, 30].

In these predictions the branching fraction for this decay is related to the one of $B_s^0 \rightarrow \eta \phi$. The η' and the η physical particles result from a mixture of the $\eta_q = (u\bar{u} + d\bar{d})/\sqrt{2}$ and $\eta_s = s\bar{s}$ states and, in the quark-flavour basis mixing scheme, can be represented as

$$\begin{pmatrix} \eta \\ \eta' \end{pmatrix} = \begin{pmatrix} \cos\theta & -\sin\theta \\ \sin\theta & \cos\theta \end{pmatrix} \begin{pmatrix} \eta_q \\ \eta_s \end{pmatrix}, \quad (1.29)$$

where θ is the $\eta - \eta'$ mixing angle [42]. The decay amplitudes of $B_s^0 \rightarrow \eta^{(\prime)} \phi$ are given by the following expressions,

$$A(B_s^0 \rightarrow \eta \phi) = \cos\theta A(B_s^0 \rightarrow \eta_q \phi) - \sin\theta A(B_s^0 \rightarrow \eta_s \phi), \quad (1.30)$$

$$A(B_s^0 \rightarrow \eta' \phi) = \sin\theta A(B_s^0 \rightarrow \eta_q \phi) + \cos\theta A(B_s^0 \rightarrow \eta_s \phi), \quad (1.31)$$

where

$$A(B_s^0 \rightarrow \phi\eta_s) = A_{\phi\eta_s}(\alpha_3^p + \alpha_4^p) + A_{\eta_s\phi}(\alpha_3^p + \alpha_4^p), \quad \sqrt{2}A(B_s^0 \rightarrow \eta_q\phi) = A_{\phi\eta_q}(\delta_{pu}\alpha_2 + 2\alpha_3^p). \quad (1.32)$$

In the latter formulas, α_i^p ($p = u, c$ and $i = 2, 3, 4$), represent the flavour operators giving contributions and the factors $A_{\phi\eta_{s(q)}}$ and $A_{\eta_s\phi}$ include the factorisable matrix elements depending on the form factors. There is a strong cancellation between the PV and VP penguin amplitudes $\alpha_4^c(\phi\eta_s)$ and $\alpha_4^c(\eta_s\phi)$. It is useful to note that $\alpha_3^c(\phi\eta_s)$ and $\alpha_3^c(\eta_s\phi)$ are of opposite sign. This implies that the sign of $A(B_s^0 \rightarrow \phi\eta_s)$ depends on the $B \rightarrow \phi$ form factor $A_{B_s\phi}^0$. Depending on the values obtained from the many theoretical approaches, one can either have a constructive contribution of $A(B_s^0 \rightarrow \phi\eta_s)$ and $A(B_s^0 \rightarrow \phi\eta_q)$, leading to a branching fractions of few 10^{-6} , or a near cancellation, so that the expected branching fraction, of order 10^{-7} , becomes very small. While the QCDF approach leads to $\mathcal{B}(B_s^0 \rightarrow \eta'\phi) > \mathcal{B}(B_s^0 \rightarrow \eta\phi)$, the pQCD theory predicts a significantly larger value for $\mathcal{B}(B_s^0 \rightarrow \eta\phi)$ and the pattern is opposite for SCET [38, 37, 40]. This is why the study of this decay is very important. Even if the expected yield is too small for any CP measurement, the measurement of its branching fraction is useful to gain information on the form factor $A_{B_s\phi}^0$ and constrain theoretical models.

2 LHCb detector

2.1 The Large Hadron Collider project

The Large Hadron Collider (LHC) is a 27 km ring of superconducting magnets placed in the tunnel that was previously used from the Large Electron-Positron (LEP) accelerator (see Fig. 2.1). The LHC delivers mainly proton-proton (pp) collisions, but is also used to produce proton-heavy ion and heavy ion-heavy ion collisions.

The accelerator facility consists of 1232 superconducting dipole magnets, one array of accelerating radio-frequency (RF) cavities and a variety of higher-order magnets used for beam focusing and corrections. The beams collide at four interaction points which house the four large LHC experiments: ALICE, ATLAS, CMS and LHCb.

Proton-proton collisions with a centre-of-mass energy $\sqrt{s} = 7$ TeV were provided in 2010 and 2011, and $\sqrt{s} = 8$ TeV collisions were achieved in 2012 (Run 1). After the first long shutdown in 2013 and 2014 (LS1), new operations at $\sqrt{s} = 13$ TeV began in 2015, close to the design energy of 14 TeV. It was decided to stay at $\sqrt{s} = 13$ TeV throughout Run 2 until the end of 2018. The nominal energy of 14 TeV is expected to be reached at the beginning of Run 3 in 2021.

The CMS and ATLAS experiments are designed for the direct search of BSM phenomena. On the other hand, the main goal of the LHCb experiment is the indirect search of NP in the decays of hadrons containing a heavy b or c quark. The effect of new particles or physics processes might be observed in heavy flavour physics, where many models of new physics predict contributions that modify the expectation values of CP-violating phases or branching fractions of rare decay modes. Some decays that are highly suppressed in the SM, might be observable if NP phenomena enter in the game. In order to study all these possibilities, it is important to collect high statistics samples of heavy flavour hadrons.

The increase in centre-of-mass energy and the reduced proton bunch spacing, from 50 ns in Run 1 to the design value 25 ns in Run 2, contribute significantly to improve the amount of available data needed for these studies. Moreover, the integrated luminosity collected so far in Run 2 is larger than expected due to the remarkable high efficiency of the LHC machine in 2016. After Run 3, during a long shutdown from 2024 to 2026, the machine will be upgraded for a second phase of high-luminosity operation.

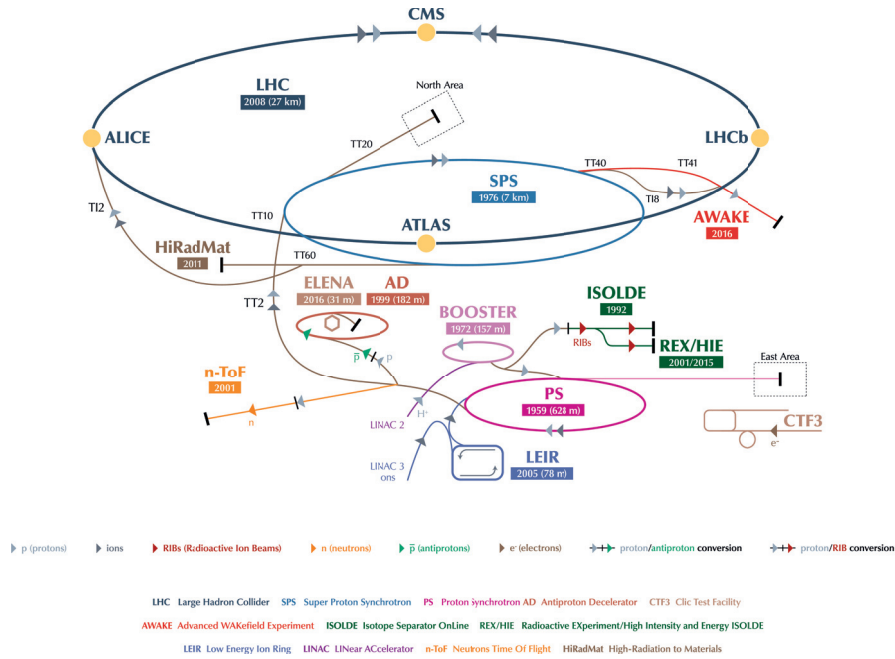


Figure 2.1 – Schematic layout of the CERN accelerator complex and its experimental facilities, in particular the LHC collider, its injectors and its main experiments [43].

2.2 The LHCb experiment

LHCb is a single-arm spectrometer with a forward angular coverage from approximately 15 to 300 (250) mrad in the bending (non-bending) plane [44]. This corresponds to a range in pseudo-rapidity η between 1.8 and 4.9, where η is defined as $\eta = -\ln(\tan(\theta/2))$, and θ is the angle between the momentum \vec{p} of a particle and the direction of the clockwise-rotating beam.

The detector geometry is optimized for the detection of hadrons containing b quarks. Indeed, the production of $b\bar{b}$ pairs occurs mostly through gluon fusion in which the momenta of the incoming partons are strongly asymmetric in the laboratory frame. The centre of mass of the produced $b\bar{b}$ pair is boosted along the direction of the gluon with higher momentum, and this results in both b hadrons being produced in the same forward (or backward) cone, as illustrated in Fig. 2.2. For each collision of the proton beams at the interaction point, a large number of particles coming from multiple primary pp interactions (pile-up) fly in the detector acceptance, resulting not only in events that are very complicated to process in real time, but also in a significant radiation damage to the detector. In order to reduce the probability of having many interactions in a single proton-bunch collision, a beam-focussing method has been implemented to reduce the nominal luminosity at the LHCb interaction point to $L = 4 \times 10^{32} \text{cm}^2 \text{s}^{-1}$. In these conditions the most probable number of pp interactions is one per bunch-crossing [46] (see Fig. 2.3). The LHC is the most intense source of b hadrons. In proton-proton collisions at $\sqrt{s} = 13 \text{ TeV}$, the $b\bar{b}$ cross section is $\sim 600 \mu\text{b}$, value in the full η

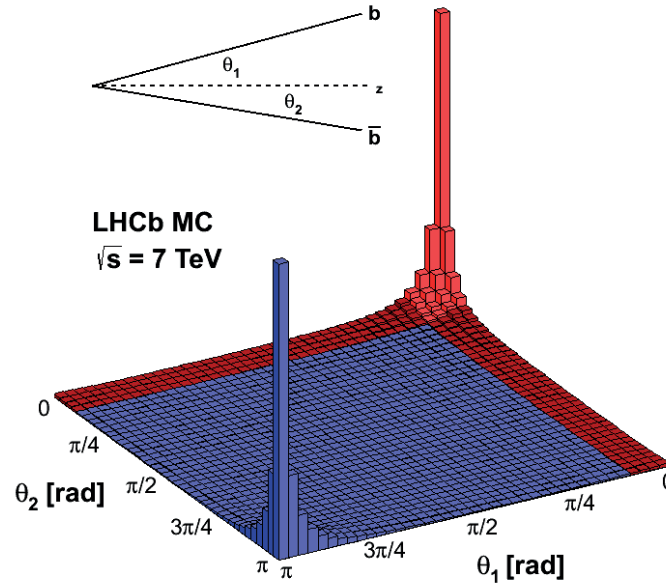


Figure 2.2 – Two-dimensional distribution of the polar angles θ_1 and θ_2 of the produced b and \bar{b} quarks in pp collisions at $\sqrt{s} = 8 \text{ TeV}$, as simulated with the event generator PHYTIA 8 [45]. The red colour indicates the angular acceptance of the LHCb detector.

range [47]. This corresponds to 10^{12} produced $b\bar{b}$ pairs per year. The large centre-of-mass energy implies that the complete spectrum of b hadrons can be studied, including the B_c^+ meson and the b baryons that are inaccessible at the B factories.

As shown in Fig. 2.4 the integrated luminosity collected by LHCb is 1.1 fb^{-1} in 2011 at $\sqrt{s} = 7 \text{ TeV}$, 2.1 fb^{-1} in 2012 at $\sqrt{s} = 8 \text{ TeV}$, and 0.3 fb^{-1} and 1.7 fb^{-1} at $\sqrt{s} = 13 \text{ TeV}$ in 2015 and 2016, respectively.

However in this hadronic environment the amount of background is very large because only 1% of the inelastic events contain b quarks. To fulfill the requirements of the physics programme and to cope with the large background, the performance of the LHCb detector is based on a few but key features:

- Excellent vertex capability, essential to distinguish the decay vertex of a b hadrons (secondary vertex, SV) from the pp collision “primary vertex” (PV), where that hadron was produced. This implies also an excellent proper time resolution, which is a key ingredient for time-dependent analyses.
- Good particle identification (PID), for proton/kaon/pion/muon/electron separation.
- A very efficient trigger scheme, able to reject a large fraction of the background and

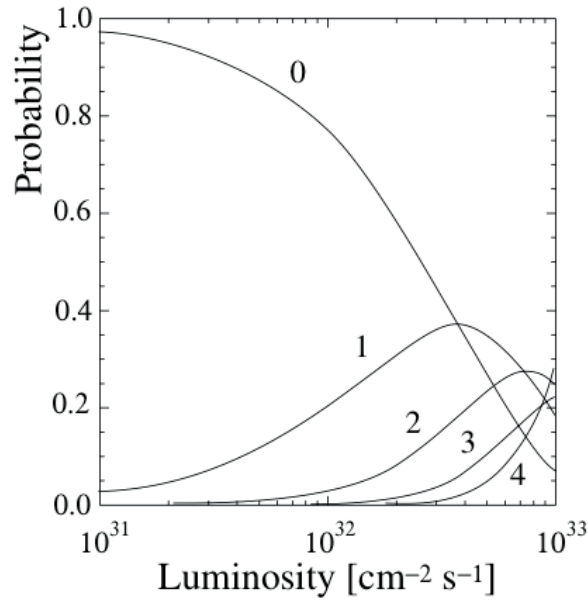


Figure 2.3 – Probability of 0, 1, 2, 3 or 4 pp collisions per bunch-crossing as a function of the instantaneous luminosity. The value of instantaneous luminosity that maximises the probability of a single primary collision is $4 \times 10^{32} \text{ cm}^2 \text{ s}^{-1}$ [46].

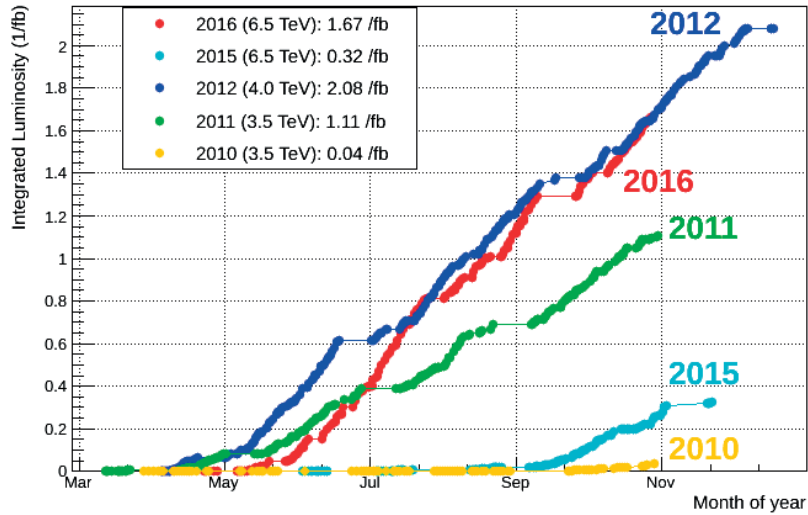


Figure 2.4 – Integrated luminosity collected by the LHCb experiment in Run 1 (2011, 2012) and Run 2 (2015, 2016) [48].

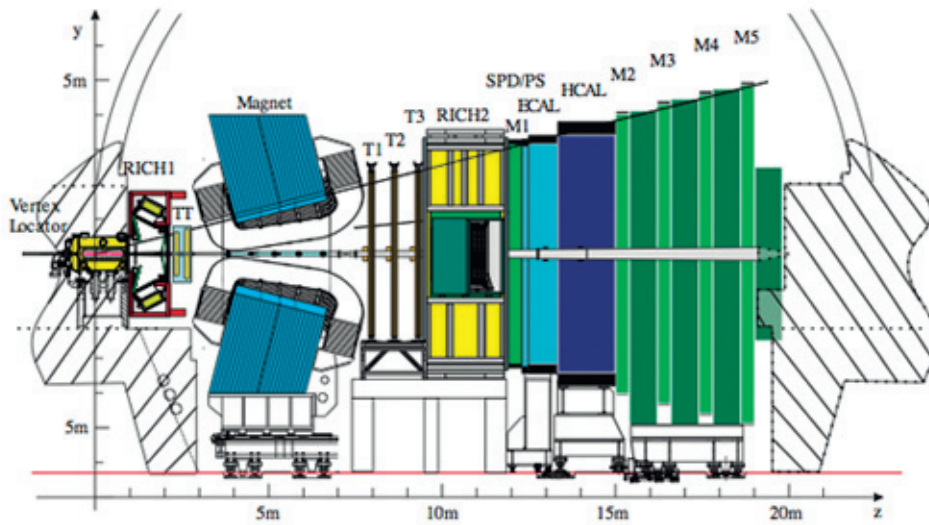


Figure 2.5 – Schematic layout of the LHCb detector and its coordinate system [49].

select the final leptonic, semileptonic and hadronic states of interest.

- An excellent momentum resolution, in order to measure accurately the invariant masses and reject combinatorial background.

Figure 2.5 shows a schematic layout of the LHCb detector. It consists of a tracking system, which includes a vertex detector, a warm magnet dipole and two series of tracking detectors, and the particle identification system, which includes two Cherenkov detectors, electromagnetic and hadronic calorimeters and a muon detection system [44, 49]. The coordinate system has its origin at the nominal pp interaction point, the z axis coincides with the beam axis, pointing from the VELO to the muon stations, the x axis is perpendicular to the beam axis in the horizontal plane, pointing away from the centre of the collider ring, while the y axis is perpendicular to the xz plane, in the upward direction. In the following, the LHCb sub-detector systems are described in more detail.

2.3 Tracking system

The tracking system is designed to reconstruct with a high spatial resolution the trajectory of the charged particles traversing the detector and to give information on quantities such as the charge and the momentum of the particles, measured from the trajectory bending due to the magnetic field, and the position of the production and decay vertices.

2.3.1 The dipole magnet

The magnetic field in LHCb is generated by a non-superconducting dipole magnet. The main component of the magnetic field lies along the y axis, and its bending power is approximately 4Tm in the horizontal plane, in the region $0 < z < 10$ m, where the tracking detectors are located. The magnetic field allows the measurement of the particle momentum p with a relative resolution of $0.4 - 0.6\%$, for $5 < p < 100$ GeV/ c .

The magnet polarity is flipped at periodic intervals such that a variety of systematic uncertainties in charged particle tracking can be studied and accounted for. The magnet consists of two coils, of 27 ton each, mounted inside a 1500 ton steel frame. In order to achieve the desired momentum resolution, a precise knowledge of the magnetic field is needed. The magnetic field integral is measured with an array of Hall probes, and is parametrized in the full tracking volume.

2.3.2 Vertex Locator

The Vertex Locator (VELO) measures the trajectory of charged particles in the region closest to the interaction point, with the main goal to locate and separate the primary vertices and secondary vertices with a spatial resolution much higher than the decay length of b and c hadrons in LHCb ($ct \sim 0.01 - 1$ cm).

Since the beauty mesons produced in the LHCb acceptance mostly fly close to the beam axis, the VELO is designed to operate as close as possible to the beam. The detector consists of two sets of 21 semicircular silicon modules perpendicular to the beam axis and placed around the collision point, on both sides with respect to the z axis. In stable data-taking conditions the halves are close to the beam line (distance ~ 8 mm), while if the LHC beams are not stable, they are moved away to about 4 cm. This is illustrated in Fig. 2.6. The modules located in the region $z > 0$ measure the vertex positions with high precision, while the stations at $z < 0$ are used to identify the high-multiplicity events due to pile-up. Each module contains two silicon-strip sensors: an r -sensor and a ϕ -sensor, to measure the particle coordinates (radial distance and azimuthal angle in the xy plane). The excellent vertex reconstruction, impact parameter (IP) resolution and decay time resolution achieved by LHCb, are mostly due to the VELO performance.

2.3.3 Silicon Tracker

The Silicon Tracker (ST) consists of two sub-detectors: the Tracker Turicensis (TT) upstream of the dipole magnet and the Inner Tracker (IT), which is the inner part of the tracking stations downstream of the magnet (see Fig. 2.7). Both detectors use single-sided silicon micro-strip sensors. The TT is designed for the reconstruction of low-momentum tracks deflected by the magnetic field outside the acceptance of the detector, while the IT reconstructs those tracks that pass through the magnet and are close to the beam line.

The layout of the TT sub-detector is shown in Fig. 2.8; it consists of a single station and has four

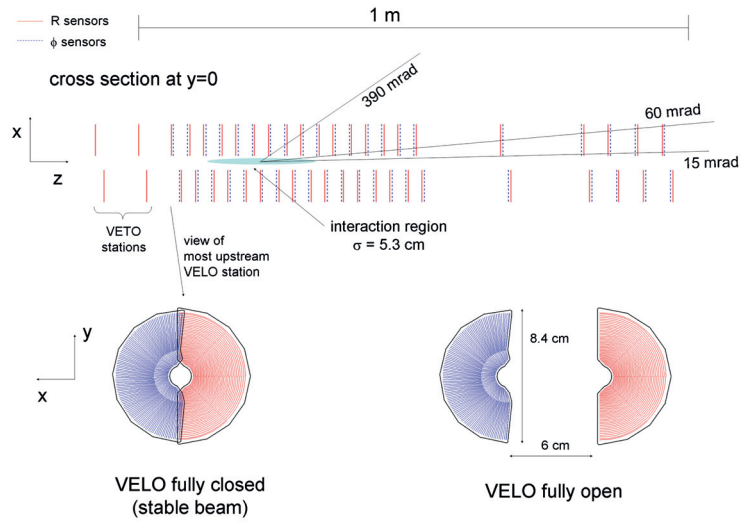


Figure 2.6 – Schematic view of the VELO detector (top) and of a single module in the closed and open configurations (bottom) [44].

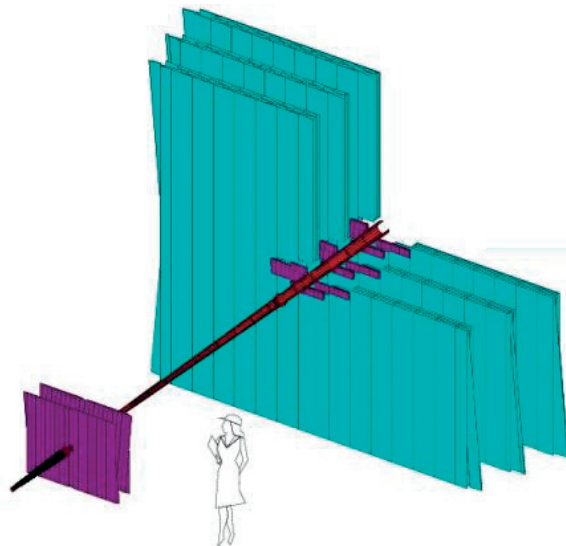


Figure 2.7 – LHCb tracking stations. The beam pipe is shown in red, the TT (front) and the IT (back) in purple, and the OT stations in blue [50].

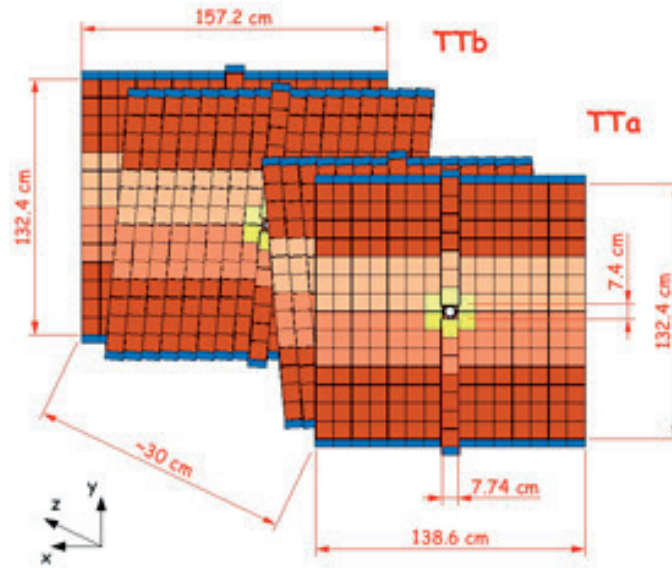


Figure 2.8 – Layout of the four layers of the TT detector [50].

planar detector layers; the first and the last layers have vertical strips, while the two middle layers have strips tilted by $+5^\circ$ and -5° with respect to the vertical. The layers are arranged in pairs, with the first two separated by around 27 cm from the second pair along the beam axis, with the goal to aid the tracking reconstruction algorithms. Each layer is composed of half-modules, upper and lower, with each half divided into rows of seven silicon sensors (or eight in the two downstream layers). The first two layers give the x and u coordinates while the second two measure the v and z coordinates. Depending on the proximity to the beam pipe the sensors are organised in two or three readout sectors. Each sensor is 9.64 cm wide, 9.44 cm long and $500 \mu\text{m}$ thick, and carries 512 readout strips.

The three IT stations have a four-layer design, similar to that of the TT (two $\pm 5^\circ$ stereo views in between two layers with vertical strips). The IT covers a cross-shaped area around the LHC beam pipe (see Fig. 2.9), where particle densities are too high for the drift tube technology used in the OT detector, discussed in the following. The sensitive surface of the three IT stations is approximately 4.2 m^2 . The sensors are 7.6 cm wide and 11 cm long with 384 readout strips. They have different thicknesses ($410 \mu\text{m}$ for those placed at the left and right sides of the beam pipe, $320 \mu\text{m}$ for sensors above and below) in order to ensure good signal-to-noise ratio in the entire detector, while keeping the material budget as low as possible.

2.3.4 Outer Tracker

The Outer Tracker (OT) is a drift-time detector, placed in the external part of the three stations (T stations) housing the IT (see Fig. 2.7). It is designed to provide high tracking performance for charged particles over the large area in the acceptance not covered by the Inner Tracker. It

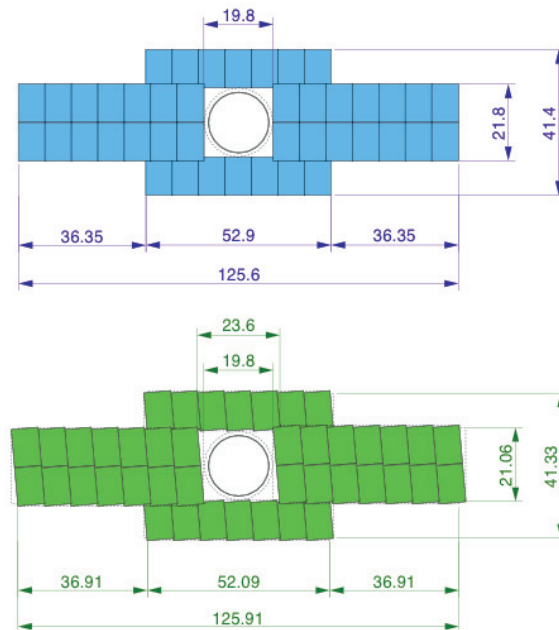


Figure 2.9 – Layout of an x -layer (top) and a stereo layer (bottom) in the T2 station of the Inner Tracker. [50].

therefore consists of three stations, each having four layers with the (x, u, v, x) orientations. The dimensions of the OT with respect to the IT have been chosen to fulfill the requirement that the OT occupancy should be less than 10% at the nominal instantaneous luminosity. Each layer consists of two staggered arrays of straw-tubes, which ensure a spatial resolution of $\sim 200 \mu\text{m}$ in a large momentum region. Each tube is filled with a mixture of Ar (70%) and CO_2 (30%) gases, and contains a gold-plated tungsten wire. The gas mixture was chosen to guarantee a drift time below 50 ns. Since the LHC bunch spacing was reduced from 50 ns in Run 1 to the design value of 25 ns (half of the drift time in the OT) in Run 2, spillover effects in the OT have become more important in Run 2 as compared to Run 1.

2.3.5 Track reconstruction

The VELO, the ST and the OT data are used in the reconstructions of the tracks crossing the LHCb detector. Different track types are defined, depending on the sub-detectors in which those are reconstructed. Depending on the track type, different algorithms are used [51]. A pictorial view of the different tracks type is given in Fig. 2.10. Five different categories of tracks are reconstructed:

- VELO tracks, detected only in the VELO, by both ϕ - and r -sensors. The VELO tracks can fly at large polar angles or backwards and are used for the reconstruction of PVs.
- T tracks, reconstructed only in the downstream T stations. They can come either from

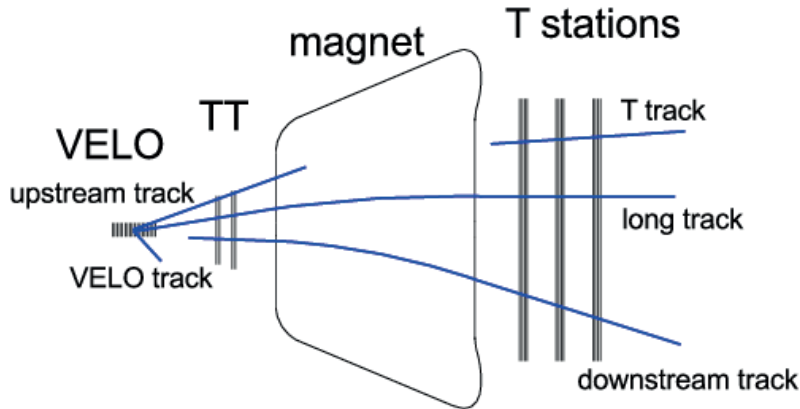


Figure 2.10 – Schematic diagram of the track types reconstructed by the different tracking algorithms [52].

very long-lived particles or be the result of an interaction with the detector material.

- Upstream tracks, which hit only the VELO and TT detectors. Due to their low momentum and the bending of the magnetic field, they fly out of the LHCb acceptance after the TT.
- Downstream tracks, reconstructed from hits in the TT and T stations, are used to identify charged daughters of long-lived particles, such as K_S or Λ , which may have a decay vertex outside of the VELO region.
- Long tracks, which leave hits in all the tracking sub-detectors, allowing a precise and accurate momentum determination. In order to ensure very high efficiency performance, two complementary algorithms are used to reconstruct long tracks, such that a loss of efficiency in one algorithm can be compensated by the other. The long tracks are the most useful ones in the physics analysis presented in this document.

2.4 Particle identification systems

The particle identification (PID) systems have a very important role in the study of heavy-flavour decays, in particular to disentangle the desired signal from background when they are topologically similar but differ by the final state particles (e.g. pions and kaons). Four different sub-detectors are used to distinguish the different particles.

2.4.1 RICH detectors

The discrimination between charged pions, kaons and protons is provided by two Ring Imaging Cherenkov detectors, RICH1 and RICH2. The two detectors are optimized to cover a large range of track momentum.

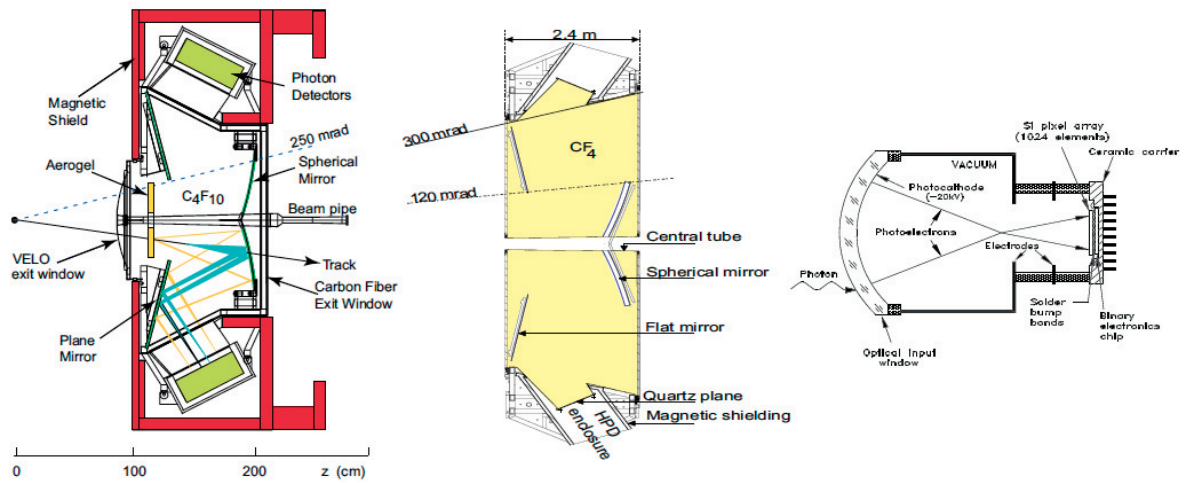


Figure 2.11 – Illustrations of the RICH1 (left) and RICH2 (middle) detectors, and of the Hybrid Photon Detectors (right) [50].

RICH1 provides high discrimination in the range $2 - 40 \text{ GeV}/c$ and covers the full LHCb angular acceptance, while RICH2, placed downstream of the tracking stations, is optimised for high momentum tracks ($15 - 100 \text{ GeV}/c$) and covers a limited angular acceptance ($15 - 120 \text{ mrad}$ near the beam pipe). Despite the limited acceptance, RICH2 captures a large fraction of the tracks in the momentum range in which it has discriminating power. The two detectors are shown in Fig. 2.11. The different momentum acceptances are achieved by the use of different radiators: C_4F_{10} and aerogel for RICH1, and CF_4 for RICH2. Before the start of Run 2 data taking, the aerogel has been removed from RICH1. Indeed, its contribution to the PID performance is worse than expected and it is difficult to integrate it in the new Run 2 trigger scheme due to the large rings produced and to the many photon candidates being very CPU consuming. Its removal provides improved π/K separation and it allows to use the offline PID algorithms in the online reconstruction [53]. Both RICH detectors have spherical primary focusing mirrors and secondary flat mirrors that allow the photon to be guided outside the spectrometer acceptance to the Hybrid Photon Detectors (HPD), which detect photons with a wavelength in the range $200 - 600 \text{ nm}$. Iron screens are used as shielding material against the residual magnetic field around the HPD.

The information given by the RICH detectors is then used in the reconstruction algorithms [54]. In order to identify the species of the charged particle corresponding to a certain track, the information on the Cherenkov angle is combined with the track momentum measured by the tracking system. The reconstruction algorithm is based on a global likelihood fit. At the first steps all the tracks are assumed to be pions and then for each track in turn, the likelihood is recomputed leaving all the parameters identical and changing only the mass hypothesis (electron, muon, pion, kaon or proton). The preferred value of the mass hypothesis corresponds to the one for which the largest increase in the event likelihood is obtained. The procedure is repeated until the optimal value is set for all the tracks.

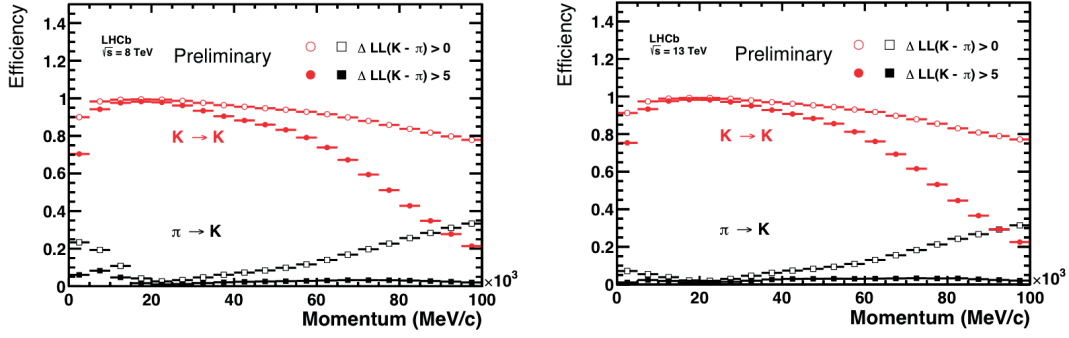


Figure 2.12 – Kaon identification efficiency (red) and pion misidentification efficiency (black) measured in $\sqrt{s} = 8$ TeV (left) and $\sqrt{s} = 13$ TeV (right) data as a function of track momentum. Two different particle identification requirements have been imposed on the samples (open and filled marker) [53].

The PID of the RICH detectors has an efficiency of around 95% for the identification of kaons in the momentum region 5 – 100 GeV/c, while the pion misidentification remains below 5%. Figure 2.12 shows the performance in Run 1 and Run 2.

2.4.2 Calorimeters

The LHCb calorimeter system (CALO), located downstream of RICH2 and the first muon station, is designed to identify and reconstruct electrons, photons and π^0 mesons. It also provides transverse energy (E_T) information used at the first trigger level described further in Sec. 2.5.

The CALO consists of four sub-detectors: the scintillating pad detector (SPD), followed by a preshower (PS) detector, an electromagnetic calorimeter (ECAL) and, finally, a hadronic calorimeter (HCAL). The four calorimeters share the same structure: the interaction of the particles with the detector material produces scintillating light that is collected and guided by Wave-Length Shifting fibres (WLS) and is read by PhotoMultipliers (PMTs). The threshold set for the SPD detector allows only the charged particles to deposit energy, while the PS, being located after a 1.5 cm lead converter corresponding to around 2.5 radiation lengths, measures only significant deposit of energy from photons and electrons. The passage of electrons and photons through the lead layer allows the start of an electromagnetic shower. These particle species are then stopped inside the ECAL, while the hadrons are stopped in the HCAL. The information collected by the SPD and the PS, combined with the cluster information in the ECAL, helps to distinguish the electromagnetic nature of the particle. The SPD/PS detector has an active area about 6.2 m wide and 7.6 m high, divided in cells of different sizes, designed for a projective correspondence between SPD, PS and ECAL.

The ECAL is designed to reach an energy resolution ($\sigma_E/E = 10/\sqrt{(E/\text{GeV})} \oplus 1\%$) sufficient to achieve a good resolution in the mass reconstruction of radiative decays with a high p_T photon, such as $B \rightarrow K^* \gamma$, or of decays with a π^0 in the final state, such as $B \rightarrow \rho \pi^0$, where the

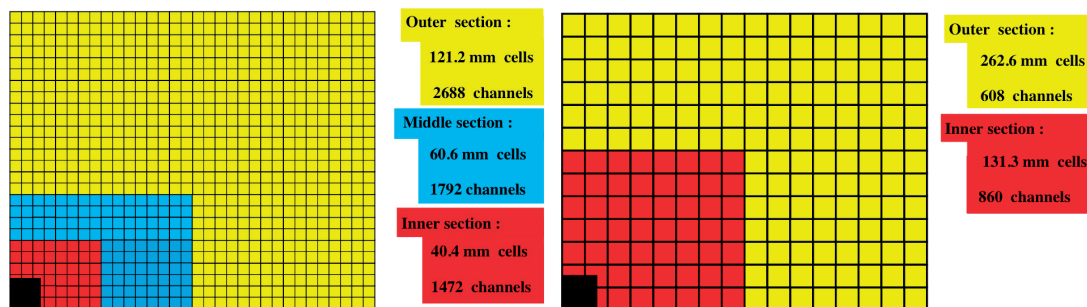


Figure 2.13 – Schematic view of the segmentation of the SPD, PS and ECAL (left), and HCAL (right). Only one quarter of the detector front face is shown. In the left figure the cell dimensions are given for the ECAL [55].

π^0 mass resolution is around $8 \text{ MeV}/c^2$. The ECAL consists of 66 layers, which alternate 2 mm thick lead tiles and 4 mm thick scintillator tiles, separated by $120 \mu\text{m}$ thick white, reflecting paper. The active volume of the ECAL is 42 cm deep, corresponding to 25 radiation lengths sufficient to capture the energy of the electromagnetic shower and ensure a good resolution. As for the SPD/PS calorimeters, the size of the ECAL cells varies with the distance from the beam pipe.

In contrast with the ECAL, the hadronic showers are not fully contained in the HCAL. This is because the E_T resolution requirement of the trigger is not very stringent. For this reason the thickness of the HCAL active area corresponds only to 5.6 hadronic interaction lengths. The detector consists of 6 mm-thick iron plates alternated with 4 mm-thick scintillating layers. Its lateral segmentation is coarser than the rest of the calorimeter system, as illustrated in Fig. 2.13. The HCAL resolution is around $\sigma_E/E = (69 \pm 5)/\sqrt{(E/\text{GeV})} \oplus (9 \pm 2)\%$.

The particles identified through the calorimeter system are the following:

- The electron identification is based on the information obtained from the ECAL, the PS and the HCAL sub-detectors. To improve the identification the output of the RICH system is also used, resulting in an efficiency of $\sim 97\%$ with a misidentification rate below 2 %.
- The photons are identified thanks to their energy deposits in the ECAL. The detector cells are clustered applying a 3×3 cell pattern around local maxima of energy deposition. The tracks reconstructed in the event are matched to the ECAL clusters and an estimator, χ_γ^2 , is defined. If a cluster does not have any matching track ($\chi_\gamma^2 > 4$), it is identified as a photon candidate. Almost half of the photons originating at the interaction point are “converted” photons, which materialise as electron and positron pairs. A fraction of these photons are converted before the magnet and are seen as two separate charged clusters in the calorimeters. The tracking system may reconstruct the corresponding electron tracks. The photons converted after the magnet usually produce a single cluster in the ECAL without reconstructed track. Low momentum neutral pions are reconstructed as

pairs of well separated photons (resolved π^0) and have a mass resolution of $8 \text{ MeV}/c^2$. On the other hand, if a neutral pion has a sufficiently large momentum, the two photons coming from its decay are emitted with a very small separation angle and, because of the finite granularity of the ECAL, the individual clusters cannot be resolved. In this case the π^0 is classified as “merged” and a specific algorithm is run in order to identify the two highest energy deposits inside the original cluster and distinguish the high momentum pions from high momentum photons.

2.4.3 Muon system

The muon system (Fig. 2.14), located in the most downstream part of the detector, has an important role for several key analyses of the LHCb physics programme, such as $B_s^0 \rightarrow \mu^+ \mu^-$, which involves high p_T muons.

The detector is composed of five muon stations. The first one (M1) is placed upstream of the calorimeter system, with the goal to improve the transverse momentum resolution in the trigger, and the other four downstream of the HCAL (M2–5). Each station consists of four regions, having on average the same flux of particles and occupancy. The four downstream stations are interleaved with three 80 cm thick iron absorber plates in order to select only penetrating muons and reduce backgrounds. The first three stations, M1–M3, are finely segmented and used to define the track momentum, reaching a p_T resolution of 20%. The stations M4 and M5 present a spatial resolution limited with respect to the first three. For this reason, they are mostly used in the identification of the penetrating particles. The detection technology consists of three gas electron multiplier foil (triple-GEM) detectors used in the inner region of M1, due to the high particle flux expected, and multi-wire proportional chambers (MWPC) in the rest of the muon system. The muon identification is based on three techniques [57]:

- A first level of identification (called isMuon) is a loose binary selection defined according to the hits found in the muon stations within a field of interest (FOI) around the track extrapolation. The number of stations for which a hit is required and the FOI size depend on the track momentum.
- The second technique consists in the computation of a likelihood for the muon and non-muon hypotheses, which is based on the average squared distance significance of the hits in the muon chambers with respect to the linear extrapolation of the tracks from the tracking system. True muons tend to have a much narrower distribution than the other particles incorrectly selected by the IsMuon requirement.
- A third level of the identification procedure uses a combined log-likelihood, computed for each track and mass hypothesis using the muon system, RICH and calorimeter systems.

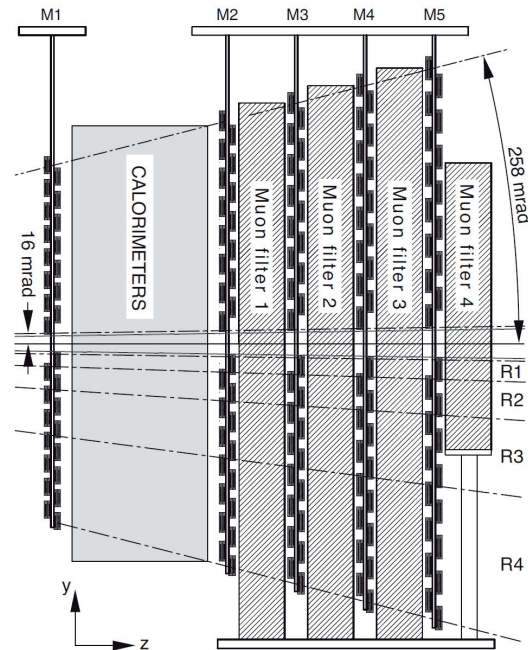


Figure 2.14 – Schematic view of the muon system [56].

2.5 Trigger

The trigger system is an essential component of the experiment to ensure a high selection efficiency for the interesting processes while removing most of the background. It consists of two stages. The Level-0 (L0) trigger implemented at the hardware level and the High-Level Trigger (HLT) implemented in software and running on a dedicated computer farm [58].

2.5.1 Hardware trigger (L0)

In order to perform the read out of the detector, the rate of visible interactions must be reduced from ~ 13 MHz down to 1 MHz. This is done with the L0 trigger, which must to provide a decision within less than $4 \mu\text{s}$. Given the high rate, the only systems with available information in such a short time and that can contribute efficiently to the decision are the calorimeter and the muon systems, as well as the Pile-Up system (Fig. 2.15). The latter consists of two backward VELO stations, called “veto stations”, composed only of r -sensors, which provide a fast estimate of the number of primary vertices identified in each event.

The calorimeter system is used to trigger on electron, photon and hadrons, and the number of hits in the SPD provides an estimate of the total number of charged particles in the event. Several trigger lines are defined. The hadronic trigger requires a high E_T cluster in the HCAL, and a match with a cluster in the ECAL. The photon trigger decision is based on the highest E_T ECAL cluster with corresponding hits in the PS detector but none in the SPD, since the latter

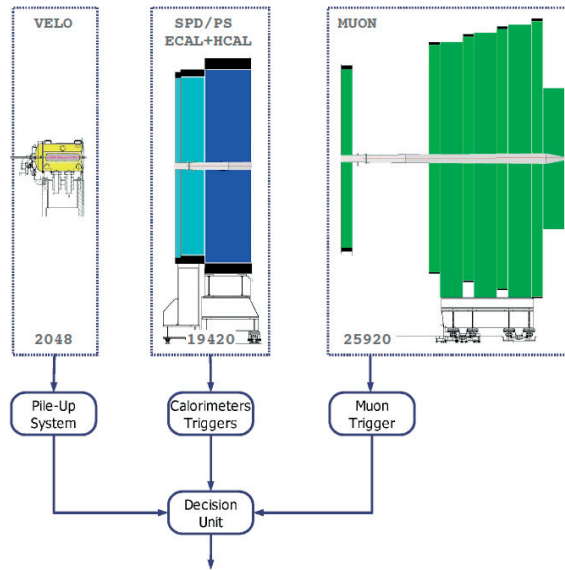


Figure 2.15 – Sources of input to the L0 trigger, with the corresponding number of channels that are read out synchronously at the 40 MHz nominal LHC frequency [44].

only gives a signal for charged particles. The trigger decision for the electrons is similar to that for the photons but requires a match with a signal in the SPD. The third input to the L0 trigger is given by the muon system. The reconstruction algorithm looks for either one or two high momentum muons in each of the muon stations and then, extrapolating with a straight line, searches for corresponding hits in all the other stations. The division of the total 1 MHz bandwidth between the different L0 trigger lines is decided on the basis of the physics reach. The output rate of the L0 muon trigger is set to 400 kHz, while it is around 450 kHz for the hadronic line and 150 kHz for the electromagnetic lines. About 10% of the events are triggered by more than one L0 trigger type.

2.5.2 Software trigger (HLT)

Event accepted by the L0 trigger are fed to HLT, which is divided in two stages. The first stage (HLT1) reduces the event rate from 1 MHz to 70 kHz. The reconstruction is limited by the computing power and includes the evaluation of track segments in the VELO, which are required to have a large impact parameter (IP) or match hits in the muon chambers. The tracks search is then extended to the tracking system. The events passing the HLT1 requirements are then processed in the second stage (HLT2), which reduces the output rate to 5 kHz. At this level, all the tracks with a p_T larger than 300 MeV/c are reconstructed.

In order to reduce the high background rate while keeping a large efficiency for specific signals, exclusive trigger lines are implemented in HLT2, together with inclusive trigger lines selecting events with the topology of B or D meson decays. The latter are based on the selection of two-, three- and four-track vertices displaced from the PV. This algorithm, known as the

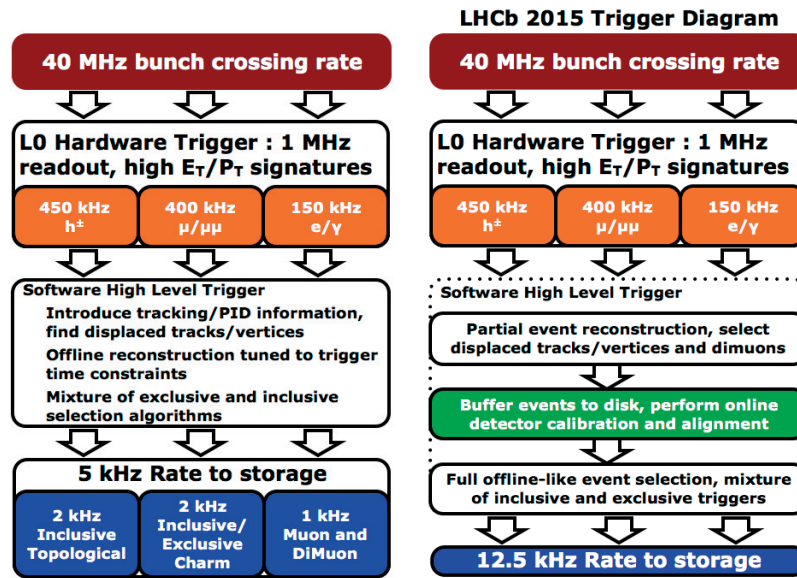


Figure 2.16 – Schematic representation of the trigger data flow in Run 1 (left) and Run 2 (right) [60].

“topological trigger”, is based on a multivariate selection, which is a modified version of the Boosted Decision Tree algorithm [59].

2.5.3 Trigger in Run 2

In Run 2 the L0 level has been optimised in terms of bandwidth division, but is identical to that of Run 1 in its structure. While in Run 1 the HLT operation was synchronous (the events had to be quickly processed by HLT1 before being sent to the slower HLT2 level), the two HLT stages are run asynchronously in Run 2. This required a change in the flow of the data. All the events passing the HLT1 selection are buffered on local disks and only later processed by HLT2 (Fig. 2.16). This procedure allows the alignment and calibration of the detector to be performed online, which gives the possibility to reconstruct the data with the same quality as in the offline procedure [60].

This new data flow allows a more efficient trigger selection for relevant decay channels, especially for the high rate charm decays. To take advantage of this possibility a new dedicated trigger has been designed, called Turbo Stream (to be distinguished from the standard Full Stream flow). This approach allows physics analyses to be performed just with data coming directly from the exclusive trigger lines, a few hours after data taking [61].

The efficiency of the system has been improved also for the standard Full Stream trigger, by modifications of the algorithms of the most important trigger lines. One example is the improvement at HLT1 level, where single- and two- track multivariate analysis (MVA) algorithms have been introduced. Thanks to additional computing resources and code optimization, the tracks are reconstructed down to $p_T = 500 \text{ MeV}/c$.

2.6 Analysis software

Physics analysis is performed within the GAUDI [62] software framework. In the following the most important software packages are described, including those used to produce the Monte Carlo (MC) simulation of the decays under study and emulate the detector response. The use of MC samples is important in the estimation of signal efficiencies, especially for rare decays.

- The **GAUSS** software takes care of the production of MC samples. It uses several applications for the different aspects of the simulation. The pp collisions are generated using PYTHIA [63], while the EVTGEN [64] application is responsible for the decay of the hadronic particles, including processes such as neutral meson mixing and resonant structures in multi-body final states. The final-state radiation is handled by PHOTOS [65] and finally GEANT [66] simulates the interaction of the particles with the detector.
- The digitization of the **GAUSS** output is provided by the **BOOLE** application, which emulates the electronic response and the hardware trigger stage, providing an output with a format identical to that of real data.
- The trigger software is run both on simulated and real data using the **MOORE** application, with the only difference that in data only the events passing the trigger requirements are saved, while in simulation all the events are kept with a flag indicating if they would pass or not the trigger decision.
- The **BRUNEL** software performs the reconstruction of the event and is run on both real and simulated data. It uses the tracking information to measure the trajectory of the particles and it executes the particle identification algorithms.
- The last step is performed by the **DAVINCI** application, which reconstructs and selects the signal decay chain of interest based on the available kinematical, topological and identification information.

2.7 Upgrade for Run 3

Run 2 will end in 2018, followed by a two-year shutdown period. The main purpose of the Long Shutdown 2 (LS2) is the upgrade of the LHC injectors. Moreover LHC will profit from this period for a full maintenance and consolidation of all the equipment. In particular the dipole magnet will be trained to sustain an operation at the design pp collision energy of $\sqrt{s} = 14$ TeV. During Run 3, the instantaneous luminosity in LHCb will increase up to $L = 2 \times 10^{33} \text{ cm}^2 \text{ s}^{-1}$. The LHCb detector, as it is now, is not able to cope with such high luminosity. In particular, the current L0 trigger system (with its 1 MHz output rate) limits the possibility to exploit the increase in luminosity. The strategy is therefore to remove the hardware trigger and to process the 40 MHz event rate directly with a flexible software trigger, where selection criteria similar to those applied offline will be used [67]. The present Turbo stream, described above, is a first

prototype in view of this trigger configuration.

In addition to the new readout system, several sub-detectors will be replaced with new ones in order to cope with the high rate, the high detector occupancy and the radiation damage.

- The VELO detector, essential for vertex identification and track reconstruction, will be replaced with a new pixel detector with smaller cells ($55 \times 55 \mu\text{m}^2$). Moreover, the track acceptance and the impact parameter resolution will be improved, placing the sensors closer to the beam (5.1 mm instead of 8.2 mm) [68].
- The tracking system will be completely replaced [2]. In particular, the TT planes will be replaced with a detector called Upstream Tracker (UT), keeping the same detector technology but improving the granularity and the geometrical coverage. Both the IT and OT detectors will be replaced with a Scintillating Fibre Tracker, composed of 2.5 m long scintillating fibres with 250 μm diameter and read out by silicon photo-multipliers (SiPMs) located at the end of the fibres, outside of the acceptance.
- In the RICH1 detector, placed upstream of the magnet, the aerogel (already removed in Run 2) will be replaced with a CF_4 radiator, allowing operation with higher occupancies [69].
- Due to the removal of the L0 trigger, the SPD, the PS and the first muon station will be removed.

3 $B_s^0 \rightarrow \eta' \phi$ and $B^+ \rightarrow \eta' K^+$ selection

The search for the decay $B_s^0 \rightarrow \eta' \phi$ and the determination of its branching fraction, presented in this thesis, is performed using the full sample of pp collisions recorded at LHCb during Run 1, in 2011 and 2012, which corresponds to an integrated luminosity of 3 fb^{-1} . The analysis is performed without inspecting the signal region for the full selection and optimisation procedure, as well as for the definition and validation of the fit model described in Chapter 4. The analysis uses the decay mode $B^+ \rightarrow \eta' K^+$ as normalisation and control channel. This mode yields a clear and abundant signal and has the most precisely known branching fraction amongst all charmless $B \rightarrow \eta' X$ modes. In this chapter, we present the reconstruction and the selection criteria for the candidates of the searched signal and normalisation modes.

3.1 Selection strategy

The decays $B_s^0 \rightarrow \eta' \phi$ and $B^+ \rightarrow \eta' K^+$ are reconstructed through the resonance decays $\eta' \rightarrow \pi^+ \pi^- \gamma$ and $\phi \rightarrow K^+ K^-$, which have substantial and well known branching fractions [13]. The η' decay includes both $\eta' \rightarrow \rho^0 \gamma$ (followed by $\rho^0 \rightarrow \pi^+ \pi^-$) and non-resonant $\eta' \rightarrow \pi^+ \pi^- \gamma$. Although the resonant ρ^0 contribution is known to be largely dominant, we do not try to isolate it, nor to use the $\pi^+ \pi^-$ mass as fitting variable. However, we use the resonant decay as a proxy for the signal in all MC simulation studies. After the events have passed the trigger requirements, signal candidates are formed offline and required to pass a loose cut-based preselection as described in Sec. 3.3. In order to refine the sample of signal candidates a further multivariate selection is applied, as described in Sec. 3.4. The selection requirements are applied to MC simulated events in order to determine the signal efficiency for the $B_s^0 \rightarrow \eta' \phi$ signal and the $B^+ \rightarrow \eta' K^+$ normalisation channel. The efficiency ratio is used as input information in the calculation of the $B_s^0 \rightarrow \eta' \phi$ branching fraction. The selections of the signal and normalisation channels are kept as similar as possible in order to reduce the number of systematic effects to be taken into account in the ratio of efficiencies.

Table 3.1 – Samples of fully-simulated events used in the analysis.

Decay chain	\sqrt{s}	Number of events
$B_s^0 \rightarrow \eta' \phi, \eta' \rightarrow \rho^0 \gamma, \rho^0 \rightarrow \pi^+ \pi^-, \phi \rightarrow K^+ K^-$	7 TeV	0.52×10^6
$B_s^0 \rightarrow \eta' \phi, \eta' \rightarrow \rho^0 \gamma, \rho^0 \rightarrow \pi^+ \pi^-, \phi \rightarrow K^+ K^-$	8 TeV	1.03×10^6
$B^+ \rightarrow \eta' K^+, \eta' \rightarrow \rho^0 \gamma, \rho^0 \rightarrow \pi^+ \pi^-$	7 TeV	0.54×10^6
$B^+ \rightarrow \eta' K^+, \eta' \rightarrow \rho^0 \gamma, \rho^0 \rightarrow \pi^+ \pi^-$	8 TeV	1.03×10^6
$B_s^0 \rightarrow \phi \phi, \phi \rightarrow K^+ K^-, \phi \rightarrow \pi^+ \pi^- \pi^0$	7 TeV	0.55×10^6
$B_s^0 \rightarrow \phi \phi, \phi \rightarrow K^+ K^-, \phi \rightarrow \pi^+ \pi^- \pi^0$	8 TeV	1.01×10^6
$B^0 \rightarrow \phi K^*(892)^0, \phi \rightarrow K^+ K^-, K^*(892)^0 \rightarrow K^+ \pi^-$	7 TeV	2.04×10^6
$B^0 \rightarrow \phi K^*(892)^0, \phi \rightarrow K^+ K^-, K^*(892)^0 \rightarrow K^+ \pi^-$	8 TeV	4.02×10^6
$B^0 \rightarrow \phi K_1(1270)^0, \phi \rightarrow K^+ K^-, K_1(1270)^0 \rightarrow K^+ \pi^- \pi^0$	7 TeV	0.92×10^6
$B^0 \rightarrow \phi K_1(1270)^0, \phi \rightarrow K^+ K^-, K_1(1270)^0 \rightarrow K^+ \pi^- \pi^0$	8 TeV	1.94×10^6

3.2 Simulation

Samples of simulated events are needed in order to emulate and optimise the selection in data, train the multivariate classifier, calculate the selection efficiencies, and study possible backgrounds. For this analysis, samples of $\sim 1.5 \times 10^6$ events have been produced for both $B_s^0 \rightarrow \eta' \phi$ and $B^+ \rightarrow \eta' K^+$ decays. Samples of simulated $B^0 \rightarrow \phi K^*(892)^0$, $B^0 \rightarrow \phi K_1(1270)^0$ and $B_s^0 \rightarrow \phi \phi$ decays have also been used in order to study their contributions to the background. The event generation follows the procedure described in Sec. 2.6. The simulated samples are produced using both 2011 and 2012 data-taking conditions, in the same proportion as in real data. The model used to generate the mentioned decays forces the particle to decay in the final state of interest. All the final state tracks are required to be within the LHCb acceptance. For the signal and normalisation channels, the model used in EVTGEN [64] for the η' decay considers only the dominant $\rho^0 \rightarrow \pi^+ \pi^-$ contribution, while the precise proportion of the phase space (PHSP) final state $\pi^+ \pi^- \gamma$ is unknown. The possible data-MC discrepancies due to this assumption cancel out in the final computation of the branching fraction ratio thanks to the use of the normalisation channel. The decay model used for the $\eta' \rightarrow \rho^0 \gamma$ generation (SVP_HELAMP [64]) describes the two-body decay of a scalar to a vector (ρ^0) and a photon, allowing for the specification of the helicity amplitudes for the final state particles. Table 3.1 reports all the specifications for each of the MC samples used in the analysis.

3.3 Trigger and preselection requirements

3.3.1 Trigger requirements

In the event reconstruction the trigger constitutes the first stage of the selection. The trigger decision for each reconstructed candidate is classified as TOS (Trigger On Signal) if the particles associated with the signal candidate triggered the event and as TIS (Trigger Independent of Signal) if other particles, which are not associated with the signal candidate, triggered the

Table 3.2 – List of trigger lines used at each trigger level.

L0	HLT1	HLT2
Hadron_TOS	TrackAllL0_TOS*	Topo2BodyBBBDT_TOS
Hadron_TIS		Topo3BodyBBBDT_TOS
Photon_TIS		Topo4BodyBBBDT_TOS
Muon_TIS		
Electron_TIS		

*This requirement is more stringent than the one applied at stripping level (see Table 3.3).

event. Table 3.2 lists the trigger lines used at the various trigger levels. At the hardware trigger level, the B candidates are required to be classified as L0Hadron_TOS or L0Phys_TIS, which is the logical “or” of the hadron, muon, electron and photon lines fired by tracks in the event that are not associated with the signal candidate. The inclusion of L0Phys_TIS candidates increases the signal efficiency by 30%, as shown in Sec. 3.7.3. At the software trigger level, the B candidates are required to be classified as Hlt1TrackAllL0_TOS and Hlt2TopoNBodyBBBDT_TOS, where $N = 2, 3$ or 4 . The trigger line Hlt2IncPhi_TOS, which selects ϕ mesons inclusively, would increase the number of signal events by 5%. However, it is not used in this analysis, considering the small gain and the need for a second normalisation channel such as $B^+ \rightarrow \phi K^+$. Indeed, the Hlt2IncPhi_TOS line selects ϕ candidates not present in the normalisation channel.

3.3.2 Stripping

The first stage of the offline selection is known as “stripping”. The size of the output dataset is still large since only loose requirements on the candidates are applied. Two inclusive stripping algorithms are used for this analysis, B2CharmlessQ2B3piSelectionLine (3π line) for the $B^+ \rightarrow \eta' K^+$ and B2CharmlessQ2B4piSelectionLine (4π line) for $B_s^0 \rightarrow \eta' \phi$. In these algorithms the pion mass is assigned to all charged particles in the final state, without applying any particle identification (PID) requirements. These pions are then combined to reconstruct the decay chains $B^+ \rightarrow P^0(\rightarrow \pi^+ \pi^-) \pi^+$ or $B_s^0 \rightarrow P^0(\rightarrow \pi^+ \pi^-) P^0(\rightarrow \pi^+ \pi^-)$, where P^0 denotes a neutral resonance that decays through the strong or electromagnetic interaction. In the case of the three-body final state, the pion not coming from the P^0 decay is referred to as the bachelor pion. These requirements include loose thresholds on the p_T and χ^2 per degree of freedom (χ^2/ndf) of each track. Additional cuts are applied on the p_T of the bachelor pion, in the case of the three-body final state, and on the p_T , the vertex quality and the mass of the P^0 resonances and the B candidates. Only candidates that have fired a trigger line in HLT1 are considered. This cut is not applied in the stripping selection of the MC sample in order to calculate the trigger efficiency independently. The full list of stripping cuts can be found in Table 3.3.

Chapter 3. $B_s^0 \rightarrow \eta' \phi$ and $B^+ \rightarrow \eta' K^+$ selection

Table 3.3 – Requirements applied in the B2CharmlessQ2B3piSelectionLine (3π) and B2CharmlessQ2B4piSelectionLine (4π) stripping lines. The impact parameter χ^2 (χ_{IP}^2) requirement is applied with respect to each reconstructed primary vertex in the event. The corrected mass is defined as $m_{\text{corr}} = (m^2 + |p'_{\text{Tmiss}}|^2)^{1/2} + |p'_{\text{Tmiss}}|$, where m is the 3π or 4π reconstructed mass, and p'_{Tmiss} is the missing transverse momentum relative to the direction of flight of the B candidate as determined from its production and decay vertices.

	3 π line	4 π line
Pions		
– track fit quality	$\chi^2/\text{ndf} < 4$	< 4
– impact parameter χ^2	$\chi_{\text{IP}}^2 > 16$	> 16
– track ghost probability	< 0.5	< 0.5
– transverse momentum	$p_{\text{T}} > 0.4 \text{ GeV}/c$	$> 0.4 \text{ GeV}/c$
Bachelor pion		
– transverse momentum	$p_{\text{T}} > 1.0 \text{ GeV}/c$	—
Resonance (P^0)		
– transverse momentum	$p_{\text{T}} > 0.6 \text{ GeV}/c$	$> 0.6 \text{ GeV}/c$
– mass	$m_{\pi\pi} < 1.1 \text{ GeV}/c^2$	$< 1.1 \text{ GeV}/c^2$
– vertex quality	$\chi^2/\text{ndf} < 9$	< 9
B meson		
– mass	$m \in [4.2, 6.7] \text{ GeV}/c^2$	$\in [3.5, 5.7] \text{ GeV}/c^2$
– corrected mass	$m_{\text{corr}} < 7.0 \text{ GeV}/c^2$	$< 6.0 \text{ GeV}/c^2$
– vertex quality	$\chi^2/\text{ndf} < 6$	< 6
– transverse momentum	$p_{\text{T}} > 1.5 \text{ GeV}/c$	$> 1.5 \text{ GeV}/c$
Trigger = Hlt1Track*Decision_TOS	yes*	yes*

*The trigger requirement is applied only on data events; for simulated events, the trigger requirement is applied after the preselection in order to compute the trigger efficiency on preselected events.

3.3.3 Preselection

The B candidates filtered by the 3π stripping line are then combined with a photon to form $B^+ \rightarrow \eta' K^+$ candidates, while those filtered by the 4π stripping line are combined with a photon to form $B_s^0 \rightarrow \eta' \phi$ candidates. At this stage, the kaon mass is assigned to the kaon candidates in $B^+ \rightarrow \eta' K^+$ and $\phi \rightarrow K^+ K^-$. The DecayTreeFitter (DTF) [70] framework is used to refit the entire decay chain of each B candidate passing the stripping requirements. One can impose constraints in the fit in order to improve the resolution of the reconstructed B -candidate mass. During the refit, the four-momenta of the final-state particles are altered to their best fit values under the given constraints. In our case the decay chain is fitted constraining the reconstructed η' mass to its known value [13] (see Fig. 3.1). The ϕ mass is not constrained in the kinematic fit, because the ϕ meson natural width ($4.3 \text{ MeV}/c^2$) is somewhat larger than the detector resolution ($\sim 1 \text{ MeV}/c^2$). Therefore, there would be no gain from constraining the mass and this would also result in a small distortion of the B meson mass distribution. After the DTF algorithm is applied a set of additional cuts, presented in

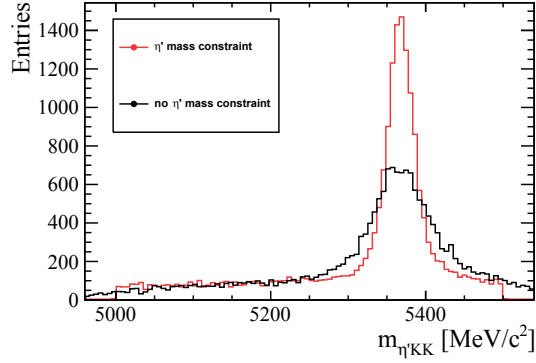


Figure 3.1 – Distribution of the reconstructed B_s^0 mass for $B_s^0 \rightarrow \eta' \phi$ simulated candidates before (black curve) and after (red curve) applying the constraint on the reconstructed η' mass to its known value [13].

Table 3.4, is applied on the reconstructed candidates. The requirement on the $\pi^+ \pi^-$ mass, $m_{\pi\pi} > 0.52 \text{ GeV}/c^2$, reduces significantly the background, including true $K_S^0 \rightarrow \pi^+ \pi^-$ decays (likely to come from $B_s^0 \rightarrow \phi K_S^0$) and true $\phi \rightarrow K^+ K^-$ decays peaking at $m_{\pi\pi} \sim 0.34 \text{ GeV}/c^2$ (coming from $B_s^0 \rightarrow \phi\phi$ decays where the two kaons of one of the ϕ mesons have been misidentified as pions). The requirement on the $K^+ K^-$ mass, $1.005 < m_{KK} < 1.035 \text{ GeV}/c^2$, selects a $\pm 20 \text{ MeV}/c^2$ window around the central value of the ϕ mass peak.

3.3.4 Particle identification requirements

Together with requirements on the transverse momentum of the photon and the B meson, the selection at this stage is refined using particle identification information. For the charged particles, and in particular to distinguish between pions and kaons, the likelihood information produced by PID detector sub-systems is added, to form a set of combined variables giving a measure of how likely are the mass hypotheses X ($X = \text{kaon, electron, proton, muon}$) under consideration for any given track relative to the pion hypothesis,

$$\text{DLL}_{X\pi} = \ln \mathcal{L}_X - \ln \mathcal{L}_\pi, \quad (3.1)$$

where \mathcal{L}_X is the PID likelihood for hypothesis X . This information is then improved by the combination with the tracking performance and the track kinematics. The combination is obtained using a neural network (NN) algorithm and the resulting variable, called ProbNN_X and varying in the range $[0,1]$, gives the Bayesian posterior probability of a particle to belong to the species X . The requirement $\text{ProbNN}_K > 0.3$ is applied to the bachelor kaon in the selection of the normalisation channel. The requirement ProbNN_π (ProbNN_K) > 0.2 is applied for the pions (kaons) forming the η' (ϕ) resonance. The cut on the pion PID has been tuned in two steps following the studies on the peaking background, as described in Sec. 3.5.

The photon identification relies on two independent estimators for the converted and non-

Chapter 3. $B_s^0 \rightarrow \eta' \phi$ and $B^+ \rightarrow \eta' K^+$ selection

Table 3.4 – Preselection requirements applied on the B candidates passing the 3π and 4π stripping lines to form $B^+ \rightarrow \eta' K^+$ and $B_s^0 \rightarrow \eta' \phi$ candidates, respectively. The final selection includes the following additional requirements: a BDT output larger than 0.1 (0.05) for $B_s^0 \rightarrow \eta' \phi$ ($B^+ \rightarrow \eta' K^+$) (Sec. 3.4), tighter PID cuts as indicated with footnotes below (Sec. 3.5) and the selection for a unique candidate per event (Sec. 3.6).

	$B^+ \rightarrow \eta' K^+$	$B_s^0 \rightarrow \eta' \phi$
Photon (converted and not-converted)		
– photon identification	$CL_\gamma > 0.1^*$	$> 0.1^*$
– photon transverse momentum	$p_T > 0.30 \text{ GeV}/c$	$> 0.30 \text{ GeV}/c$
$\eta' \rightarrow \pi^+ \pi^- \gamma$ meson		
– pion identification	$\text{ProbNN}_\pi > 0.1^{**}$	$> 0.1^{**}$
– vertex quality	$\chi^2/\text{ndf} < 9$	< 9
– $\pi\pi$ mass	$m_{\pi\pi} > 0.52 \text{ GeV}/c^2$	$> 0.52 \text{ GeV}/c^2$
– $\pi\pi\gamma$ transverse momentum	$p_T > 1.5 \text{ GeV}/c$	$> 1.5 \text{ GeV}/c$
– $\pi\pi\gamma$ mass	$m_{\pi\pi\gamma} \in [0.88, 1.04] \text{ GeV}/c^2$	$\in [0.88, 1.04] \text{ GeV}/c^2$
Bachelor kaon		
– kaon identification	$\text{ProbNN}_K > 0.3$	—
$\phi \rightarrow K^+ K^-$ meson		
– kaon identification	ProbNN_K —	> 0.2
– vertex quality	χ^2/ndf —	< 9
– mass	m_{KK} —	$\in [1.005, 1.035] \text{ GeV}/c^2$
$B_{(s)}$ meson		
– transverse momentum	$p_T > 1.5 \text{ GeV}/c$	$> 1.5 \text{ GeV}/c$
– vertex quality	$\chi^2/\text{ndf} < 6$	< 6
– mass	$m_B \in [5.0, 5.5] \text{ GeV}/c^2$	$\in [5.0, 5.6] \text{ GeV}/c^2$

*This requirement has been tightened from 0.1 to 0.2 in the final selection.

**This requirement has been tightened from 0.1 to 0.2 in the final selection.

converted candidates (Sec. 2.4.2). The variable used is the difference in log-likelihood between the photon and the background hypotheses. A probability density function, CL_γ , is built from different variables depending on the photon conversion or not [49]. It has been checked that applying the same cut for the two types of reconstructed photon leads to compatible efficiencies. The requirement, $CL_\gamma > 0.2$, has also been optimised in two steps following the peaking background studies described in Sec. 3.5.

3.4 Multivariate analysis

The background level is still high after the trigger and preselection requirements (see Fig. 3.2, left). A further selection step is needed considering the small number of expected signal events. A multivariate selection (MVA) is applied to improve the signal-to-noise ratio. A boosted decision tree classifier [71] (BDT) allows the labeling of events as signal-like or background-like,

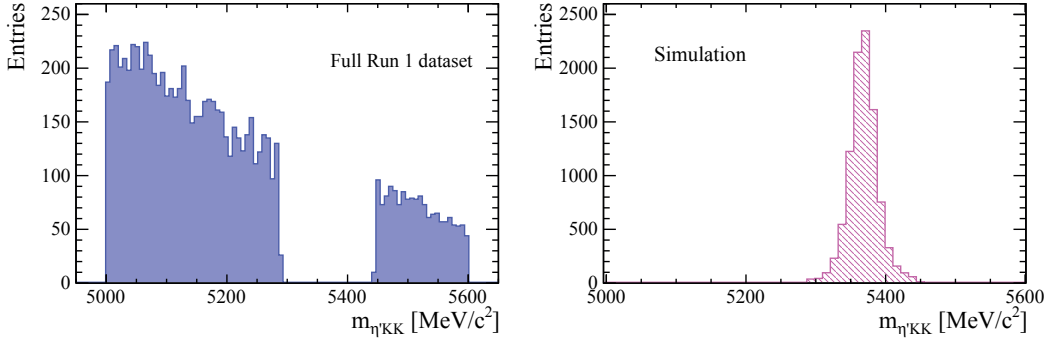


Figure 3.2 – Left: distribution of the $\eta'K^+K^-$ invariant mass for the $B_s^0 \rightarrow \eta'\phi$ candidates after preselection requirements. The signal region is not displayed. Right: $\eta'K^+K^-$ invariant mass for simulated signal MC events passing the preselection requirements.

using simultaneously several input variables as discriminators. The use of a MVA instead of a cut-based selection, in which individual requirements are placed on many variables, is more effective when the signal and background show a significant overlap in multiple degrees of freedom. The main goal of the BDT is to suppress candidates formed with random combinations of tracks, called combinatorial background. The samples used in the BDT are already pre-selected as described in Sec. 3.3. The BDT is implemented using the Scikit-learn [72] python package. The BDT is trained and tested using a signal sample of MC simulated events and a background sample of real data events. The signal and background samples are divided randomly into training and testing samples of equal size, and the testing samples are used at a later stage. Many decision trees are constructed using different sets of input variables, and the variables showing the greatest separation power are identified. At each so-called boosting iteration, weights are applied to the training events. For each iteration, the weights are modified, giving higher weight when the prediction is not correct, and the algorithm is then reapplied to the reweighted data. This allows misclassified events to have a higher chance of being correctly identified in the next decision stage. Separate BDTs are defined (even if using the same input variables) and trained for signal and control channels.

3.4.1 Input variables and data samples

For the optimisation of the multivariate selection, the following $\eta'\phi$ mass regions are defined:

- the low-mass sideband region, from 5000 to 5287 MeV/c²;
- the B_s^0 signal region, from 5287 to 5446 MeV/c²;
- the high-mass sideband region, from 5446 to 5600 MeV/c².

The BDT is trained using simulated $B_s^0 \rightarrow \eta'\phi$ events as signal in the signal region, and selected $B_s^0 \rightarrow \eta'\phi$ data candidates falling in the low-mass or high-mass sidebands as background (see Fig. 3.2). For the latter category, one would ideally use only the high-mass sideband,

Table 3.5 – Definition of the nine variables used as input to the multivariate selection. The PV notation refers to the reconstructed primary vertex with respect to which the B candidate has the smallest impact parameter χ^2 .

<u>Variables related to geometry and vertexing:</u>
1. B impact parameter with respect to the PV
2. Cosine of the angle between the vector from the PV to the B decay vertex and the B momentum direction
3. Distance of flight of the B candidate
4. χ^2/ndf of the B vertex
5. Smallest increase in χ^2 when adding one track to the B vertex
6. Smallest increase in χ^2 when adding a second track to the combination that has the smallest χ^2 increase when adding one track
7. Sum of the χ^2 of the impact parameters with respect to the PV of the four (or three) tracks forming the B candidate
<u>Kinematic variables:</u>
8. Transverse momentum of the photon candidate
9. Transverse momentum of the η' candidate

since the aim of the multivariate selection is to distinguish between signal and combinatorial background. However, due to the small data statistics, the low-mass sideband, which is more likely to contain non-combinatorial background, is used as well. For the same reason a unique BDT is trained for the full Run 1 dataset (2011 and 2012 data). To minimise biases in the final selection, the data and MC samples are randomly divided into two sub-samples and two BDTs are defined. Each BDT is trained, tested and optimised on one sample, and is then applied for the event selection to the other sample and *vice versa*. The BDTs are constructed from the nine variables listed in Table 3.5. No variable related to the ϕ resonance is used in the BDT for the searched signal, in order to exploit the same variables in the two channels and hence minimise the systematic uncertainties in the ratio of efficiencies. The first seven variables are purely geometrical or related to vertex reconstruction, while the last two variables are kinematical. The two kinematical variables provide significant discrimination between signal and background. Indeed, most of the η' background comes from the association of a random low p_T photon with a pair of pion tracks, and vertex-related variables cannot discriminate against such background.

Another interesting kinematic variable is the pion helicity angle, defined in the $\pi^+ \pi^-$ rest-frame as the angle between the π^+ and the η' flight directions. The distribution of the cosine of this angle has the characteristic shape shown in Fig. 3.3 for the signal, while it is expected to be mostly flat for the background, for which the contribution from real η' mesons has been checked to be small. Adding this variable in the multivariate analysis only brings a modest improvement to the BDT performance, because of its correlation with the photon and η' transverse momenta. Furthermore, the distribution of this variable for the signal is not perfectly modeled in the simulation, which assumes $\eta' \rightarrow \rho^0 \gamma$ and neglects the non-resonant

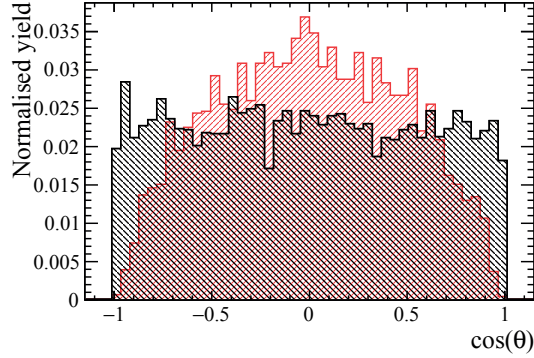


Figure 3.3 – Distribution of the cosine of the pion helicity angle for the $B_s^0 \rightarrow \eta' \phi$ MC simulated signal (hatched red) and for B_s^0 data sidebands (hatched black).

$\eta' \rightarrow \pi^+ \pi^- \gamma$ contribution. For all these reasons the helicity angle is not used in the selection, but is kept as a look-back variable in case a $B_s^0 \rightarrow \eta' \phi$ signal is observed.

3.4.2 Verifications on data-MC compatibility

Since a simulated $B_s^0 \rightarrow \eta' \phi$ sample is used for the BDT training as proxy to study the signal behaviour, it is important to verify that it reproduces well the true signal characteristics. Indeed, a mis-modelling of the simulated sample would imply not only a wrong estimate of the effective power of the BDT, but also a wrong estimate of its efficiency. Using the control channel as proxy for the signal, it has been checked that the distributions of the nine input variables as well as the BDT output are correctly described in the MC simulation. For both data and simulation, the distributions of all variables are extracted using the *sPlot* technique [73] applied to the one-dimensional fit of the $B^+ \rightarrow \eta' K^+$ mass distribution shown in Fig. 3.4.

Figure 3.5 demonstrates that the simulation reproduces in a satisfactory manner the distributions of all nine variables used in the BDT. As shown in Fig. 3.6, the simulation also reproduces the distribution of the BDT output, from which we conclude that the correlation between the input variables is adequately described in the MC simulation. However, small differences are present. The efficiency of a cut on the BDT output estimated from simulation differs from the true efficiency measured with data by an absolute 3 – 5%, depending on the cut value in the range $[-0.1, 0.2]$. This discrepancy is sufficiently small to be included as a systematic uncertainty on the signal efficiency.

3.4.3 BDT performance and optimization

Figure 3.7 shows the distributions of the BDT output for $B_s^0 \rightarrow \eta' \phi$ MC signal and data sideband background. Figure 3.8 shows the signal efficiency for a given background efficiency or rejection when a requirement on the BDT output is applied. The optimisation of the requirement

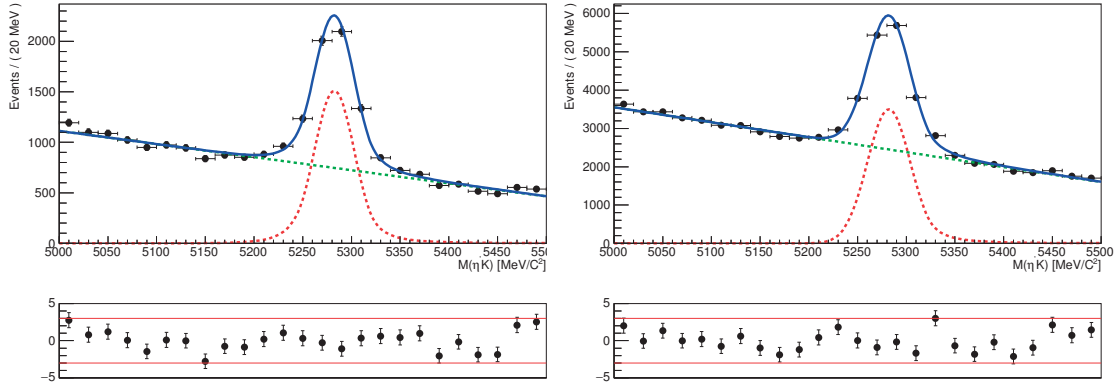


Figure 3.4 – Mass distribution of the preselected $B^+ \rightarrow \eta' K^+$ candidates in the 2011 (left) and 2012 (right) datasets falling in a tight $\pi^+ \pi^- \gamma$ mass window around the η' meson ($|m_{\pi\pi\gamma} - 957.8 \text{ MeV}/c^2| < 27 \text{ MeV}/c^2$). The blue curves show the results of fits with the following components: the signal (red curve) and the combinatorial background (green curve). The bottom plots show the fit residuals, expressed in statistical standard deviations.

on the BDT output is performed using the figure of merit (FoM) [74]

$$\text{FoM} = \frac{\varepsilon(t)}{a/2 + \sqrt{B(t)}}, \quad (3.2)$$

where $\varepsilon(t)$ is the signal MC efficiency for a given BDT cut t , $B(t)$ is the number of background events in the signal region estimated from the data sidebands and $a = 5$ is the significance for which we intend to optimise. The FoM clearly reaches its maximal value for a BDT cut value between 0 and 0.2 (see Fig. 3.9). Based on these results the working point of the BDT algorithm has been set at 0.1. For the control channel a cut at 0.05 on the BDT variable is chosen as optimal.

As a check, an alternative optimisation is performed for various values of the $B_s^0 \rightarrow \eta' \phi$ branching fraction. Pseudo-experiments are generated with a model containing only signal and combinatorial background, and are then analysed with a simple two-dimensional maximum likelihood fit to the B_s^0 and η' masses. The signal significance, determined using Wilks' theorem [75], is found to reach its maximum for a BDT requirement in agreement with that obtained using the method of Ref. [74]. In particular it reaches its maximum at 0.1 assuming a signal branching fraction of 4×10^{-6} .

3.5 Physics background studies

The BDT selection is mostly useful in reducing the combinatorial background. In case of presence of partially-reconstructed B decays, the BDT could be less efficient. Indeed, these B decays for which one or more particles are either mis-reconstructed or not reconstructed and

3.5. Physics background studies

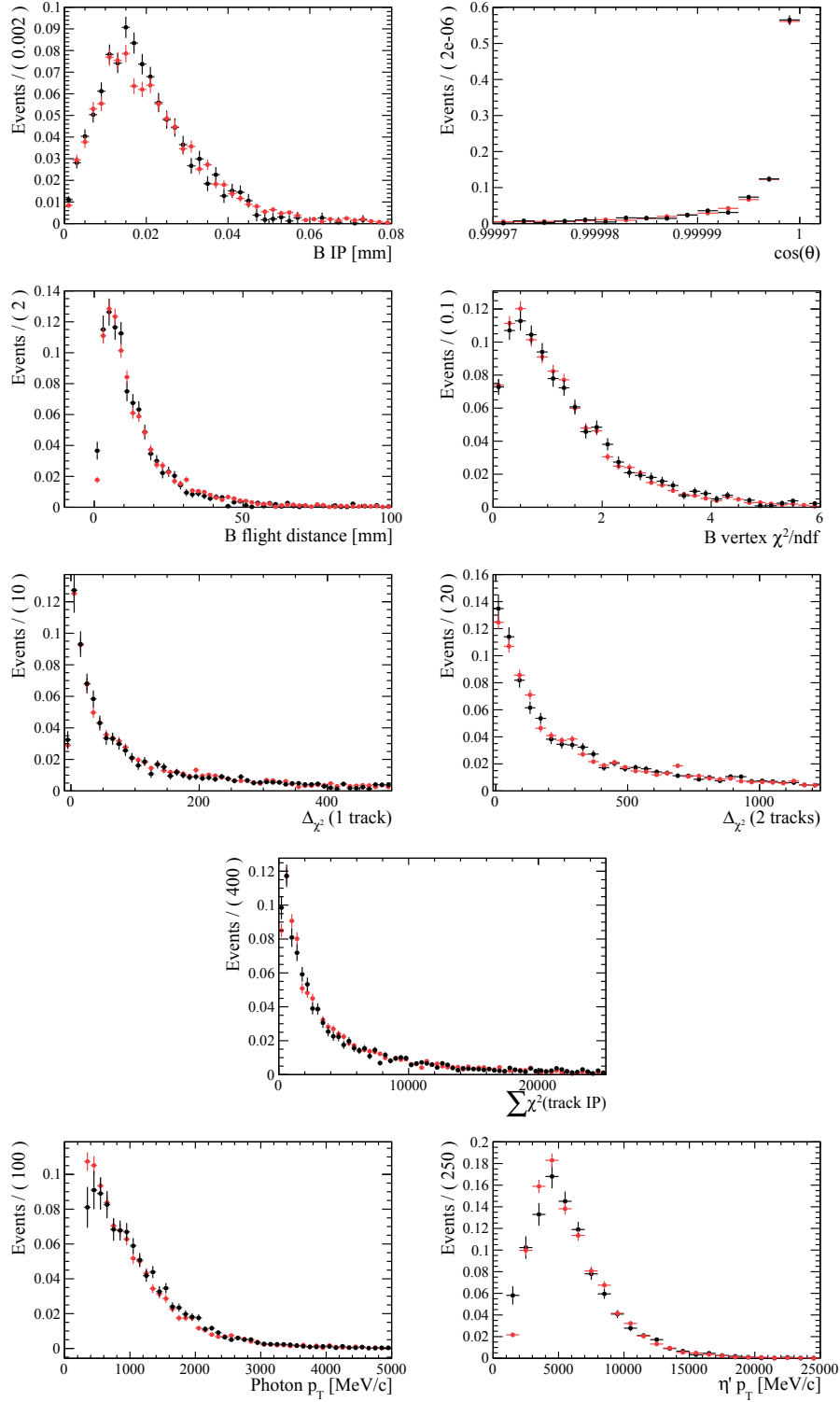


Figure 3.5 – Distributions of the nine variables used as input to the multivariate selection (from left to right and top to bottom, in the same order as listed in Table 3.5), for the $B^+ \rightarrow \eta' K^+$ control channel. The black and red distributions are obtained using the sPlot technique for signal data and signal MC for the 2012 conditions, respectively.

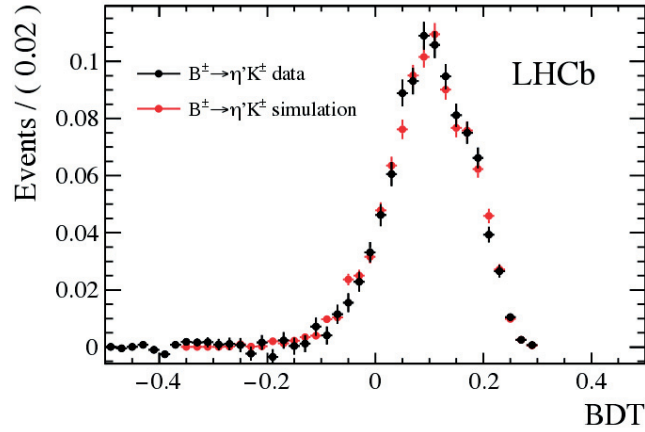


Figure 3.6 – Distributions of the BDT output for the $B^+ \rightarrow \eta' K^+$ control channel, obtained using the sPlot technique for signal data (black) and signal MC (red) for the 2012 conditions.

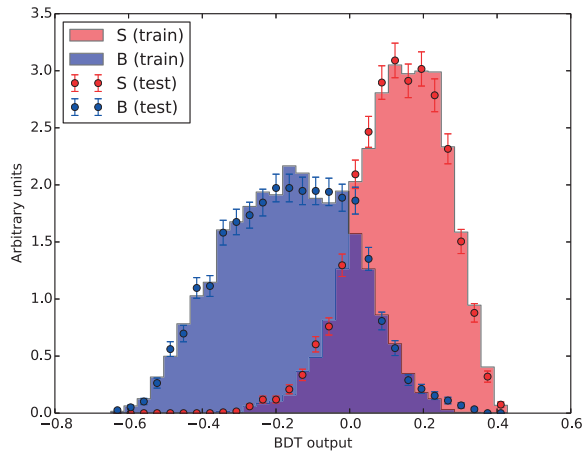


Figure 3.7 – Distributions of the BDT output for the $B_s^0 \rightarrow \eta' \phi$ MC signal (red) and for the $B_s^0 \rightarrow \eta' \phi$ data candidates falling in the B_s^0 mass sidebands (blue).

which usually fall in the low-mass sideband, have many similarities to the signal and therefore the BDT can not efficiently discriminate between the two components. Figure 3.10 shows the signal efficiency and the fraction of surviving background candidates from the high-mass and low-mass sidebands as a function of the BDT cut, selecting the candidates with BDT output larger than the cut value. For the low-mass sideband, we observe less background reduction than for the high-mass sideband. This shows that the BDT cut acts more effectively on the high-mass sideband, which contains mostly combinatorial background, and is a hint of the presence of a partially-reconstructed component (which is more signal-like than pure combinatorial background) in the low-mass sideband.

Dedicated studies are performed on charmless backgrounds which have similar or identical final-state particles as the signal. If every particle has been correctly identified, and all particles

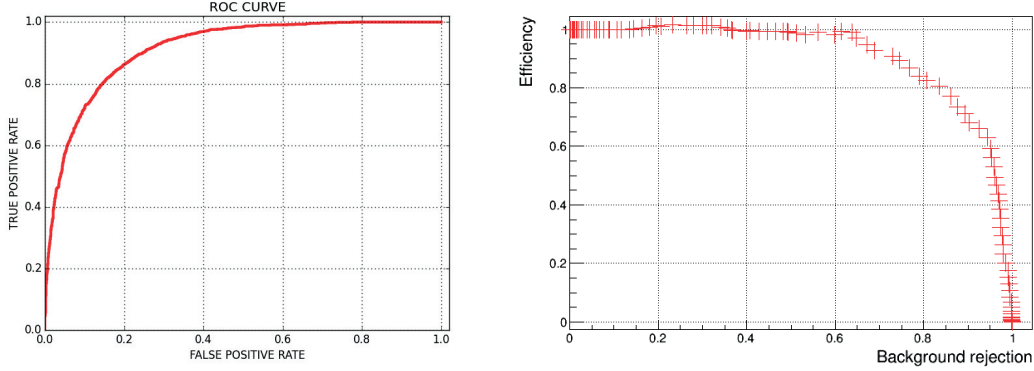


Figure 3.8 – Signal efficiency for a given background efficiency (left) or background rejection (right), when a requirement on the BDT output is applied.

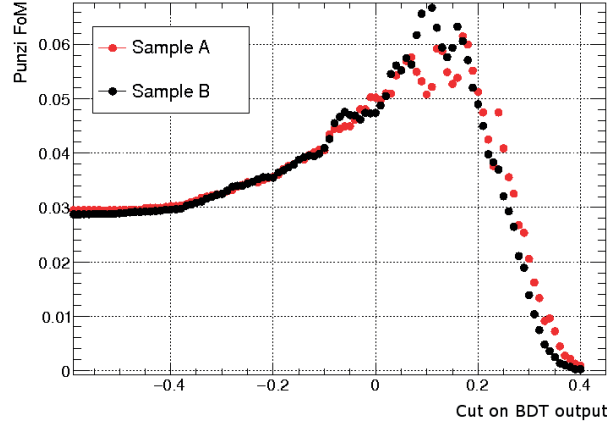


Figure 3.9 – Figure of merit defined by Eq. 3.2 as a function of the cut value on the BDT output. The two sets of points (red and black) correspond to the two BDTs, each trained and optimised on half of the available data and MC samples for the 2012 conditions.

originate from the same B decay, these backgrounds peak in the same B mass region as the signal and cannot be distinguished from the signal in the B mass distribution. If one of the particles is misidentified or not reconstructed, the resulting B mass peak can be shifted from the nominal value and have a wider mass distribution than signal. It is important to identify such backgrounds, either to include them in the final fit model or to check they are not peaking and determine how to control them in data. Using MC simulation, we look at a few modes that are potential sources of background. Reconstructing these decays as $B_s^0 \rightarrow \eta' \phi$ candidates, we can infer their contribution to the background. Contamination from the following sources has been identified:

- $B^0 \rightarrow \phi K^* (892)^0$, $K^* (892)^0 \rightarrow K^+ \pi^-$ decays, for which a kaon is misidentified as a pion and a random photon is added.

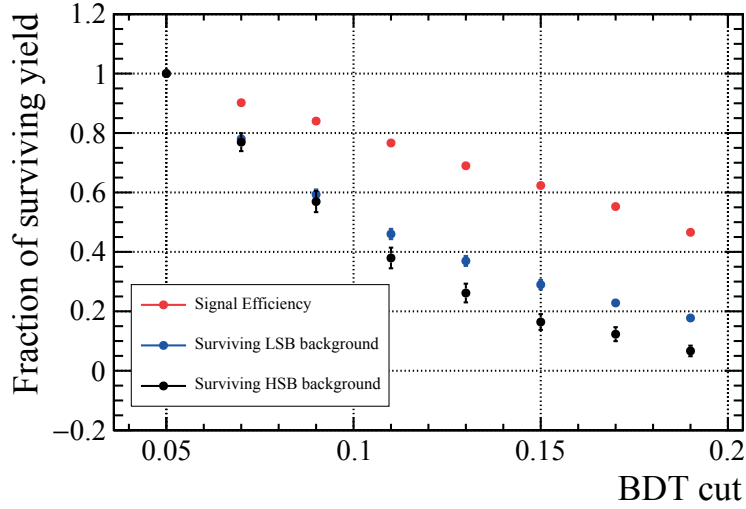


Figure 3.10 – Efficiency of the BDT selection for MC $B_s^0 \rightarrow \eta' \phi$ signal (red), low-mass data sideband (blue) and high-mass data sideband (black), as a function of the BDT cut value.

- $B^0 \rightarrow \phi K_{\text{res}}^0$, $K_{\text{res}}^0 \rightarrow K^+ \pi^- \pi^0$ decays, where K_{res}^0 is a kaon resonance for which the charged kaon is misidentified as a pion and either a random photon, or one photon from the $\pi^0 \rightarrow \gamma\gamma$ decay is added. One of the most problematic modes in this family is $B^0 \rightarrow \phi K_1(1270)^0$. Since the branching fractions of $B^+ \rightarrow J/\psi K^*(892)^+$ $((1.43 \pm 0.08) \times 10^{-3})$ and $B^+ \rightarrow J/\psi K_1(1270)^+$ $((1.8 \pm 0.5) \times 10^{-3})$ are similar [13], we expect this mode to have a branching fraction of the order of 10^{-5} , as for $B^0 \rightarrow \phi K^*(892)^0$. In the model used for this channel all the possible decays of the $K_1(1270)^0$ resonance to the $K^+ \pi^- \pi^0$ final state are considered, with a total branching fraction of 0.86.
- $B^+ \rightarrow \phi K_{\text{res}}^+$, $K_{\text{res}}^+ \rightarrow K^+ \pi^- \pi^+$ decays, where one of the tracks is lost and a random photon is added in the reconstruction of the η' candidate. These contaminations are found to be negligible and not peaking.
- $B_s^0 \rightarrow \phi\phi$ decays, where one of the two ϕ mesons decays in the $\pi^+ \pi^- \pi^0$ final state, with a large branching fraction of $(15.3 \pm 0.3)\%$ [13]. In this case, either a random photon, or one photon from the $\pi^0 \rightarrow \gamma\gamma$ decay is combined with the pion pair to build the η' candidate.

The backgrounds with misidentified particles are strongly reduced thanks to an optimisation of the pion PID requirements ($\text{ProbNN}_\pi > 0.2$). Figure 3.11 (top) shows the MC simulated distributions for the signal and the backgrounds with misidentified pion candidates. The requirements on ProbNN_π reduces the background by 20% in data (mostly in the high-mass sideband), while preserving 96% of the signal. Another requirement helpful in reducing the partially-reconstructed background is that on CL_γ ($\text{CL}_\gamma > 0.2$), for which the background distribution is significantly different from that of the signal as can be observed in Fig. 3.11 (middle).

3.5. Physics background studies

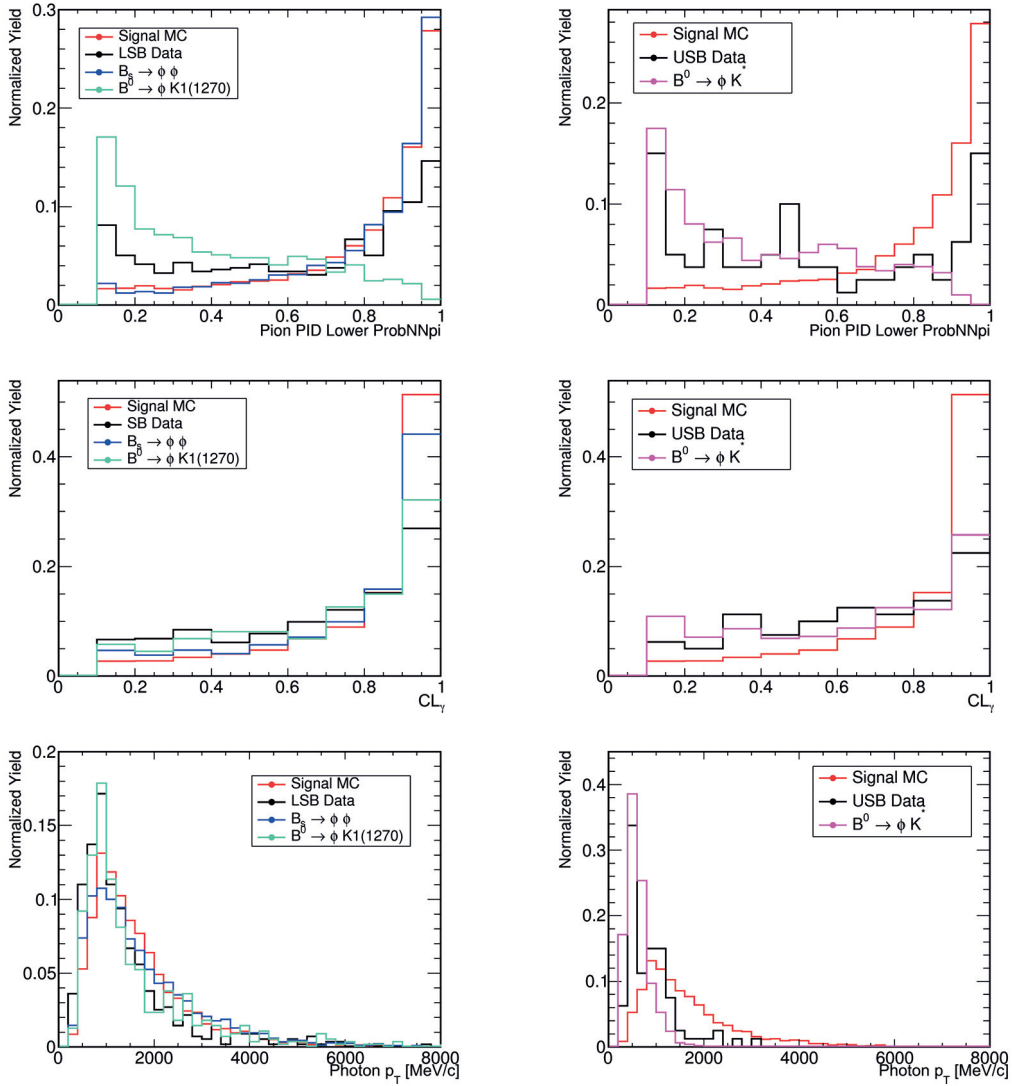


Figure 3.11 – ProbNN $_{\pi}$ (top), CL_{γ} (middle) and photon p_T (bottom) distributions for the low-mass data sideband, $B_s^0 \rightarrow \phi\phi$, $B^0 \rightarrow \phi K_1(1270)$ and signal MC (left), as well as for the high-mass data sideband, $B^0 \rightarrow \phi K^*(892)$ and signal MC (right).

Chapter 3. $B_s^0 \rightarrow \eta' \phi$ and $B^+ \rightarrow \eta' K^+$ selection

Table 3.6 – Fraction of events with multiple candidates in the selected data samples collected in 2011 and 2012.

Selection	Sample	Fraction in data (%)	Fraction in signal MC (%)
$B^+ \rightarrow \eta' K^+$	2011	3.0	5.2
$B^+ \rightarrow \eta' K^+$	2012	3.3	5.1
$B_s^0 \rightarrow \eta' \phi$	2011	0.8	2.8
$B_s^0 \rightarrow \eta' \phi$	2012	1.0	2.1

The rejection of the $B_s^0 \rightarrow \phi\phi$ background is more complicated, because of the similarity of the final state with the searched signal. The PID requirements cannot help since all the particles in the final state are of the same species and the reconstructed photon is identified as one of the two photons coming from the π^0 decay. The similar topology and kinematics are also the reason which makes the BDT selection less effective with respect to the $B^0 \rightarrow \phi K_1(1270)^0$ and $B^0 \rightarrow \phi K^*(892)^0$ backgrounds. This can be shown for instance looking at the p_T distributions for signal and physics background, keeping in mind that this variable is the most powerful discriminating variable used as input to the BDT algorithm. The p_T of the photon in $B^0 \rightarrow \phi K^*(892)^0$ (Fig. 3.11 bottom right) is on average lower (random low energy γ) and more similar to the combinatorial background, while it is similar to the signal for the $B_s^0 \rightarrow \phi\phi$ decay. The expected yields of the $B_s^0 \rightarrow \phi\phi$, $B^0 \rightarrow \phi K^*(892)^0$ and $B^0 \rightarrow \phi K_1(1270)^0$ backgrounds, presented in Sec. 3.9, are not negligible but have small contributions under the signal peak.

3.6 Multiple candidates and final sample size

The data samples after the final selection contain a small fraction of events with multiple candidates. This is due to the fact that many low p_T photons can be combined with the pion pair to form η' candidates. The fraction of events with multiple candidates, estimated in the full selected B and η' mass ranges, is presented in Table 3.6 for both $B^+ \rightarrow \eta' K^+$ and $B_s^0 \rightarrow \eta' \phi$ decays. Since the presence of more than one candidate per event is due to random photon associations, we select in each event the B_s^0 candidate with the highest CL_γ for the photon. The mass distributions of the selected and rejected candidates in events with multiple $B^+ \rightarrow \eta' K^+$ candidates are shown in Fig. 3.12 for data and in Fig. 3.13 for simulation. Selecting the candidate with highest CL_γ slightly increases the purity of the selection. Possible biases due this choice are taken into account performing studies with pseudo-experiments. With all selection criteria applied, the final data sample contains 430 $B_s^0 \rightarrow \eta' \phi$ candidates and 22681 $B^+ \rightarrow \eta' K^+$ candidates.

3.6. Multiple candidates and final sample size

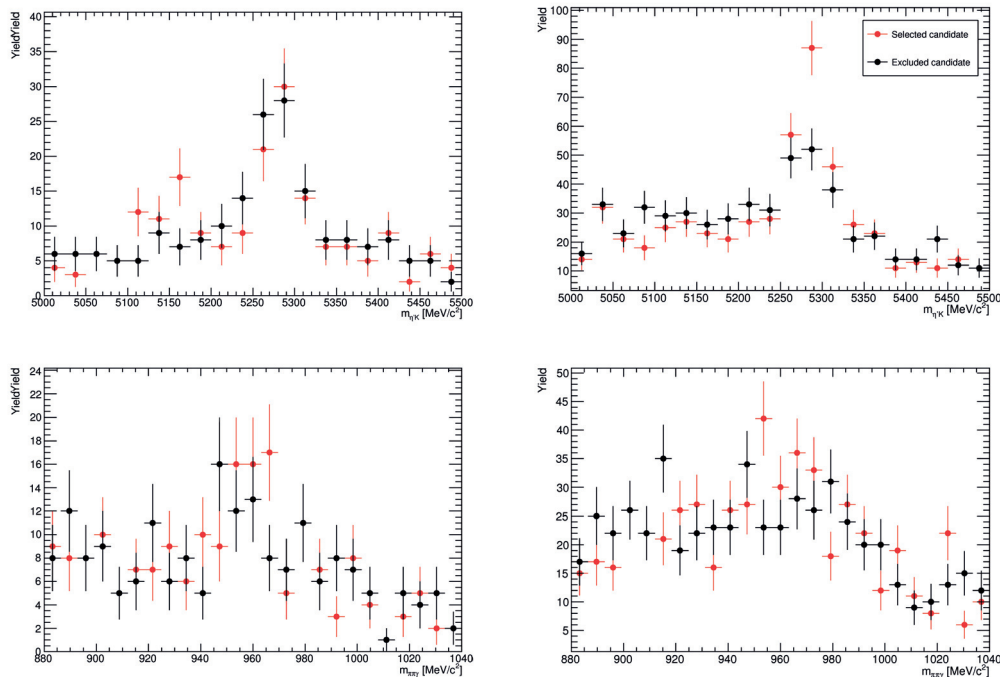


Figure 3.12 – B^+ (top) and η' (bottom) mass distributions for the $B^+ \rightarrow \eta' K^+$ candidates kept (red) and rejected (black) in selected events with multiple candidates, in the 2011 (left) and 2012 (right) data samples.

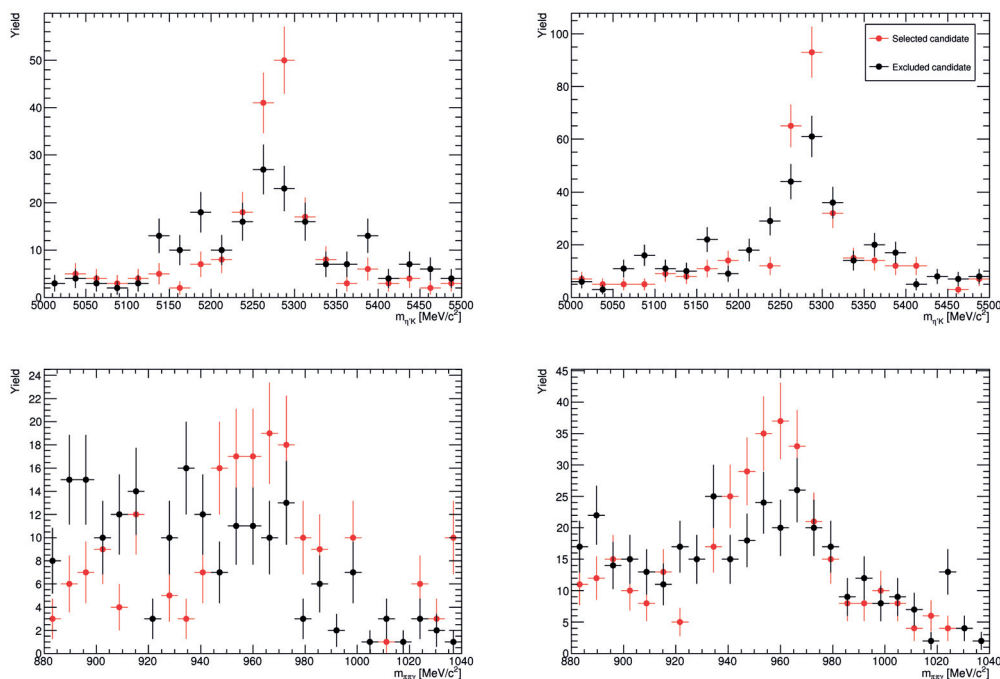


Figure 3.13 – B^+ (top) and η' (bottom) mass distributions for the $B^+ \rightarrow \eta' K^+$ candidates kept (red) and rejected (black) in selected events with multiple candidates, in the 2011 (left) and 2012 (right) MC samples.

3.7 Selection efficiencies

3.7.1 Breakdown of the efficiencies

The selection efficiencies for the signal and the normalisation modes are needed for the computation of the signal branching fraction. For each decay mode of interest the total selection efficiency ϵ^{total} is factorized as

$$\begin{aligned} \epsilon^{\text{total}} = & \epsilon^{\text{geom}} \times \epsilon^{\text{presel|geom}} \times \epsilon^{\text{PID|presel\&geom}} \times \epsilon^{\text{trig|PID\&presel\&geom}} \times \\ & \epsilon^{\text{BDT|trig\&PID\&presel\&geom}} \times \epsilon^{\text{CL+PID|BDT\&trig\&PID\&presel\&geom}} \times \\ & \epsilon^{\text{uniq|CL+PID\&BDT\&trig\&PID\&presel\&geom}}, \end{aligned} \quad (3.3)$$

where

- ϵ^{geom} is the geometrical acceptance, measured as the efficiency of the requirements imposed in simulation at the generator level on the tracks from the B decay of interest (Sec. 3.2);
- $\epsilon^{\text{presel|geom}}$ is the reconstruction and preselection efficiency; it is calculated as the fraction of simulated decays (generated in the geometrical acceptance) that pass the preselection without any charged hadron identification or trigger requirements (requirements listed in Table 3.4, excluding PID);
- $\epsilon^{\text{PID|presel\&geom}}$ is the efficiency of pion and kaon identification requirements of the preselection on reconstructed decays of interest passing the rest of the preselection (PID requirements listed in Table 3.4);
- $\epsilon^{\text{trig|PID\&presel\&geom}}$ is the combined efficiency of the used trigger lines on preselected decays;
- $\epsilon^{\text{BDT|trig\&PID\&presel\&geom}}$ is the efficiency of the BDT selection;
- $\epsilon^{\text{CL+PID|BDT\&trig\&PID\&presel\&geom}}$ is the efficiency of the additional particle identification requirements on preselected events passing the BDT selection ($\text{ProbNN}_\pi > 0.2$ and $\text{CL}_\gamma > 0.2$, see Sec. 3.5);
- $\epsilon^{\text{uniq|CL+PID\&BDT\&trig\&PID\&presel\&geom}}$ is the efficiency of the requirement to eliminate multiple candidates.

All these factors are shown in Table 3.7 for the channels of interest. They are determined from MC simulation, except for PID and L0 hadron efficiencies, for which calibration samples from real data are used. Each efficiency is computed as the ratio of two signal yields, after and before the appropriate set of requirements is applied. These yields are obtained as the result of a mass fit, using the same mass model as the one described in the caption of Fig. 3.4, as opposed to counting the number of truth-matched MC signal candidates.

3.7. Selection efficiencies

Table 3.7 – $B^+ \rightarrow \eta' K^+$ and $B_s^0 \rightarrow \eta' \phi$ selection efficiencies and their breakdown, for signal decays and expected physics backgrounds.

	$B^+ \rightarrow \eta' K^+$ selection	$B_s^0 \rightarrow \eta' \phi$ selection
2011 conditions:	$B^+ \rightarrow \eta' K^+$ signal	$B_s^0 \rightarrow \eta' \phi$ signal
ϵ^{geom}	$(17.54 \pm 0.06)\%$	$(17.80 \pm 0.04)\%$
$\epsilon^{\text{presel geom}}$	$(3.797 \pm 0.026)\%$	$(2.444 \pm 0.021)\%$
$\epsilon^{\text{PID partial\&geom}}$	$(85.916 \pm 0.002)\%$	$(84.735 \pm 0.005)\%$
$\epsilon^{\text{trig PID\&partial\&geom}}$	$(41.13 \pm 0.40)\%$	$(36.74 \pm 0.44)\%$
$\epsilon^{\text{BDT presel}}$	$(70.99 \pm 0.62)\%$	$(62.15 \pm 0.86)\%$
$\epsilon^{\text{CL+PID BDT\&presel}}$	$(91.53 \pm 0.45)\%$	$(94.24 \pm 0.51)\%$
$\epsilon^{\text{uniq CL+PID\&BDT\&presel}}$	$(98.22 \pm 0.22)\%$	$(98.60 \pm 0.27)\%$
$\epsilon^{\text{total}} = \text{product of above}$	$(0.1502 \pm 0.0024)\%$	$(0.0782 \pm 0.0016)\%$
2012 conditions:	$B^+ \rightarrow \eta' K^+$ signal	$B_s^0 \rightarrow \eta' \phi$ signal
ϵ^{geom}	$(17.89 \pm 0.05)\%$	$(18.16 \pm 0.05)\%$
$\epsilon^{\text{presel geom}}$	$(3.414 \pm 0.017)\%$	$(2.161 \pm 0.014)\%$
$\epsilon^{\text{PID partial\&geom}}$	$(85.622 \pm 0.001)\%$	$(84.945 \pm 0.002)\%$
$\epsilon^{\text{trig PID\&partial\&geom}}$	$(40.59 \pm 0.25)\%$	$(40.38 \pm 0.31)\%$
$\epsilon^{\text{BDT presel}}$	$(68.68 \pm 0.46)\%$	$(57.04 \pm 0.67)\%$
$\epsilon^{\text{CL+PID BDT\&presel}}$	$(89.67 \pm 0.36)\%$	$(93.36 \pm 0.43)\%$
$\epsilon^{\text{uniq CL+PID\&BDT\&presel}}$	$(97.55 \pm 0.19)\%$	$(99.16 \pm 0.16)\%$
$\epsilon^{\text{total}} = \text{product of above}$	$(0.1275 \pm 0.0015)\%$	$(0.0711 \pm 0.0012)\%$
2011+2012 average conditions:		$B_s^0 \rightarrow \phi\phi(\pi\pi\pi^0)$ background
ϵ^{geom}		$(18.15 \pm 0.03)\%$
$\epsilon^{\text{presel geom}}$		$(2.032 \pm 0.011)\%$
$\epsilon^{\text{PID partial\&geom}}$		$(85.387 \pm 0.008)\%$
$\epsilon^{\text{trig PID\&partial\&geom}}$		$(33.49 \pm 0.27)\%$
$\epsilon^{\text{BDT presel}}$		$(41.28 \pm 0.56)\%$
$\epsilon^{\text{CL+PID BDT\&presel}}$		$(91.94 \pm 0.48)\%$
$\epsilon^{\text{uniq CL+PID\&BDT\&presel}}$		$(97.995 \pm 0.258)\%$
$\epsilon^{\text{total}} = \text{product of above}$		$(0.0392 \pm 0.0007)\%$
2011+2012 average conditions:		$B^0 \rightarrow \phi K^*(892)^0$ background
ϵ^{geom}		$(18.74 \pm 0.05)\%$
$\epsilon^{\text{presel geom}}$		$(1.007 \pm 0.004)\%$
$\epsilon^{\text{PID partial\&geom}}$		$(31.710 \pm 0.006)\%$
$\epsilon^{\text{trig PID\&partial\&geom}}$		$(44.49 \pm 0.31)\%$
$\epsilon^{\text{BDT presel}}$		$(12.17 \pm 0.37)\%$
$\epsilon^{\text{CL+PID BDT\&presel}}$		$(63.92 \pm 1.54)\%$
$\epsilon^{\text{uniq CL+PID\&BDT\&presel}}$		$(98.06 \pm 0.55)\%$
$\epsilon^{\text{total}} = \text{product of above}$		$(0.00203 \pm 0.00008)\%$
2011+2012 average conditions:		$B^0 \rightarrow \phi K_1(1270)^0$ background
ϵ^{geom}		$(17.50 \pm 0.03)\%$
$\epsilon^{\text{presel geom}}$		$(0.707 \pm 0.005)\%$
$\epsilon^{\text{PID partial\&geom}}$		$(31.878 \pm 0.031)\%$
$\epsilon^{\text{trig PID\&partial\&geom}}$		$(36.99 \pm 0.54)\%$
$\epsilon^{\text{BDT presel}}$		$(25.86 \pm 0.95)\%$
$\epsilon^{\text{CL+PID BDT\&presel}}$		$(69.13 \pm 1.96)\%$
$\epsilon^{\text{uniq CL+PID\&BDT\&presel}}$		$(98.69 \pm 0.58)\%$
$\epsilon^{\text{total}} = \text{product of above}$		$(0.0026 \pm 0.0001)\%$

3.7.2 PID efficiencies

The simulation is known not to describe PID variables well and therefore a data-driven method is used to obtain the PID efficiencies. This is done using the `PidCalib` tool [76], which uses calibration samples of decays where particles can be identified from their kinematic properties. In the case of pions and kaons a calibration sample of real $D^{*+} \rightarrow D^0(K^- \pi^+) \pi^+$ decays is used. The phase space is divided in bins of several variables relevant for the PID performance. In this analysis, momentum and pseudo-rapidity are used. Using the calibration sample, the efficiency is derived in each two-dimensional bin. This information is then folded with the two-dimensional kinematic distributions of the reconstructed MC simulated decays of interest passing the preselection without any charged hadron identification or trigger requirements, in order to obtain the overall efficiency. This procedure is needed to take into account the possible differences in the kinematical distributions between the calibration sample and the simulated signal sample.

3.7.3 Trigger efficiencies

The trigger efficiency is factorized as

$$\epsilon^{\text{trig|PID\&presel\&geom}} = \epsilon^{\text{L0}} \times \epsilon^{\text{HLT1|L0}} \times \epsilon^{\text{HLT2|HLT1\&L0}}, \quad (3.4)$$

where the L0 trigger efficiency (on preselected decays of interest) is estimated as

$$\epsilon^{\text{L0}} = \epsilon^{\text{L0_TOS}} + \epsilon^{\text{L0_TIS}} - \epsilon^{\text{L0_TOS}} \times \epsilon^{\text{L0_TIS}} \quad (3.5)$$

from the efficiency of the `Hadron_TOS` line, $\epsilon^{\text{L0_TOS}}$, and the combined efficiency $\epsilon^{\text{L0_TIS}}$ of the different `L0_TIS` lines of Table 3.2. The quantity $\epsilon^{\text{HLT1|L0}}$ ($\epsilon^{\text{HLT2|HLT1\&L0}}$) is the HLT1 (HLT2) efficiency on preselected decays of interest passing L0 (L0 and HLT1). All trigger efficiencies are obtained from MC samples of the decays of interest, except $\epsilon^{\text{L0_TOS}}$ which is determined with real data. The L0 hadron efficiency has been measured and tabulated using well identified kaons and pions from real $D^{*+} \rightarrow D^0(K^- \pi^+) \pi^+$ decays as a function of track type, track E_T and magnet polarity [77]; these calibrated efficiency tables are then folded with the MC simulated distributions of tracks from the decay of interest to obtain $\epsilon^{\text{L0_TOS}}$. The efficiencies for the $B^+ \rightarrow \eta' K^+$ and $B_s^0 \rightarrow \eta' \phi$ modes, presented in Table 3.8, are very similar to each other as intended with the choice of the control channel and expected from the very close requirements. The use of the `Topo4BodyBBBDT` line, which is TOS only for the signal channel can introduce a small bias that does not cancel out in the ratio. However, the $B_s^0 \rightarrow \eta' \phi$ signal is TOS exclusively for the `Topo4BodyBBBDT` only in 2% of the cases, while it is mainly triggered by the 2- and 3-body lines, like $B^+ \rightarrow \eta' K^+$.

Table 3.8 – $B^+ \rightarrow \eta' K^+$ and $B_s^0 \rightarrow \eta' \phi$ trigger efficiencies and their breakdown, computed on preselected signal MC events.

	$B^+ \rightarrow \eta' K^+$ preselection	$B_s^0 \rightarrow \eta' \phi$ preselection
2011 conditions:	$B^+ \rightarrow \eta' K^+$ signal	$B_s^0 \rightarrow \eta' \phi$ signal
$\epsilon^{\text{L0_TOS}}$	$(36.56 \pm 0.52)\%$	$(28.29 \pm 0.40)\%$
$\epsilon^{\text{L0_TIS}}$	$(32.12 \pm 0.36)\%$	$(30.69 \pm 0.44)\%$
ϵ^{L0}	$(56.94 \pm 0.42)\%$	$(50.30 \pm 0.42)\%$
$\epsilon^{\text{HLT1 L0}}$	$(84.74 \pm 0.36)\%$	$(84.40 \pm 0.50)\%$
$\epsilon^{\text{HLT2 HLT1\&L0}}$	$(85.24 \pm 0.39)\%$	$(86.55 \pm 0.52)\%$
$\epsilon^{\text{L0}} \times \epsilon^{\text{HLT1 L0}} \times \epsilon^{\text{HLT2 HLT1\&L0}}$	$(41.13 \pm 0.40)\%$	$(36.74 \pm 0.44)\%$
2012 conditions:	$B^+ \rightarrow \eta' K^+$ signal	$B_s^0 \rightarrow \eta' \phi$ signal
$\epsilon^{\text{L0_TOS}}$	$(33.80 \pm 0.24)\%$	$(26.45 \pm 0.17)\%$
$\epsilon^{\text{L0_TIS}}$	$(30.64 \pm 0.26)\%$	$(32.43 \pm 0.34)\%$
ϵ^{L0}	$(54.08 \pm 0.24)\%$	$(50.30 \pm 0.28)\%$
$\epsilon^{\text{HLT1 L0}}$	$(84.13 \pm 0.28)\%$	$(88.34 \pm 0.35)\%$
$\epsilon^{\text{HLT2 HLT1\&L0}}$	$(89.20 \pm 0.26)\%$	$(90.87 \pm 0.33)\%$
$\epsilon^{\text{L0}} \times \epsilon^{\text{HLT1 L0}} \times \epsilon^{\text{HLT2 HLT1\&L0}}$	$(40.59 \pm 0.25)\%$	$(40.38 \pm 0.31)\%$

3.7.4 Data-MC discrepancies

In addition to the PID and trigger efficiencies, other data-MC comparisons have been performed, in order to reduce the probability of a wrong estimate of the efficiencies.

Modeling of the $\pi^+ \pi^-$ mass distribution

As discussed in Sec. 3.2 the MC samples used in the analysis are generated considering only the η' decaying into a photon and a ρ^0 resonant state of the pion pair. Figure 3.14 compares the $\pi^+ \pi^-$ mass distribution obtained in MC simulation and data using the sPlot technique [73] applied to the $B^+ \rightarrow \eta' K^+$ mass distribution. A significant difference is observed, which is due not only to the missing phase-space contribution for the pion pair but more generally to the imperfect modeling of the $\pi^+ \pi^-$ mass distribution. Indeed the invariant mass distribution of the $\pi^+ \pi^-$ system in the η' decay has a non trivial shape. In particular the $\eta' \rightarrow \pi^+ \pi^- \gamma$ decay amplitude presents, besides the main component with the ρ^0 resonant final state, an extra-contribution predicted by QCD [78] and called box-anomaly, which shift the mass spectrum peak from the nominal ρ^0 mass ($770 \text{ MeV}/c^2$) to lower values and modifies the upper tail of the distribution [79]. However, this discrepancy is small and its effect on the efficiencies cancels out in the branching fraction ratio computation since both signal and normalisation modes are affected in the same way. Therefore no correction is applied. A systematic uncertainty is also neglected, being small with respect to the other sources accounted for.

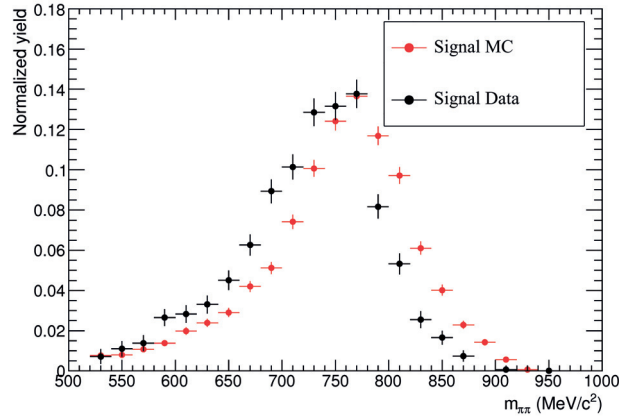


Figure 3.14 – Normalised $\pi^+ \pi^-$ mass distributions for the $B^+ \rightarrow \eta' K^+$ control channel. The black (red) points with error bars are obtained using the sPlot technique for signal data (MC).

SPD hit multiplicity

The simulation of the SPD charged track multiplicity distribution shows discrepancies with data, as seen in Fig. 3.15. This affects the efficiency of the global cut applied in the L0 trigger on the number of SPD hits. No correction is applied but a systematics uncertainty accounts for this discrepancy, as described in Sec. 3.8.

Photon efficiency correction

The photon reconstruction efficiency is not perfectly modeled in the simulation and an efficiency correction is determined in each bin of the photon transverse energy E_T as described in Ref. [80]. This study can be used to derive average corrections for this analysis, based on the photon E_T distribution in $B^+ \rightarrow \eta' K^+$ and $B_s^0 \rightarrow \eta' \phi$ simulated decays. These average corrections are similar (within the uncertainties) for the two decays because the E_T distributions are compatible. In the final calculation of the branching fraction ratio a correction on the efficiency ratio will be applied. The correction factor is found to be 0.9980 ± 0.0014 .

Tracking efficiency correction

The tracking efficiency is not perfectly modeled in the simulation and therefore an efficiency correction needs to be applied. In order to evaluate this correction the method suggested in Ref. [81] is used. The tracking efficiency is corrected according to tables giving the data-MC efficiency ratio in bins of pseudo-rapidity and momentum. The correction on the ratio of efficiencies for $B^+ \rightarrow \eta' K^+$ and $B_s^0 \rightarrow \eta' \phi$ is found to be 0.997 ± 0.004 , where the quoted uncertainty is the sum in quadrature of the statistical and systematic uncertainties. The latter is equal to 0.4% to account for the additional track in $B_s^0 \rightarrow \eta' \phi$.

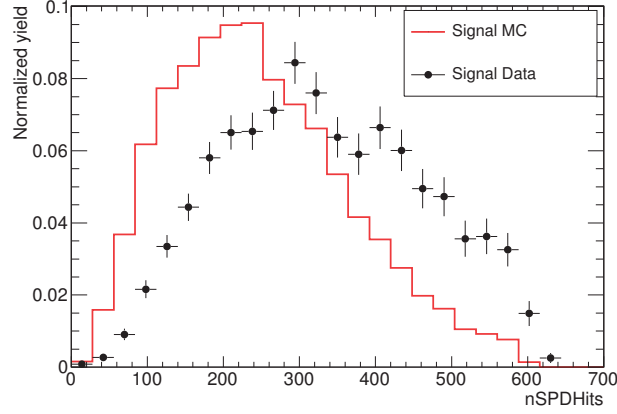


Figure 3.15 – Normalised distributions of the number of SPD hits for the $B^+ \rightarrow \eta' K^+$ control channel. The black (red) points with error bars are obtained using the sPlot technique for signal data (MC).

3.8 Efficiency ratio and systematic uncertainties

The efficiency values obtained for the signal and normalisation channels, together with the tracking and photon efficiency corrections described in the previous section, are used in the computation of the final efficiency ratio, defined as

$$\frac{\varepsilon^{\text{total}}(B^+ \rightarrow \eta' K^+)}{\varepsilon^{\text{total}}(B_s^0 \rightarrow \eta' \phi)} \quad (3.6)$$

The ratio is computed as a weighted average according to integrated luminosities and production cross-sections for the 2011 and 2012 running conditions. The $B_s^0 \rightarrow \eta' \phi$ and the $B^+ \rightarrow \eta' K^+$ decays being similar in topology and kinematic, most of the systematic uncertainties cancel out in the evaluation of the efficiency ratio. However, non-cancelling sources of uncertainties on the efficiencies must be evaluated. These sources are listed in Table 3.9 and described in more details below.

PID efficiency The systematic uncertainties on the PID efficiency arise from the data calibration sample, limited size of the reference sample of simulated signal events, and the different kinematics of the two channels. Systematic uncertainties due to the size of the calibration samples are negligible with respect to the uncertainty introduced by the calibration method. In order to account for these effects, we test if the binning scheme significantly changes the efficiency. We vary the nominal binning scheme used in the efficiency calculation, and the efficiency ratio is recomputed. The systematic uncertainty on the PID efficiency is taken as largest difference with the nominal value of the ratio, and is found to be ± 0.021 .

Chapter 3. $B_s^0 \rightarrow \eta' \phi$ and $B^+ \rightarrow \eta' K^+$ selection

Table 3.9 – Absolute systematic uncertainties on the ratio of the $B^+ \rightarrow \eta' K^+$ and $B_s^0 \rightarrow \eta' \phi$ efficiencies.

Source	Systematic uncertainty
PID selection	0.021
Trigger	0.042
BDT selection	0.045
Photon reconstruction efficiency	0.003
SPD cut efficiency	0.016
Tracking efficiency correction	0.007
Hadron interaction	0.026
MC statistics	0.030
Quadratic sum	0.078

L0 trigger efficiency In order to evaluate the systematic uncertainty introduced in the computation of the L0Hadron_TOS efficiency, we study the effect of the kinematic cut applied by the L0Hadron_TOS trigger line ($E_T > 3620$ MeV in 2012 and $E_T > 3500$ MeV in 2011) on the efficiency ratio. A 5% variation of the value of this cut produces a variation of the efficiency ratio of ± 0.042 , which is applied as systematic uncertainty.

BDT efficiency In order to account for the systematic uncertainty introduced by the BDT selection of the $B^+ \rightarrow \eta' K^+$ channel, the absolute difference in efficiency between data and MC for the nominal cut (5.3% for 2012 and 2.2% for 2011) is considered. The same uncertainty is used for $B_s^0 \rightarrow \eta' \phi$, and a correlation of 80% with $B^+ \rightarrow \eta' K^+$ is assumed. This high correlation coefficient is motivated by the almost identical dependence of the BDT output with the input variables for the two channels. A test is performed to evaluate the effects of the different BDTs and of the different spectra of the BDT input variables for the $B_s^0 \rightarrow \eta' \phi$ and $B^+ \rightarrow \eta' K^+$ channels. We apply both BDT algorithms (the one for $B^+ \rightarrow \eta' K^+$ and the one for $B_s^0 \rightarrow \eta' \phi$) to the same sample and then plot the two BDT outputs event-by-event. Figure 3.16 shows the distributions of the two BDT output for $B^+ \rightarrow \eta' K^+$ and $B_s^0 \rightarrow \eta' \phi$ MC events. The measured correlations are of $\sim 90\%$ in the case of $B^+ \rightarrow \eta' K^+$ and 87% in the case of $B_s^0 \rightarrow \eta' \phi$. This test can be interpreted as a measure of the correlation between the two BDT functions, but it does not evaluate the effect due to the different distributions of the BDT input variables between the two channels. In order to test the latter effect, we cut on the BDT input variables of the $B^+ \rightarrow \eta' K^+$ signal MC to centre the distributions on the $B_s^0 \rightarrow \eta' \phi$ phase space and then recalculate the correlation between the two BDT outputs. Depending on the applied cuts, this correlation varies monotonically from $\sim 90\%$ (without any cut applied, 9200 candidates selected) down to $\sim 80\%$ (with the tightest cuts and 417 candidates selected). We conclude that the correlation is between 80% and 90%, and we use the value of 80%, towards which the above procedure converges. The resulting uncertainty on the BDT efficiency ratio, ± 0.045 , is used as systematic uncertainty.

3.8. Efficiency ratio and systematic uncertainties

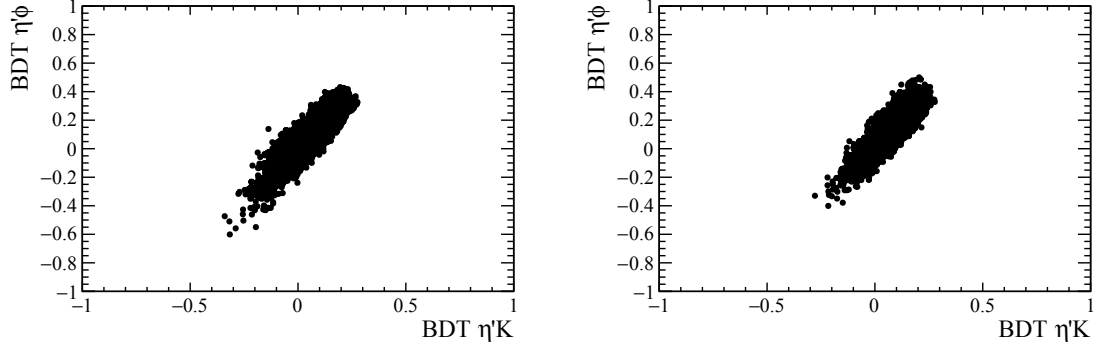


Figure 3.16 – Two-dimensional distribution of the $B_s^0 \rightarrow \eta' \phi$ and $B^+ \rightarrow \eta' K^+$ BDT output values for $B^+ \rightarrow \eta' K^+$ (left) and $B_s^0 \rightarrow \eta' \phi$ (right) MC events.

Photon efficiency correction As described in Sec. 3.7.4, a correction factor is applied to the efficiency ratio to take into account the imperfect model for the photon reconstruction efficiency. The uncertainty on this correction factor, ± 0.003 , is taken as systematic uncertainty.

SPD cut efficiency In the efficiency calculation we do not correct for the data-MC mis-match of the SPD multiplicity distribution, assuming that this effect is the same for the signal and normalisation channels. We consider a systematic uncertainty on this assumption. Because of the data-MC discrepancy, the cut applied by the L0 trigger lines on the SPD multiplicity (< 600) rejects a smaller fraction of events in the simulation than in real data. An “effective” cut at 430 on the SPD multiplicity is used to evaluate the efficiency for the signal and normalisation channel. This cut is chosen to reproduce, in the MC, an efficiency close to that obtained in data, and it is estimated using the $B^+ \rightarrow \phi K^+$ decay as proxy[82]. Using this requirement on the SPD multiplicity we estimate the fraction of rejected events in the $B_s^0 \rightarrow \phi \eta'$ and $B^+ \rightarrow \eta' K^+$ MC samples. The results are listed in Table 3.10: The resulting SPD efficiency ratio, weighted

Table 3.10 – Fraction of rejected MC events using a cut at 430 on the SPD multiplicity.

Decay	Rejected fraction	
	2011	2012
$B_s^0 \rightarrow \phi \eta'$	$(2.24 \pm 0.34)\%$	$(5.47 \pm 0.41)\%$
$B^+ \rightarrow \eta' K^+$	$(2.45 \pm 0.27)\%$	$(7.6 \pm 0.34)\%$

by luminosity and cross section, is 0.984 ± 0.004 . We use the difference with respect to unity (± 0.016) as systematic uncertainty.

Tracking efficiency correction We correct the tracking efficiency as described in Sec. 3.7.4, and apply the uncertainty on the correction as systematic uncertainty (± 0.007). Since the

correction to the tracking efficiency is obtained using muons, an additional uncertainty of ± 0.026 is needed to account for hadronic interactions in the detector material [52].

MC statistics We assign an uncertainty to account for the limited statistics of the MC simulated data samples (± 0.030).

Including all the systematic uncertainties described above, the final efficiency ratio is found to be

$$\frac{\varepsilon^{\text{total}}(B^+ \rightarrow \eta' K^+)}{\varepsilon^{\text{total}}(B_s^0 \rightarrow \eta' \phi)} = 1.828 \pm 0.078. \quad (3.7)$$

This number will enter in Eq. 4.12 to calculate the final value of the branching fraction.

3.9 Expected yields

The determination of the selection efficiencies for the signal and background modes allows the computation of the yields expected in the Run 1 data set. Given a decay mode the expected number of events to be observed is computed as the product of the integrated luminosity L , the $b\bar{b}$ production cross-section $\sigma(pp \rightarrow b\bar{b}X)$, twice the fragmentation fraction $f_{u,d,s}$, the visible branching fraction $\mathcal{B}(B_{u,d,s} \rightarrow X)$ and the selection efficiency $\varepsilon^{\text{total}}(B_{u,d,s} \rightarrow X)$:

$$N(B_{u,d,s} \rightarrow X) = \mathcal{B}(B_{u,d,s} \rightarrow X) \times L \times \sigma(pp \rightarrow b\bar{b}X) \times 2 \times f_{u,d,s} \times \varepsilon^{\text{total}}(B_{u,d,s} \rightarrow X). \quad (3.8)$$

Due to the large uncertainty on the luminosity and $b\bar{b}$ production cross-section, and the data-MC discrepancies, the expected yields are calculated with respect to the yield measured in data for the control channel $B^+ \rightarrow \eta' K^+$. For the $B_s^0 \rightarrow \phi \eta'$ decay the expected number of selected events is given by the following formula

$$N_{B_s^0 \rightarrow \eta' \phi} = N_{B^+ \rightarrow \eta' K^+} \times \frac{f_s}{f_u} \times \frac{\mathcal{B}(B_s^0 \rightarrow \eta' \phi)}{\mathcal{B}(B^+ \rightarrow \eta' K^+)} \times \mathcal{B}(\phi \rightarrow K^+ K^-) \times \frac{\varepsilon_{B_s^0 \rightarrow \eta' \phi}^{\text{total}}}{\varepsilon_{B^+ \rightarrow \eta' K^+}^{\text{total}}}, \quad (3.9)$$

where $N_{B^+ \rightarrow \eta' K^+}$ is the fitted yield for the $B^+ \rightarrow \eta' K^+$ mode, $f_s/f_u = f_s/f_d = 0.259 \pm 0.015$ [83] is the B^+ / B_s^0 production ratio in LHCb, $\mathcal{B}(B_s^0 \rightarrow \eta' \phi) / \mathcal{B}(B^+ \rightarrow \eta' K^+)$ is the ratio of branching fraction and $\varepsilon_{B_s^0 \rightarrow \eta' \phi}^{\text{total}} / \varepsilon_{B^+ \rightarrow \eta' K^+}^{\text{total}}$ is the efficiency ratio (see Eq. 3.7).

The obtained value, assuming a branching fraction of 4×10^{-6} , is 40 ± 3 events. The expected yields for the contamination modes, together with the expected signal yields are presented in Table 3.11. Within 2σ from the B_s^0 and η' nominal masses [13], where σ is the mass resolution ($\sim 20 \text{ MeV}/c^2$ for B_s^0 and $\sim 13 \text{ MeV}/c^2$ for η'), their contribution is negligible. However, the shape of the $B_s^0 \rightarrow \phi \phi$ distribution in data (discussed in the next chapter) suggests the necessity to introduce this component in the final fit model.

3.9. Expected yields

Table 3.11 – Expected number of Run 1 signal and the main physics backgrounds events passing the selection requirements, in the full B_s^0 and η' mass regions and in the signal region.

Decay mode	Visible branching fraction	Full region	Signal region
$B_s^0 \rightarrow \eta' \phi$	4×10^{-6}	40	
$B_s^0 \rightarrow \phi \phi$	$2 \times 1.92 \times 10^{-5} \times 0.492 \times 0.153$	104	7
$B^0 \rightarrow \phi K^*(892)^0$	$1 \times 10^{-5} \times 0.492 \times 0.66$	24	2
$B^0 \rightarrow \phi K_1(1270)$	$1 \times 10^{-5} \times 0.492 \times 0.86$	39	1

4 $B_s^0 \rightarrow \eta' \phi$ signal extraction and results

The branching fraction of the decay $B_s^0 \rightarrow \eta' \phi$ is measured with respect to the normalisation channel $B^+ \rightarrow \eta' K^+$. Indeed, in LHCb, it is practical to compute the branching fractions with respect to a well known control channel. This procedure has the main advantage of removing most of the systematic effects if the selection of the normalisation channel is kept as similar as possible to that of the signal. Moreover, in the ratio, factors with large uncertainty such as the luminosity or the $b\bar{b}$ production cross-section (see Eq. 3.8 in Sec. 3.9) cancel out and do not need to be taken into account.

The extraction of the $B^+ \rightarrow \eta' K^+$ and $B_s^0 \rightarrow \eta' \phi$ yields, needed for the computation of the branching fraction ratio, is obtained from a simultaneous extended maximum likelihood fit to the selected samples of data candidates. In this chapter, after an introductory explanation of the fit method, the fit model and its validation using real data and pseudo-experiments are described and finally the fit results are presented.

4.1 Maximum likelihood method

The maximum likelihood method is used to estimate the parameters of a statistical model, given a set of observations, by finding the parameter values that maximise a likelihood function. For this analysis the parameters of interest are the signal yields. Given a vector \mathbf{m} of k observables, being here the masses of the B and η' candidates, a vector $\boldsymbol{\theta}$ of model parameters, and a set of N observations, the extended likelihood function is written as

$$\mathcal{L} = \exp(-\sum_j N_j) \prod_{i=1}^N \left(\sum_j N_j P_j(\mathbf{m}^i; \boldsymbol{\theta}) \right), \quad (4.1)$$

where N_j represents the yield of component j and $P_j(\mathbf{m}; \boldsymbol{\theta})$ the probability density function for the component j , which, assuming no correlation among the observables, is written as the product

$$P_j(\mathbf{m}; \boldsymbol{\theta}) = P_j^1(m_1; \boldsymbol{\theta}) \times \dots \times P_j^k(m_k; \boldsymbol{\theta}). \quad (4.2)$$

The estimator values $\hat{\theta}_i$ and \hat{N}_j are obtained by maximizing the likelihood function with respect to θ_i and N_j :

$$\frac{\partial \mathcal{L}}{\partial \theta_i} = 0 \quad \text{and} \quad \frac{\partial \mathcal{L}}{\partial N_j} = 0. \quad (4.3)$$

4.2 Fit model description

The $B_s^0 \rightarrow \eta' \phi$ and $B^+ \rightarrow \eta' K^+$ yields are extracted through a simultaneous extended maximum likelihood fit of the $B_s^0 \rightarrow \eta' \phi$ and $B^+ \rightarrow \eta' K^+$ candidates. A common fit model is used for the 2011 and 2012 data samples, despite the different running conditions, in order to reduce the fit instability due to the small $B_s^0 \rightarrow \eta' \phi$ sample size, especially in the high-mass sideband. The fit is performed in two dimensions for both $B_s^0 \rightarrow \eta' \phi$ and $B^+ \rightarrow \eta' K^+$ candidates, and the fitted observables are the $\eta' K^+ K^-$ ($\eta' K^+$) and $\pi^+ \pi^- \gamma$ invariant masses. The $\pi^+ \pi^- \gamma$ mass is constrained to the known η' mass [13] in the calculation of the $\eta' K^+ K^-$ ($\eta' K^+$) mass, in order to improve the resolution and reduce the correlation between the two fitted masses. The possibility to include as third dimension the $K^+ K^-$ invariant mass for the $B_s^0 \rightarrow \eta' \phi$ sample has not been pursued. Indeed most of the background in the selected $B_s^0 \rightarrow \eta' \phi$ sample contains real ϕ mesons and a third dimension would have increased the complexity of the fit without helping in terms of signal discrimination.

The fit model is developed and validated in an iterative process on simulated and real data. The fit is performed using the ROOFIT library [84].

The signal and background components are described using several probability density functions (PDFs). In total, seven components are used in the nominal model: three for the $B^+ \rightarrow \eta' K^+$ sample, describing the signal, the combinatorial background with true η' and the combinatorial background without true η' (pure combinatorial background), and four components for the $B_s^0 \rightarrow \eta' \phi$ sample to model the signal, the combinatorial background with true η' , the pure combinatorial background and the $B_s^0 \rightarrow \phi \phi (\pi^+ \pi^- \pi^0)$ physics background. Table 4.1 summarizes the components and the PDFs used to describe them. These PDFs are the following:

1. A double-tail Crystal Ball function (CB) is used to describe the B^+ , B_s^0 and η' signal peaks. It consists of a Gaussian core with two power-law tails. The tails account for poorly reconstructed signal events or possible radiative corrections. This function is used to describe the reconstructed mass distribution of particles for which the detector resolution effects dominate over the particle natural width. The generic double-tail CB function for variable m is

$$\text{CB}(m; m_0, \sigma, \alpha_L, n_L, \alpha_R, n_R) = N_{\text{CB}} \begin{cases} A_L \left(B_L - \frac{m-m_0}{\sigma} \right)^{-n_L} & \text{for } \frac{m-m_0}{\sigma} \leq -\alpha_L, \\ \exp\left(-\frac{(m-m_0)^2}{2\sigma^2}\right) & \text{for } -\alpha_L < \frac{m-m_0}{\sigma} < \alpha_R, \\ A_R \left(B_R + \frac{m-m_0}{\sigma} \right)^{-n_R} & \text{for } \frac{m-m_0}{\sigma} \geq \alpha_R, \end{cases} \quad (4.4)$$

Table 4.1 – Description of the components of the simultaneous two-dimensional fit of the $B_s^0 \rightarrow \eta' \phi$ and $B^+ \rightarrow \eta' K^+$ samples. The CB, LIN and QUAD functions are defined in Eqs. 4.4, 4.7 and 4.9, respectively.

Component of the $B^+ \rightarrow \eta' K^+$ sample	PDF($m_{\eta' K}$)	PDF($m_{\pi\pi\gamma}$)
$B^+ \rightarrow \eta' K^+$ signal	CB	CB
Combinatorial bkg with true η'	LIN	CB
Combinatorial bkg without true η'	QUAD	LIN
Component of the $B_s^0 \rightarrow \eta' \phi$ sample	PDF($m_{\eta' \phi}$)	PDF($m_{\pi\pi\gamma}$)
$B_s^0 \rightarrow \eta' \phi$ signal	CB	CB
Combinatorial bkg with true η'	LIN	CB
Combinatorial bkg without true η'	LIN	LIN
$B_s^0 \rightarrow \phi \phi (\pi^+ \pi^- \pi^0)$	RooNDKeysPdf	

with

$$A_i = \left(\frac{n_i}{\alpha_i} \right)^{n_i} \exp \left(-\frac{\alpha_i^2}{2} \right), \quad (4.5)$$

$$B_i = \frac{n_i}{\alpha_i} - \alpha_i, \quad (4.6)$$

where the six parameters (all positive) are the mass of the decaying particle m_0 , the mass resolution σ , and the tail parameters: α_L, n_L (for the low-mass tail) and α_R, n_R (for the high-mass tail). N_{CB} is a normalisation factor which depends on the resolution and on the tail parameters.

2. The combinatorial background with true η' , peaking in the $m_{\pi\pi\gamma}$ distribution, is modeled in the $\eta' K^+ K^-$ (or $\eta' K^+$) dimension using a linear function. The same function is used for both mass observables (for $m_{\pi\pi\gamma}$ only) to describe the pure combinatorial in the $B_s^0 \rightarrow \eta' \phi$ ($B^+ \rightarrow \eta' K^+$) sample. The linear function is expressed as a first-order Chebychev polynomial,

$$\text{LIN}(m; a) = \frac{1}{2}(1 + ax), \quad (4.7)$$

where

$$x = 2 \frac{m - m_{\min}}{m_{\max} - m_{\min}} - 1, \quad (4.8)$$

a is a slope parameter free in the fit, m_{\min} and m_{\max} are the lower and upper edges of the fitting range in m , and m is the mass of the $\eta' K^+ K^-$, $\eta' K^+$ or $\pi^+ \pi^- \gamma$ system.

3. A quadratic function is used to describe the pure combinatorial background component

in the $\eta' K^+$ mass distribution. A second-order Chebychev polynomial is used,

$$\text{QUAD}(m; a, b) = \frac{3}{2(3-b)} (1 + ax + b(2x^2 - 1)), \quad (4.9)$$

where x is defined as in Eq. 4.8. The parameters a and b are free in the fit.

4. The $B_s^0 \rightarrow \phi\phi(\pi^+\pi^-\pi^0)$ background component is modeled using `RoosNDKeysPdf` [85]. This PDF models the distribution of an input dataset, consisting of N MC events, using a superposition of Gaussian kernels, one for each data point, each contributing $1/N$ to the total integral of the PDF. The width of the Gaussian is adaptively calculated from the local density of events (narrow for regions with high event density to account better for details and wide for regions with small density to promote smoothness).

Several assumptions are made on the fit components:

- The two mass observables are treated as independent for all components except for the one describing the $B_s^0 \rightarrow \phi\phi(\pi^+\pi^-\pi^0)$ background. In this case, a two-dimensional PDF is used to take correlations between the two fitted mass observables into account, as described in Sec. 4.3.3. This assumption is tested on MC and real data samples.
- The tail parameters of the B_s^0 and B^+ components are fixed to the values obtained from the two-dimensional fit of the 2011 and 2012 MC samples, performed separately for the $B^+ \rightarrow \eta' K^+$ and $B_s^0 \rightarrow \eta' \phi$ candidates.
- Constraints are applied to the parameters describing the B_s^0 mass and resolution. In particular the difference $m_{B_s^0} - m_{B^+}$ is fixed to the PDG value, $87.33 \pm 0.23 \text{ MeV}/c^2$, and the ratio $\sigma_{B_s^0}/\sigma_{B^+}$ is fixed to the central value obtained from a fit on the simulated samples, $\sigma_{B_s^0}/\sigma_{B^+} = 0.93 \pm 0.02$.
- The η' mass $m_{\eta'}$ and the resolution $\sigma_{\eta'}$ are left free to vary in the fit, while the tail parameters are fixed to the values obtained by the final two-dimensional simultaneous fit of 2011 and 2012 $B^+ \rightarrow \eta' K^+$ and $B_s^0 \rightarrow \eta' \phi$ MC samples (see Table 4.2). All the parameters describing the η' signal are shared between the two channels and the two run conditions.
- The parameters describing the slopes of the first- and second-order Chebychev polynomial are free to vary.
- In the case of the $B_s^0 \rightarrow \eta' \phi$ sample, the same slope parameter is used to describe the combinatorial background with and without a true η' resonance in the $\eta' K^+ K^-$ mass dimension, because of the low sensitivity due to the small number of events.

The fit counts 17 free parameters in total: seven parameters for the yields, four parameters for the masses and resolutions of the B and the η' mesons, and six parameters for the various combinatorial components.

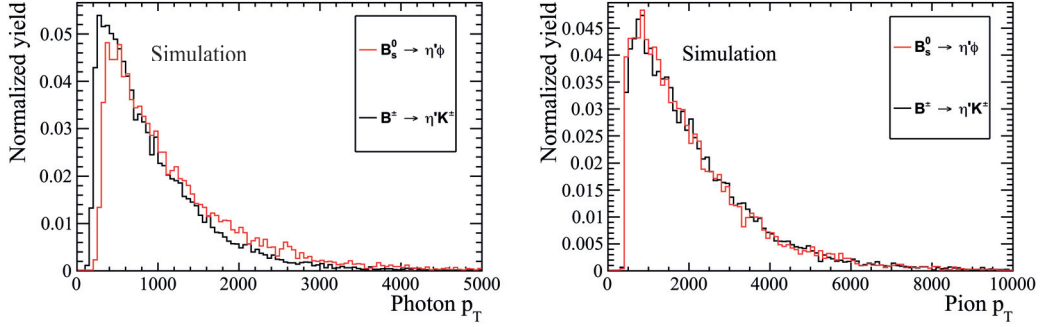


Figure 4.1 – Distribution of the transverse momentum of the photon (left) and pions (right) in 2012 MC datasets for $B^+ \rightarrow \eta' K^+$ (black) and $B_s^0 \rightarrow \eta' \phi$ (red).

4.3 Fit model validation

The fit model is studied and validated on fully-simulated MC samples, real data and fast simulation samples. These studies are described in the following sections.

4.3.1 Studies with fully simulated events

The signal models are determined and then validated with several fits on samples of simulated events selected with the criteria described in Chapter 3. In a first step, in order to extract the B^+ and B_s^0 signal shapes and the values of the tail parameters, the $B_s^0 \rightarrow \eta' \phi$ and $B^+ \rightarrow \eta' K^+$ candidates are fitted separately using a two-dimensional fit for the 2011 and 2012 datasets. The fit of the 2011 and 2012 samples is performed simultaneously, and with independent parameters for each of the two running conditions, in order to validate the assumption that the two samples are compatible and therefore can be merged in the final nominal fit.

In a second step the $B_s^0 \rightarrow \eta' \phi$ and $B^+ \rightarrow \eta' K^+$ MC samples are fitted simultaneously. The parameters describing the tails of B^+ and B_s^0 signal are fixed from the previous fit, while the parameters describing the shape of the η' signal are shared between the $B_s^0 \rightarrow \eta' \phi$ and $B^+ \rightarrow \eta' K^+$ datasets and are all free to vary. No difference is expected for the resolution and the mass of the η' in the two different channels, because the pions and photon momentum spectra (Fig. 4.1) are similar. In addition to CB functions used to model the signals, a linear component is included in the model to describe the small background originating for mis-reconstructed signal events. The values of the tail parameters for the η' shape, resulting from this fit, are then fixed and used for the fit to the real data.

The parameters to describe the tails of the B^+ , B_s^0 and η' mass peaks are shared between 2011 and 2012 data, since they have been checked to be compatible in the fit with independent parameters for each dataset. On the other hand, the parameters describing central mass values and resolutions are kept separate for the 2011 and 2012 datasets, such that their compatibility can be checked. The results obtained by the fit are shown in Table 4.2 and Fig. 4.2.

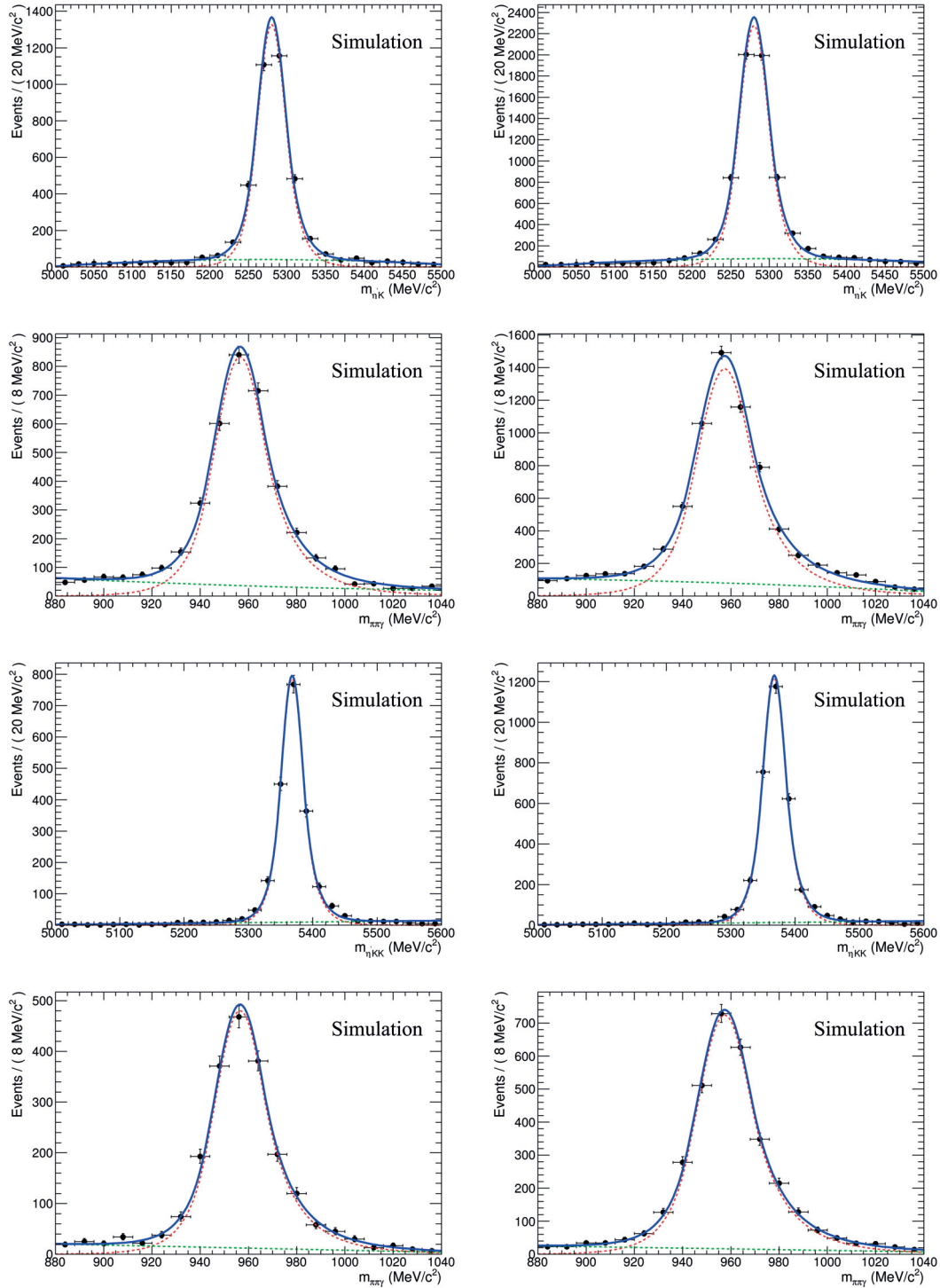


Figure 4.2 – From top to bottom, distributions of the $\eta' K^+$ and $\pi^+ \pi^- \gamma$ masses in $B^+ \rightarrow \eta' K^+$ MC samples, and of the $\eta' K^+ K^-$ and $\pi^+ \pi^- \gamma$ masses in $B_s^0 \rightarrow \eta' \phi$ MC samples, for the 2011 (left) and 2012 (right) conditions. The solid blue curves represent the result of the simultaneous two-dimensional fit described in the text, with the following components: $B^+ \rightarrow \eta' K^+$ and $B_s^0 \rightarrow \eta' \phi$ signal (red dashed), combinatorial background (green dashed).

Table 4.2 – Simultaneous fit of the $B^+ \rightarrow \eta' K^+$ and $B_s^0 \rightarrow \eta' \phi$ candidates in 2011 and 2012 signal MC samples with different masses and resolutions parameters for the 2011 and 2012 datasets.

Parameter		Value and error	
		2011	2012
B_s^0 mass	m_{B_s} [MeV/ c^2]	5368.0 ± 0.5	5367.6 ± 0.4
B^+ mass	m_B [MeV/ c^2]	5280.1 ± 0.4	5279.9 ± 0.3
η' mass	$m_{\eta'}$ [MeV/ c^2]	956.5 ± 0.2	957.4 ± 0.2
B_s^0 mass resolution	σ_{B_s} [MeV/ c^2]	17.1 ± 0.4	17.9 ± 0.3
B^+ mass resolution	σ_B [MeV/ c^2]	18.4 ± 0.3	19.2 ± 0.3
η' mass resolution	$\sigma_{\eta'}$ [MeV/ c^2]	10.7 ± 0.3	11.5 ± 0.3
B_s^0 mass left tail parameter	α_L	1.20	(fixed)
B_s^0 mass left tail parameter	n_L	33.97	(fixed)
B_s^0 mass right tail parameter	α_R	1.09	(fixed)
B_s^0 mass right tail parameter	n_R	17.14	(fixed)
B^+ mass left tail parameter	α_L	1.37	(fixed)
B^+ mass left tail parameter	n_L	57	(fixed)
B^+ mass right tail parameter	α_R	1.20	(fixed)
B^+ mass right tail parameter	n_R	100	(fixed)
η' mass left tail parameter	α_L	1.33 ± 0.09	
η' mass left tail parameter	n_L	12.3 ± 6.2	
η' mass right tail parameter	α_R	0.94 ± 0.05	
η' mass right tail parameter	n_R	7.7 ± 1.9	
$B_s^0 \rightarrow \eta' \phi$ signal yield		1901.1 ± 44.9	3079.0 ± 57.1
$B_s^0 \rightarrow \eta' \phi$ comb. background yield		241.9 ± 18.9	326.0 ± 22.5
$B^+ \rightarrow \eta' K^+$ signal yield		3295.2 ± 60.9	5923.7 ± 83.5
$B^+ \rightarrow \eta' K^+$ comb. background yield		749.8 ± 34	1503.3 ± 50.5

4.3.2 Validation with data

The fit model is further validated using real data. In particular, all the functions used for the signal and background description of the $B^+ \rightarrow \eta' K^+$ sample are tested. The background components and shapes are also evaluated by performing one-dimensional fits of the $\eta' K^+ K^-$ and $\pi^+ \pi^- \gamma$ sidebands of the $B_s^0 \rightarrow \eta' \phi$ data sample.

Study of the $B^+ \rightarrow \eta' K^+$ data samples

As described in the introduction of this chapter, the nominal fit is a two-dimensional fit to a merged sample of 2011 and 2012 data. However, a fit of the $B^+ \rightarrow \eta' K^+$ candidates is performed simultaneously for the 2011 and 2012 data in order to verify the hypotheses about the background components, the functional form of the combinatorial background and the compatibility between the η' mass and resolution parameters between 2011 and 2012 data and with MC simulation.

Chapter 4. $B_s^0 \rightarrow \eta' \phi$ signal extraction and results

All parameters are free to vary and kept separate for the 2011 and 2012 samples, except for the tail parameters of the CB functions, which are fixed to the values obtained from the fit on the fully simulated events. The slope parameter for the component describing the combinatorial background with true η' is shared between the 2011 and 2012 samples.

The results obtained by the fit are shown in Fig. 4.3 (mass distributions in the full fit region) and in Fig. 4.4 (mass distributions in the enhanced signal region). As shown in Table 4.3, 7886 ± 108 and 3203 ± 67 signal events are fitted in data, for 2012 and 2011, respectively. The resolutions and central mass values, obtained for both B^+ and η' , are larger than in the MC simulation (Table 4.2) and a small difference is seen between 2011 and 2012.

Since the two samples will be merged in the final fit, several studies with pseudo-experiments are performed (as presented in Sec. 4.3.3) to assess the possible bias due to the use of a single set of parameters to describe the mean and the resolution in both samples.

The fit model assumes no correlations between the two fit observables $m_{\eta'K}$ and $m_{\pi\pi\gamma}$. Possible correlations for the background are studied performing a fit using the same model but allowing for a dependence on $m_{\eta'K}$ of the slope of the $m_{\pi\pi\gamma}$ PDF (and vice versa). The variation in the signal yield is of the order of 0.02%, which is negligible, therefore validating the assumption of independence.

Table 4.3 – Simultaneous fit of the $B^+ \rightarrow \eta' K^+$ candidates selected in the 2011 and 2012 real data samples with different masses and resolution parameters for the 2011 and 2012 datasets.

Parameter			Value and uncertainty	
			2011	2012
B^+ mass	m_B	[MeV/ c^2]	5281.38 ± 0.49	5283.04 ± 0.33
η' mass	$m_{\eta'}$	[MeV/ c^2]	958.33 ± 0.32	959.37 ± 0.21
B^+ mass resolution	σ_B	[MeV/ c^2]	21.07 ± 0.46	22.02 ± 0.31
η' mass resolution	$\sigma_{\eta'}$	[MeV/ c^2]	12.42 ± 0.29	12.68 ± 0.19
Slope comb. background ($m_{\eta'K}$)	a		-0.38 ± 0.03	-0.33 ± 0.02
Slope comb. background ($m_{\eta'K}$)	b		-0.12 ± 0.03	-0.10 ± 0.02
Slope comb. background ($m_{\pi\pi\gamma}$)	a		-0.53 ± 0.02	-0.55 ± 0.03
Slope comb. background with true η'	a		-1.0 ± 0.3	-1.0 ± 0.3
$B^+ \rightarrow \eta' K^+$ signal yield			3203 ± 67	7886 ± 108
Comb. background yield			3106 ± 76	8071 ± 123
Comb. background yield with true η'			102 ± 49	313 ± 77

Study of the $B_s^0 \rightarrow \eta' \phi$ data sidebands

The signal functional form of the $B_s^0 \rightarrow \eta' \phi$ fit model is defined using simulated events. The background components are defined by studying the real data sidebands after the full selection is applied. Independent one-dimensional fits are performed for each of the two fit dimensions. In both fits the 2011 and 2012 datasets are merged, to avoid instabilities due to the low statistics. The results are shown in Fig. 4.5 and in Table 4.4.

4.3. Fit model validation

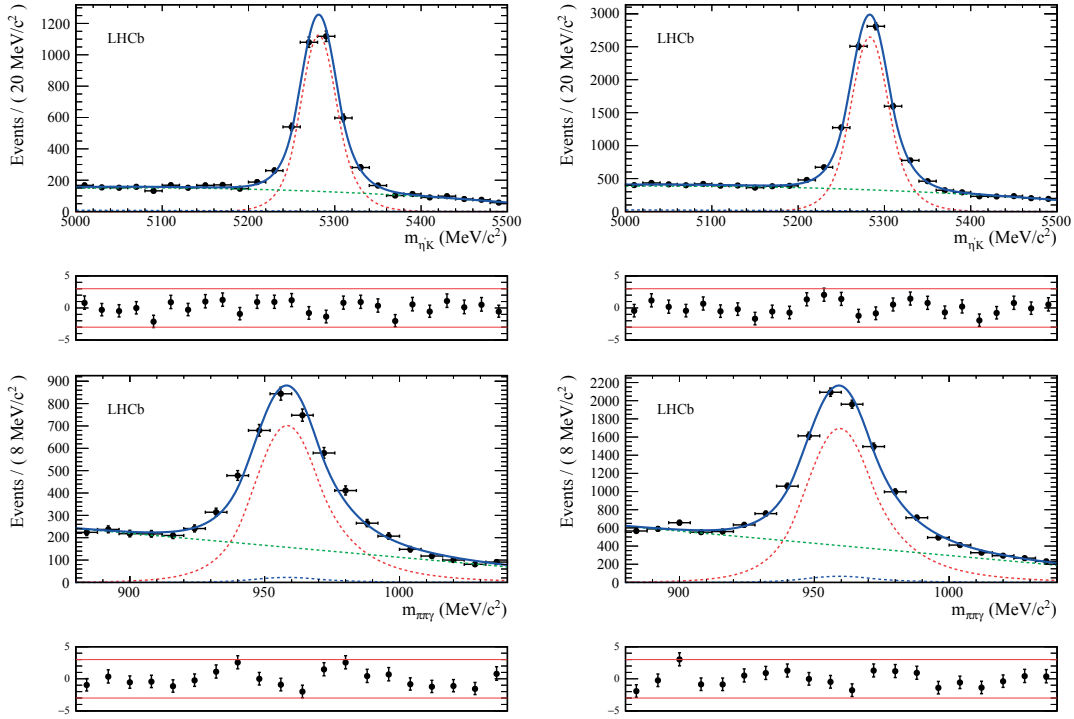


Figure 4.3 – $\eta' K^+$ (top) and $\pi^+ \pi^- \gamma$ (bottom) mass distributions of the $B^+ \rightarrow \eta' K^+$ candidates selected in the 2011 (left) and 2012 (right) data samples with fit results superimposed. The solid blue curves represent the result of the simultaneous two-dimensional fit described in the text, with the following components: $B_s^0 \rightarrow \eta' \phi$ signal (red dashed), combinatorial background (green dashed) and combinatorial background with true η' (blue dashed). The fit pulls are displayed below each histogram.

The first fit is performed on the $\eta' K^+ K^-$ mass distribution of the 208 candidates falling in the sidebands of the η' signal ($|m_{\pi\pi\gamma} - 957.8| > 43 \text{ MeV}/c^2$). The shape parameters, except the combinatorial slopes, have been fixed to the values obtained from the fit to the simulated data or $B^+ \rightarrow \eta' K^+$ real data. No significant peaking B_s^0 background is found.

The second fit is performed on the $\pi^+ \pi^- \gamma$ mass distribution of the 319 candidates falling in the sidebands of the B_s^0 signal ($|m_{\eta' KK} - 5366.7| > 79.5 \text{ MeV}/c^2$). The background component with peaking η' is found to be negligible. A broad structure centred at $980 \text{ MeV}/c^2$ is not described by the fit. This excess is attributed to a $\phi \rightarrow \pi^+ \pi^- \pi^0$ decays from the $B_s^0 \rightarrow \phi\phi$ physics background. The two sidebands have been studied separately (Fig. 4.6), and in particular the low-mass sideband is separated into two regions ($m_{\eta' KK} > 5100 \text{ MeV}/c^2$ and $m_{\eta' KK} < 5100 \text{ MeV}/c^2$), to better isolate the expected $B_s^0 \rightarrow \phi\phi$ background contribution. While the shape of the $\pi^+ \pi^- \gamma$ mass distribution for $m_{\eta' KK} < 5100 \text{ MeV}/c^2$ is similar to that of the high-mass sideband, within the statistical fluctuations, the mass region for $m_{\eta' KK} > 5100 \text{ MeV}/c^2$ presents a structure due to the $B_s^0 \rightarrow \phi\phi$ contamination. For this reason, a component to describe the $B_s^0 \rightarrow \phi\phi$ contribution is implemented in the fit model described in Sec 4.2. The PDF of this background is obtained from a sample of fully simulated $B_s^0 \rightarrow \phi\phi$ decays, reconstructed and selected as

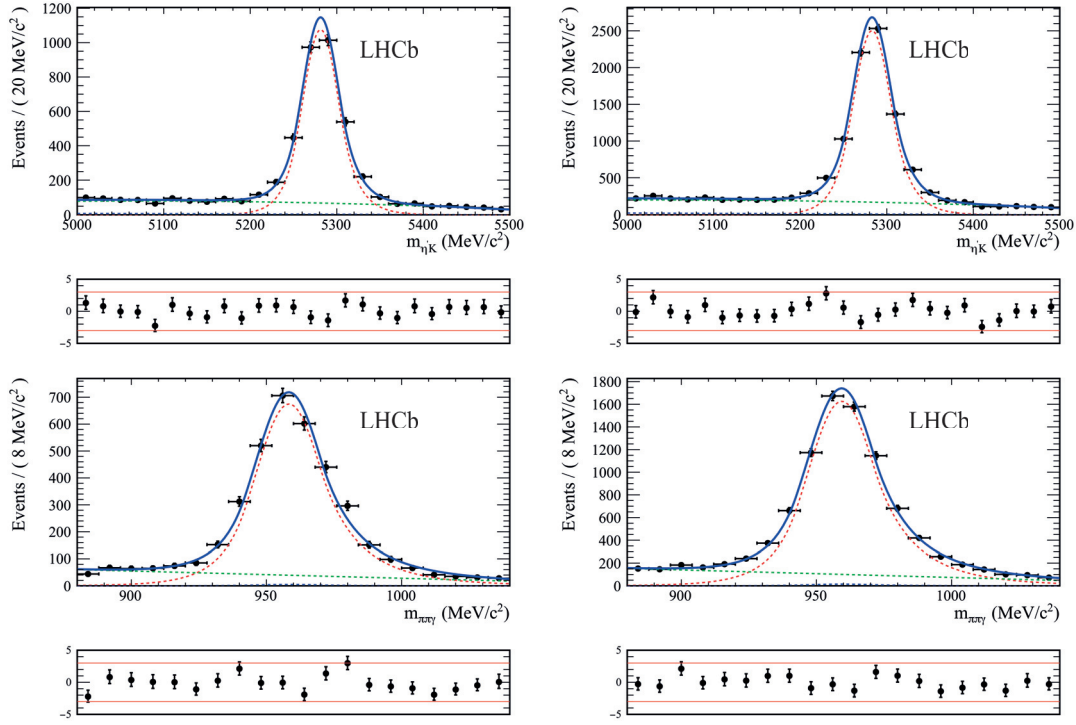


Figure 4.4 – $\eta' K^+$ mass distribution in the η' signal region ($|m_{\pi\pi\gamma} - 957.8| < 40 \text{ MeV}/c^2$) (top) and $\pi^+ \pi^- \gamma$ mass distribution in the B^+ signal region ($|m_{\eta'K} - 5279.3| < 60 \text{ MeV}/c^2$) (bottom) for the $B^+ \rightarrow \eta' K^+$ candidates selected in the 2011 (left) and 2012 (right) data samples. The solid blue curves represent the result of the simultaneous two-dimensional fit described in the text, with the following components: $B^+ \rightarrow \eta' K^+$ signal (red dashed), combinatorial background (green dashed) and combinatorial background with real η' (blue dashed). The fit pulls are displayed below each histogram.

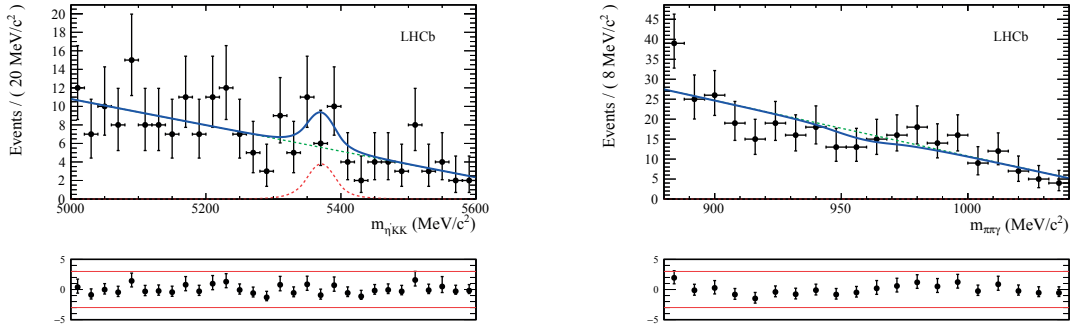


Figure 4.5 – $\eta' K^+ K^-$ mass distribution in the η' sideband regions (left) and $\pi^+ \pi^- \gamma$ mass distribution in the B_s^0 sideband regions (right) for the $B_s^0 \rightarrow \eta' \phi$ candidates selected in the 2011 and 2012 data. The solid blue curves represent the results of the one-dimensional fits described in the text with the following components: peaking backgrounds (red dashed) and combinatorial backgrounds (green dashed). No significant narrow peaking structure is identified. The fit pulls are displayed below each histogram.

Table 4.4 – Results obtained from one-dimensional fits of the $\pi^+\pi^-\gamma$ and $\eta'K^+K^-$ mass distributions of the 2011 and 2012 merged datasets. The fits are performed on the $B_s^0 \rightarrow \eta'\phi$ candidates excluding the B_s^0 and η' signal regions, as described in the text.

Parameter	Value and error
$m_{\pi^+\pi^-\gamma}$ fit (319 candidates)	
Yield of combinatorial background with η'	-8 ± 14
Yield of combinatorial background	327 ± 23
$m_{\eta'\phi}$ fit (208 candidates)	
Yield of combinatorial background with B_s^0	11 ± 6
Yield of combinatorial background	197 ± 15

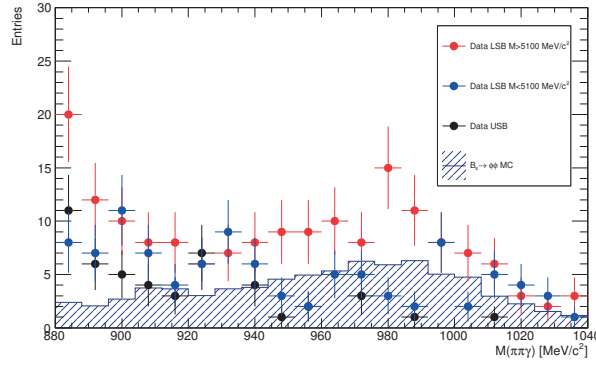


Figure 4.6 – $\pi^+\pi^-\gamma$ mass distribution of the data candidates falling in the $\eta'K^+K^-$ sidebands: low-mass sideband with $m_{\eta'KK} < 5100 \text{ MeV}/c^2$ (blue points) or $m_{\eta'KK} > 5100 \text{ MeV}/c^2$ (red points), and high-mass sideband (black points). The blue-hatched histogram represents the $\pi^+\pi^-\gamma$ mass distribution of $B_s^0 \rightarrow \phi\phi$ simulated events reconstructed and selected as $B_s^0 \rightarrow \eta'\phi$ candidates.

$B_s^0 \rightarrow \eta'\phi$ candidates. The `RoofitKeysPdf` method, described in Sec. 4.2, is used to build the functional form. In particular, we extract directly from MC a two-dimensional PDF to take into account the non-negligible correlation observed between the $m_{\eta'K^+K^-}$ and $m_{\pi^+\pi^-\gamma}$ variables (see Fig. 4.7).

4.3.3 Fit validation using fast simulation

The fit sensitivity, biases and stability are evaluated using fast simulation samples (MC pseudo-experiments). A significant number of samples of simulated events reproducing the characteristics of the real data samples, called also “toy” samples, are generated and then fitted with the fit model that we intend to test. Each toy experiment has the same statistics as in real data. Two types of pseudo-experiments are performed:

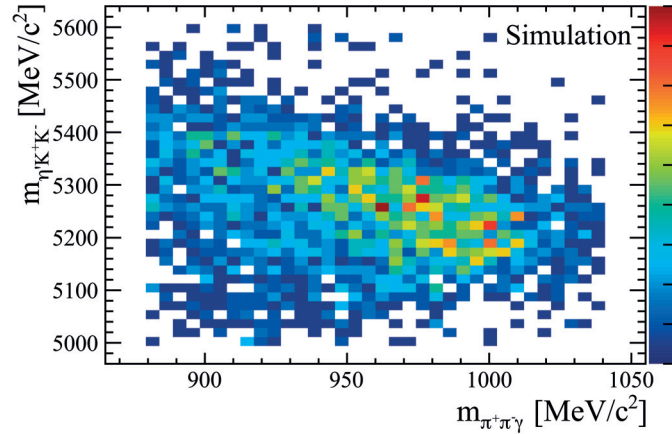


Figure 4.7 – Scatter plot of the $\pi^+\pi^-\gamma$ and $\eta'K^+K^-$ masses for $B_s^0 \rightarrow \phi\eta'$ MC events, reconstructed as $B_s^0 \rightarrow \eta'\phi$ candidates.

- “pure toys”, for which the generation of each component is obtained from the PDFs used in the fit model. These pseudo-experiments are used to evaluate the sensitivity and the stability of the fit, and possible fit biases;
- “embedded toys”, where one or more components consist of events taken randomly from fully-simulated MC samples and the others are generated from the PDFs. These toy samples are used to study biases introduced by correlations between fit variables or mis-modeled PDFs.

The distributions of the fitted parameters are expected to be Gaussian and centred on the generated values. To check the correct estimation of each parameter and its uncertainty, the pull distribution is examined. The pull is defined as

$$\theta_{\text{pull}} = \frac{\theta_{\text{fit}} - \theta_{\text{gen}}}{\sigma_{\text{fit}}}, \quad (4.10)$$

where θ_{gen} is the value of the parameter used in the sample generation, and θ_{fit} and σ_{fit} are the estimated value and uncertainty obtained from the fit. The pull distribution is expected to be Gaussian, centred at zero and with unit standard deviation.

Pure toy studies

Simultaneous fits of the $B_s^0 \rightarrow \eta'\phi$ and $B^+ \rightarrow \eta'K^+$ pure toy samples are performed using the fit model described in Sec. 4.2. The 2011 and 2012 data are generated with separate parameters, while the fits are performed merging the 2012 and 2011 datasets, with all parameters shared. This is done to test a possible bias due to the assumption (presented in Sec. 4.2) that the 2011 and 2012 samples have compatible parameters and therefore can be merged. All the parameters to describe the η' shape are shared between $B_s^0 \rightarrow \eta'\phi$ and $B^+ \rightarrow \eta'K^+$ and are

taken from the $B^+ \rightarrow \eta' K^+$ fit in real data (Sec. 4.3.2). The resolution and mass parameters of the B^+ candidates are also derived from the same fit, while, the corresponding B_s^0 parameters are constrained as explained in Sec. 4.2. The samples are generated assuming a $B_s^0 \rightarrow \eta' \phi$ branching fraction of 4×10^{-6} . This assumption corresponds to a signal yield of ~ 40 events (39 generated in toys). The computation of the number of expected signal events is presented in Sec. 3.9.

The results of the toy studies are summarised in Table 4.5. No evidence of a bias is observed for the $B_s^0 \rightarrow \eta' \phi$ and the $B^+ \rightarrow \eta' K^+$ signal yields. The $B_s^0 \rightarrow \eta' \phi$ signal yield, its uncertainty and the associated pull distribution are shown in Fig. 4.8 (left). All the fits converge, showing a good stability of the model. The mean value of the $B_s^0 \rightarrow \eta' \phi$ significance obtained with the pure toy studies is 5.7σ , as shown in Fig. 4.9. As an example, the fit result of a single toy experiment is shown in Fig. 4.10, and the projections in the signal regions for $B_s^0 \rightarrow \eta' \phi$ are shown in Fig. 4.11. For this experiment, a significance of 5.9σ is obtained.

The same fit model is used to perform pure toy studies assuming different values for the number of signal events: 0, 20, 78. The results, shown in Table 4.6, are fairly linear with respect to the expected significance, and a significance of 3σ is obtained in the case of 20 signal events (corresponding to a branching fraction of 2×10^{-6}). A small negative bias is observed when no signal events are generated, which is due to the low statistics in the signal region. The observed significant bias on the pull mean reflects the fact that the uncertainty is underestimated on the few most negative yields.

Embedded toy studies

The fit model is further validated using toy samples in which the $B_s^0 \rightarrow \eta' \phi$ signal and the $B_s^0 \rightarrow \phi\phi$ partially reconstructed background components are randomly selected from the MC simulated events, in order to investigate the effect of a possible correlation between the two fitted masses, assumed to be uncorrelated in the fit model. A bias observed in these studies would also include the effect of the choice of rejecting the multiple candidates using the requirement on photon CL. Moreover, the description of the $B_s^0 \rightarrow \phi\phi$ background PDF is validated.

Toy samples with 39 $B_s^0 \rightarrow \eta' \phi$ signal events and 103 $B_s^0 \rightarrow \phi\phi$ events are generated and fitted. In order to understand the contributions of the two components to a possible bias, three sets of embedded toy samples are generated: only $B_s^0 \rightarrow \phi\phi$ is embedded; only $B_s^0 \rightarrow \eta' \phi$ signal is embedded; and both components are embedded. In the case where the signal is embedded, an efficiency factor is considered in the generation procedure, to account for the fact that the MC samples contain a small fraction of mis-reconstructed events. For this reason, 43 events are taken from the MC sample, containing on average 39 signal events. The results are summarised in Table 4.5 and displayed in Fig. 4.8 (right). All fits converge. The resulting total bias on the signal yield, corresponding to -1.1 event has a contribution from residual correlations between the fit variables in the signal and from contamination due to the $B_s^0 \rightarrow \phi\phi$ component. A correction for this bias is included in the final result, and a systematic uncertainty on the correction is considered.

Chapter 4. $B_s^0 \rightarrow \eta' \phi$ signal extraction and results

Table 4.5 – Results obtained from fits to pure and embedded toy MC samples. The number of generated events (“In”), the mean value of the distribution of the fitted yield (“Out”), the mean value of the distribution of the error on the fitted yield (“Err”) and the mean bias on the fitted yield (“Bias”, computed as “Out”–“In”) are shown for the $B_s^0 \rightarrow \eta' \phi$, $B_s^0 \rightarrow \phi \phi$ and $B^+ \rightarrow \eta' K^+$ components.

Component	In	Out	Err	Bias	Pull mean	Pull σ
Pure toy samples						
$B_s^0 \rightarrow \phi \eta'$	39	39.1	8.9	$+0.1 \pm 0.3$	-0.05 ± 0.03	1.00 ± 0.02
$B_s^0 \rightarrow \phi \phi$	103	103.5	29.7	$+0.5 \pm 0.9$	$+0.00 \pm 0.03$	0.97 ± 0.02
$B^+ \rightarrow \eta' K^+$	11089	11088	126.1	-1 ± 4	-0.01 ± 0.03	0.97 ± 0.02
Toy samples with embedded $B_s^0 \rightarrow \phi \phi$						
$B_s^0 \rightarrow \phi \eta'$	39	38.2	8.4	-0.8 ± 0.2	-0.2 ± 0.03	1.07 ± 0.02
$B_s^0 \rightarrow \phi \phi$	103	113.3	25.8	$+10.3 \pm 0.7$	$+0.41 \pm 0.03$	0.98 ± 0.03
$B^+ \rightarrow \eta' K^+$	11089	11087	121.9	-2 ± 2	-0.04 ± 0.03	1.01 ± 0.02
Toy samples with embedded $B_s^0 \rightarrow \eta' \phi$						
$B_s^0 \rightarrow \phi \eta'$	39	38.8	8.5	-0.2 ± 0.2	-0.14 ± 0.03	1.09 ± 0.02
$B_s^0 \rightarrow \phi \phi$	103	104	29.5	$+1 \pm 0.9$	$+0.02 \pm 0.03$	0.96 ± 0.02
$B^+ \rightarrow \eta' K^+$	11089	11085	121.9	-4 ± 2	-0.08 ± 0.03	1.01 ± 0.02
Toy samples with embedded $B_s^0 \rightarrow \eta' \phi$ and $B_s^0 \rightarrow \phi \phi$						
$B_s^0 \rightarrow \phi \eta'$	39	37.9	8.3	-1.1 ± 0.2	-0.33 ± 0.04	1.18 ± 0.03
$B_s^0 \rightarrow \phi \phi$	103	114	25.9	$+11.0 \pm 0.7$	$+0.43 \pm 0.03$	0.98 ± 0.02
$B^+ \rightarrow \eta' K^+$	11089	11088	121.9	-1 ± 2	-0.03 ± 0.03	1.01 ± 0.02

Table 4.6 – Signal results obtained from fits to pure toy samples for different numbers of generated $B_s^0 \rightarrow \eta' \phi$ signal events (“In”). The mean value of the distribution of the fitted signal yield (“Out”), the mean value of the distribution of the error on the fitted signal yield (“Err”), the mean bias on the fitted signal yield (“Bias”, computed as “Out”–“In”) and the mean signal significance are shown.

Component	In	Out	Err	Bias	Pull mean	Pull σ	Significance
$B_s^0 \rightarrow \eta' \phi$	0	-0.2	5.1	-0.2 ± 0.2	-0.19 ± 0.03	1.13 ± 0.03	0
$B_s^0 \rightarrow \eta' \phi$	20	20.0	7.3	$+0.0 \pm 0.2$	$+0.08 \pm 0.03$	1.06 ± 0.02	3.2
$B_s^0 \rightarrow \eta' \phi$	39	39.1	8.9	$+0.1 \pm 0.3$	$+0.05 \pm 0.03$	0.99 ± 0.02	5.7
$B_s^0 \rightarrow \eta' \phi$	78	77.7	11.2	-0.3 ± 0.3	-0.07 ± 0.03	1.01 ± 0.02	9.8

4.4. Search for the $B_s^0 \rightarrow \eta' \phi$ signal

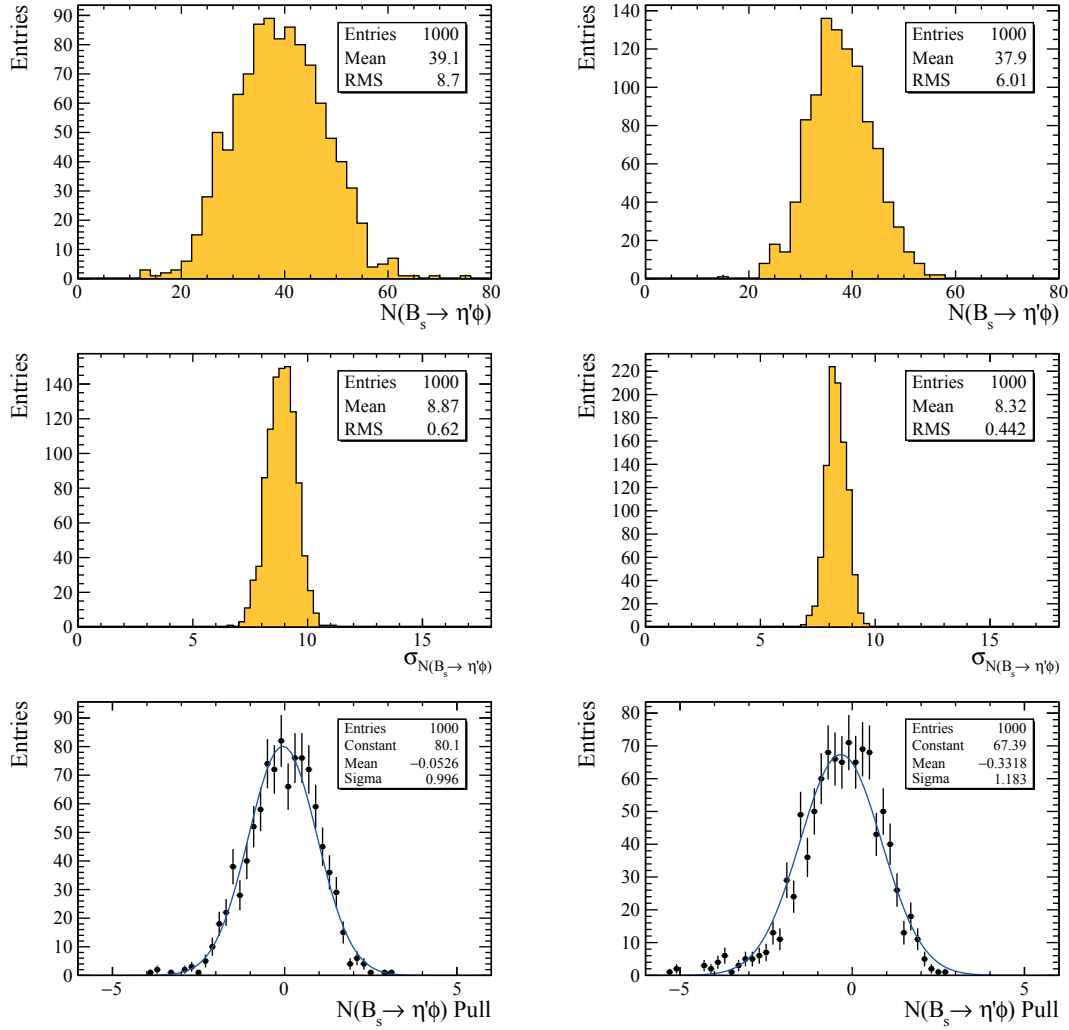


Figure 4.8 – Distributions of the fitted $B_s^0 \rightarrow \eta' \phi$ yield (top), its estimated error (middle) and the corresponding pull (bottom), obtained from pure toy samples (left) and from the embedded toy samples with fully simulated $B_s^0 \rightarrow \eta' \phi$ and $B_s^0 \rightarrow \phi \phi$ events (right).

4.4 Search for the $B_s^0 \rightarrow \eta' \phi$ signal

In this section the result of the fit performed on the full samples of $B_s^0 \rightarrow \eta' \phi$ and $B^+ \rightarrow \eta' K^+$ data candidates is presented.

4.4.1 Fit result

The model described in Sec. 4.2 is applied to the real data samples, including the signal. No $B_s^0 \rightarrow \eta' \phi$ signal is observed, with a fitted yield of $N(B_s^0 \rightarrow \eta' \phi) = -3.2^{+5.0}_{-3.8}$ events. The fitted yield for the reference channel is $N(B^+ \rightarrow \eta' K^+) = 11081 \pm 127$ events, and that for the $B_s^0 \rightarrow \phi \phi$ physics background is 105 ± 29 events. The latter can be compared with the expectation of

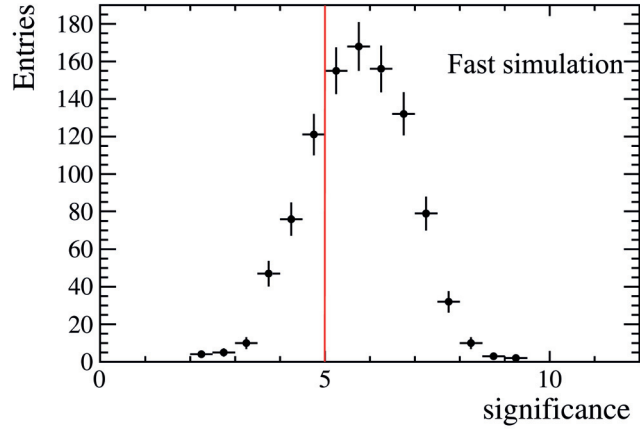


Figure 4.9 – Significance of the $B_s^0 \rightarrow \eta' \phi$ signal in pure toy samples, generated assuming a $B_s^0 \rightarrow \eta' \phi$ branching fraction of $\sim 4 \times 10^{-6}$ (39 signal events).

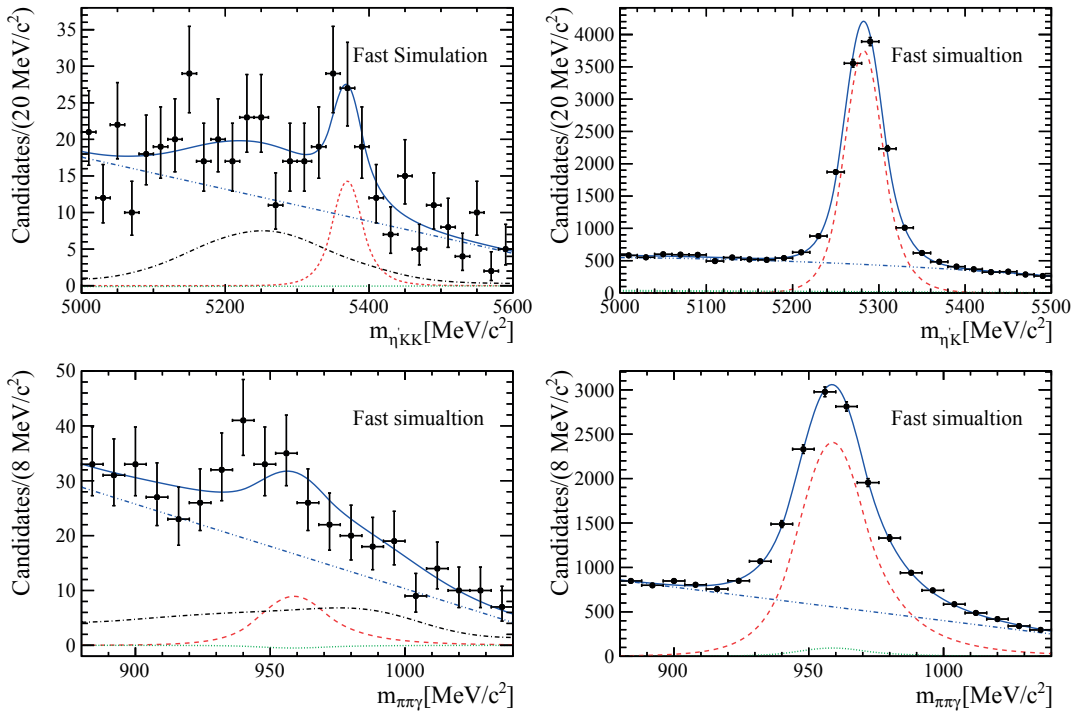


Figure 4.10 – Distributions of the $\eta' K^+ K^-$ (top left) and $\pi^+ \pi^- \gamma$ (bottom left) masses of the $B_s^0 \rightarrow \eta' \phi$ candidates, and of the $\eta' K^+$ (top right) and $\pi^+ \pi^- \gamma$ (bottom right) masses of the $B^+ \rightarrow \eta' K^+$ candidates, generated in a single pure toy experiment. The result of the simultaneous fit is superimposed (blue line) with the following components: $B_s^0 \rightarrow \eta' \phi$ and $B^+ \rightarrow \eta' K^+$ signals (red dashed), combinatorial backgrounds (blue dot-dot-dashed), combinatorial backgrounds with real η' (green dotted), and $B_s^0 \rightarrow \phi \phi$ background (black dot-dashed).

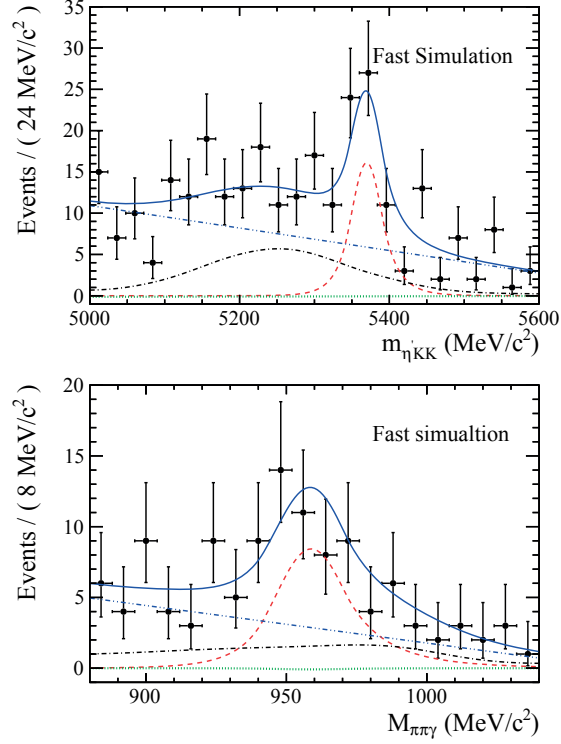


Figure 4.11 – Distributions of the $\eta' K^+ K^-$ mass when $|m_{\pi\pi\gamma} - 957.8| < 40 \text{ MeV}/c^2$ (top), and of the $\pi^+ \pi^- \gamma$ mass when $|m_{\eta' KK} - 5366.7| < 60 \text{ MeV}/c^2$ (bottom) for the $B_s^0 \rightarrow \eta' \phi$ candidates generated in the single pure toy experiment of Fig. 4.10. The fit result (blue line) is superimposed with the following components: $B_s^0 \rightarrow \eta' \phi$ signal (red dashed), combinatorial background (blue dot-dot-dashed), combinatorial background with real η' (green dotted), and $B_s^0 \rightarrow \phi\phi$ background (black dot-dashed).

104 ± 34 events. The full fit results are shown in Figs. 4.12, 4.13 and in Table 4.7. The fit is repeated a second time but introducing the ratio R between $N(B_s^0 \rightarrow \phi\eta')$ and $N(B^+ \rightarrow \eta' K^+)$ as fit parameter. The obtained value,

$$R = \frac{N(B_s^0 \rightarrow \eta' \phi)}{N(B^+ \rightarrow \eta' K^+)} = (-2.9_{-3.4}^{+4.5}) \times 10^{-4}, \quad (4.11)$$

is used in the computation of the $B_s^0 \rightarrow \eta' \phi$ branching fraction limit, presented in Sec. 4.4.3.

Further checks on the fit results

Additional tests are performed to check the quality of the fit result. A set of 1000 pseudo-experiments is generated, using as inputs the parameter values obtained from the fit on real data. As shown in Table 4.7, two components (the $B_s^0 \rightarrow \eta' \phi$ signal and the combinatorial background with true η') have a negative fitted yield. For those components the yields are set to zero in the toy generation, and the nominal yield of the combinatorial background is

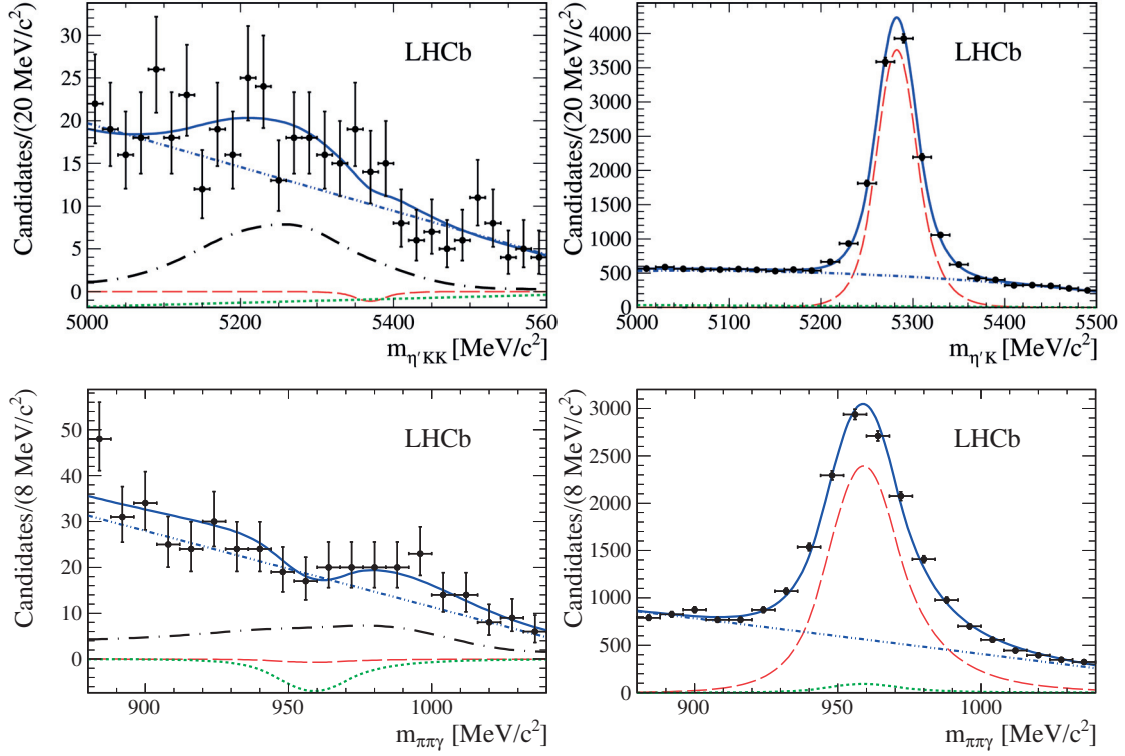


Figure 4.12 – Distributions of the $\eta' K^+ K^-$ (top left) and $\pi^+ \pi^- \gamma$ (bottom left) masses of the $B_s^0 \rightarrow \eta' \phi$ candidates, as well as of the $\eta' K^+$ (top right) and $\pi^+ \pi^- \gamma$ (bottom right) masses of the $B^+ \rightarrow \eta' K^+$ candidates selected in Run 1 data. The solid blue curves represent the result of the simultaneous two-dimensional fit described in the text, with the following components: $B_s^0 \rightarrow \eta' \phi$ and $B^+ \rightarrow \eta' K^+$ signals (red dashed), combinatorial backgrounds with real η' (green dotted), pure combinatorial backgrounds (blue dot-dot-dashed), and $B_s^0 \rightarrow \phi \phi$ background (black dot-dashed). Some of the components are barely visible because the corresponding yields are small.

reduced to keep the total size of each generated sample equal to that of the real data sample. The results of the fits to these toy samples are presented in Table 4.8. The values are consistent with those obtained in real data. In the cases of the $B_s^0 \rightarrow \eta' \phi$ signal and the combinatorial background with true η' , the uncertainties in data are slightly smaller than the average value in the toy experiments. This is a consequence of the correlations between the measured yields and their uncertainties (see Fig. 4.14). However, the value and uncertainty obtained in real data are relatively frequent in the toy experiments and therefore can be considered as expected statistical fluctuations. The distributions for all the fit variables and the comparison with the real data values is shown in Fig. 4.15.

The consistency of the fit model with the data is also evaluated by comparing the value of the likelihood in data with the distribution of likelihood values obtained from fits to the samples generated from the fit model. Figure 4.16 shows the distribution of the negative likelihood logarithm ($-\ln \mathcal{L}$) for the set of pseudo-experiments. The blue arrow indicating the value

4.4. Search for the $B_s^0 \rightarrow \eta' \phi$ signal

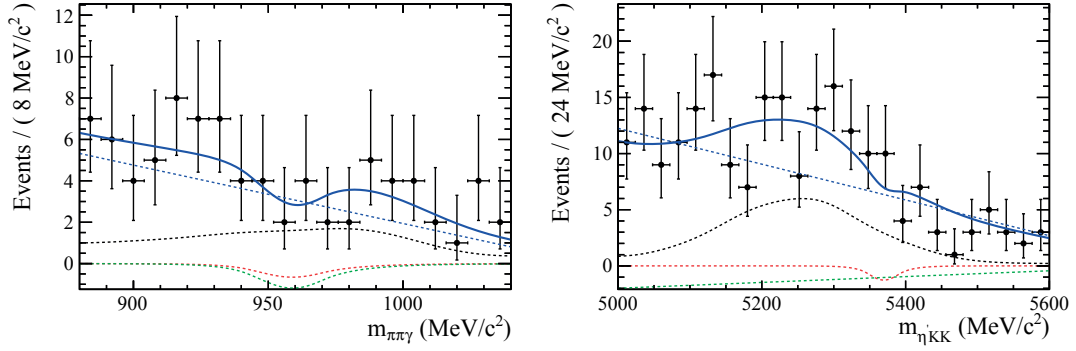


Figure 4.13 – Distributions of the $\pi^+\pi^-\gamma$ (left) and $\eta'K^+K^-$ (right) masses falling in the signal region of the other mass for the $B_s^0 \rightarrow \eta' \phi$ candidates selected in Run 1 data. The fit result (solid blue curve) is superimposed with the following components: $B_s^0 \rightarrow \eta' \phi$ signal (red dashed), combinatorial background with real η' (green dotted), pure combinatorial background (blue dot-dot-dashed), and $B_s^0 \rightarrow \phi\phi$ background (black dot-dashed).

Table 4.7 – Result of the simultaneous fit of the $B^+ \rightarrow \eta' K^+$ and $B_s^0 \rightarrow \eta' \phi$ candidates selected in Run 1 data.

Parameter		Value and error
B^+ mass	m_B [MeV/c ²]	5282.49 ± 0.27
B^+ mass resolution	σ_B [MeV/c ²]	21.83 ± 0.26
η' mass	$m_{\eta'}$ [MeV/c ²]	959.06 ± 0.17
η' mass resolution	$\sigma_{\eta'}$ [MeV/c ²]	12.60 ± 0.16
Slope comb. background in $B^+ \rightarrow \eta' K^+$ ($m_{\eta'K}$)	a	-0.34 ± 0.02
Slope comb. background in $B^+ \rightarrow \eta' K^+$ ($m_{\eta'K}$)	b	-0.11 ± 0.02
Slope comb. background in $B^+ \rightarrow \eta' K^+$ ($m_{\pi\pi\gamma}$)	a	-0.54 ± 0.02
Slope comb. background with true η' in $B^+ \rightarrow \eta' K^+$	a	-1.0 ± 0.3
Slope comb. background in $B_s^0 \rightarrow \eta' \phi$ ($m_{\eta'KK}$)	a	-0.64 ± 0.08
Slope comb. background in $B_s^0 \rightarrow \eta' \phi$ ($m_{\pi\pi\gamma}$)	a	-0.74 ± 0.08
$B^+ \rightarrow \eta' K^+$ signal yield		11081 ± 127
$B^+ \rightarrow \eta' K^+$ combinatorial background yield with true η'		424 ± 91
$B^+ \rightarrow \eta' K^+$ combinatorial background yield		11177 ± 144
$B_s^0 \rightarrow \phi \eta'$ signal yield		-3.2 ± 4.4
$B_s^0 \rightarrow \eta' \phi$ combinatorial background yield with true η'		-32.2 ± 14.8
$B_s^0 \rightarrow \eta' \phi$ combinatorial background yield		360.3 ± 33.2
$B_s^0 \rightarrow \phi\phi$ background yield		105.2 ± 28.9

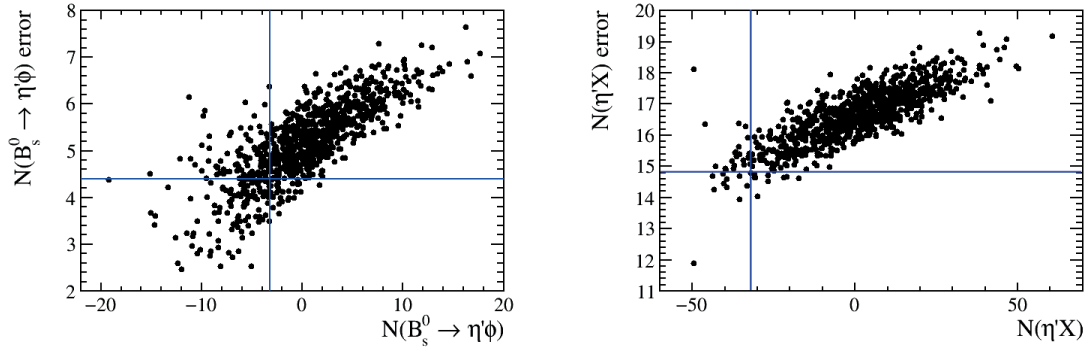


Figure 4.14 – Scatter plot of the fitted yield and its uncertainty for the $B_s^0 \rightarrow \eta' \phi$ signal (left) and the combinatorial background with true η' (right) obtained with toy samples. The blue lines indicate the values obtained from the fit to the real data.

Table 4.8 – Yields for each component of the model obtained from fits to pure toy samples reproducing the real data fit results. The number of generated events (“In”), the mean value of the distribution of the fitted yield (“Out”), and the mean value of the distribution of the error on the fitted yield (“Err”) are shown. The last column reports the result of the fit on data for comparison.

Component	In	Out	Err	Data fit result
$B_s^0 \rightarrow \phi \eta'$	0	0.2	5.2	-3.2 ± 4.4
$B_s^0 \rightarrow \phi \phi$ background	105	101.6	29.9	105.2 ± 28.9
Comb. background	325	327.3	33.4	360.3 ± 33.2
Comb. background with true η'	0	0.8	16.7	-32.2 ± 14.8
$B^+ \rightarrow \eta' K^+$	11081	11083.5	126.1	11081 ± 127
Comb. background	11177	11177.3	143.0	11177 ± 144
Comb. background with true η'	424	420.5	88.8	424 ± 91

obtained from the fit to real data is fully consistent with the values obtained from the model, which is expected if the fit model is representative of the data.

4.4.2 Fit systematic uncertainties

Several sources of systematic uncertainty due to the fit model are considered and evaluated. The computed values for the yield and for the yield ratio are summarized in Table 4.9 and quoted in parentheses in the description below.

Fit model (combinatorial background shape) In order to account for systematic effects introduced by the functions used in the model, studies on the variation of the fit results depending on the functions are performed:

4.4. Search for the $B_s^0 \rightarrow \eta' \phi$ signal

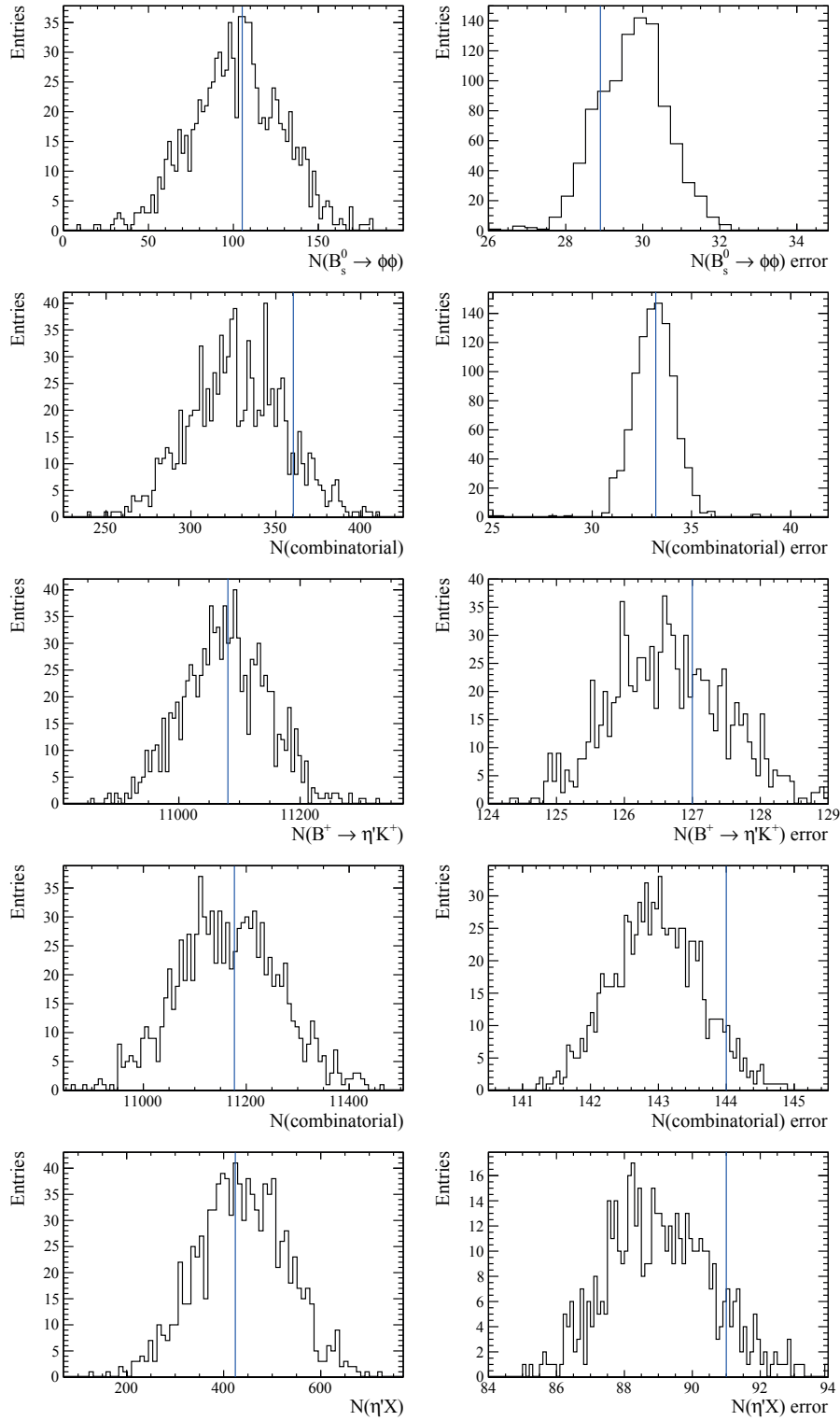


Figure 4.15 – Distributions of the fitted yield (left) and error (right) of each component in the $B_s^0 \rightarrow \eta' \phi$ sample (first two rows) and in the $B^+ \rightarrow \eta' K^+$ sample (last three rows) as obtained from a set of 1000 pseudo-experiments. For these toys the number of generated events and the shape parameters are set to the central values from the fit on real data. The blue lines indicate the results obtained from the fit to the real data.

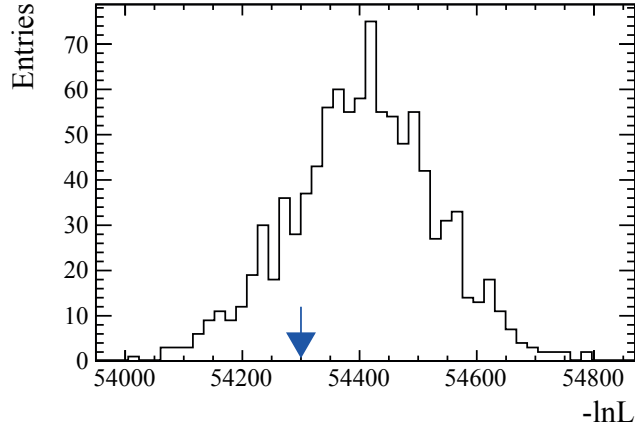


Figure 4.16 – Distribution of the minimised $-\ln \mathcal{L}$ values in pseudo-experiments. The blue arrow indicates the value obtained from the fit to the real data.

Table 4.9 – Systematic uncertainties σ_N and σ_R on the fitted yield $N(B_s^0 \rightarrow \eta' \phi)$ and on the yield ratio $R = N(B_s^0 \rightarrow \eta' \phi) / N(B^+ \rightarrow \eta' K^+)$, respectively. The last line gives the quadratic sum of the individual uncertainties.

Source	σ_N (events)	σ_R (10^{-4})
Combinatorial background modeling	0.6	0.6
$B_s^0 \rightarrow \phi\phi$ background modeling	0.4	0.3
Fixed parameters in the fit	0.3	0.3
Fit bias	0.7	0.7
Total	1.1	1.0

- The linear functions used to fit the combinatorial background in the $\eta' K^+$, $\eta' K^+ K^-$ and $\pi^+ \pi^- \gamma$ mass distributions are replaced by exponential functions (± 0.43 ; $\pm 0.42 \times 10^{-4}$);
- The quadratic shape used to fit the combinatorial in the $\eta' K^+$ mass distribution is replaced with a third-order polynomial (± 0.00 ; ± 0.00);
- The slope of the linear function describing the combinatorial background with true η' , which is shared with the pure combinatorial component in the $m_{\eta' K K}$ dimension, is allowed to fluctuate (± 0.45 ; $\pm 0.41 \times 10^{-4}$).

The contribution to the systematic uncertainty is evaluated as the sum in quadrature of the differences between the value obtained in these fits and the nominal result (± 0.62 ; $\pm 0.59 \times 10^{-4}$).

Fit model ($B_s^0 \rightarrow \phi\phi$ shape) The determination of the PDF used to describe the $B_s^0 \rightarrow \phi\phi$ background is limited by the statistics of the MC samples from which the `RoofitKeyPdf` is

determined. The related systematic uncertainty is evaluated in the following way:

1. A RooNDKeyPdf PDF is determined using the $B_s^0 \rightarrow \phi\phi$ MC samples;
2. The PDF is then used to generate a sample of $B_s^0 \rightarrow \phi\phi$ events from which a second RooNDKeyPdf is determined;
3. The second PDF is then used to fit the data;
4. Step 2. and step 3. are repeated 1000 times.

The RMS of the distribution (of the signal yield, yield ratio) is taken as systematic uncertainty (± 0.40 ; $\pm 0.34 \times 10^{-4}$).

Fit model (signal shape) To account for the systematic effects introduced by fixing several parameters in the nominal fit model, the data are fitted 1000 times and for each fit the fixed parameters ($\alpha_L(B_s^0)$, $\alpha_R(B_s^0)$, $n_L(B_s^0)$, $n_R(B_s^0)$), for the B_s^0 peaking components, $\alpha_L(\eta')$, $\alpha_R(\eta')$, $n_L(\eta')$, $n_R(\eta')$, for the η' resonance, the difference $m_{B_s^0} - m_{B^+}$ and the ratio of resolutions $\sigma_{B_s^0}/\sigma_{B^+}$ are sampled randomly from Gaussian distributions centred on the value used in the nominal fit and with widths and correlations as determined in simulation. The RMS of the distribution (of the signal yield, yield ratio) is taken as systematic uncertainty (± 0.30 ; $\pm 0.27 \times 10^{-4}$).

Fit model (bias) The contribution to the systematic uncertainty due to the observed fit bias is evaluated with embedded toys as described in Sec. 4.3.3. This study is repeated after the fit results on data have been obtained. In 200 toy experiments, the $B_s^0 \rightarrow \phi\phi$ component is embedded from MC, while the signal yield is set to zero in the generation. The bias is found to be -1.3 ± 0.3 for the yield and $(-1.16 \pm 0.33) \times 10^{-4}$ for the yield ratio. The nominal value is corrected for this bias and a systematic uncertainty is assigned due to the correction. The uncertainty is evaluated as the sum in quadrature of the statistical uncertainty on the bias and half of the bias value (± 0.74 , $\pm 0.67 \times 10^{-4}$).

4.4.3 Branching fraction limit and final result

The $B_s^0 \rightarrow \eta' \phi$ branching fraction is computed using the formula

$$\mathcal{B}(B_s^0 \rightarrow \eta' \phi) = \frac{\mathcal{B}(B^+ \rightarrow \eta' K^+)}{\mathcal{B}(\phi \rightarrow K^+ K^-)} \times \frac{f_u}{f_s} \times \frac{N(B_s^0 \rightarrow \eta' \phi)}{N(B^+ \rightarrow \eta' K^+)} \times \frac{\epsilon^{\text{total}}(B^+ \rightarrow \eta' K^+)}{\epsilon^{\text{total}}(B_s^0 \rightarrow \eta' \phi)}, \quad (4.12)$$

where $\mathcal{B}(B^+ \rightarrow \eta' K^+) = (70.6 \pm 2.5) \times 10^{-6}$ [13] is the branching fraction of the normalisation channel, $\mathcal{B}(\phi \rightarrow K^+ K^-) = 0.489 \pm 0.005$ [13] represents the probability for the ϕ meson to decay in two kaons, f_u/f_s is the B^+/B_s^0 production ratio assumed to be equal to the B^0/B_s^0

production ratio $f_d/f_s = 1/(0.259 \pm 0.015)$ [83], and $\epsilon^{\text{total}}(B_s^0 \rightarrow \eta' \phi)/\epsilon^{\text{total}}(B^+ \rightarrow \eta' K^+)$ is the ratio of efficiencies for the signal and normalisation modes as computed in Sec. 3.8. The ratio of the observed yields $R = N(B_s^0 \rightarrow \eta' \phi)/N(B^+ \rightarrow \eta' K^+)$ is taken from the fit. Since the measured signal yield has a significance smaller than 3σ , an upper limit is computed. A Bayesian approach is used, assuming a flat prior in the observable x (yield, yield ratio, or branching fraction). The likelihood is maximised for fixed values of the observable x , while all other parameters are free to fluctuate. The upper limit x_U is calculated as $\int_0^{x_U} \mathcal{L}(x) dx / \int_0^\infty \mathcal{L}(x) dx = \alpha$, where $\mathcal{L}(x)$ is the likelihood function convolved with the systematic uncertainties, and α is the confidence level (CL).

The computation of the limits must account for the effect of the systematic uncertainties. Two types of systematic errors are considered: additive systematic uncertainties on the signal yield or yield ratio, and multiplicative systematic uncertainties related to the factors appearing in Eq. 4.12, such as the efficiency ratio. From the likelihood as a function of the yield ratio R , $\mathcal{L}(R)$, we define a function $\sigma_{\text{stat}}(R)$ with the relation

$$-2 \ln \mathcal{L}(R) = \frac{(R - R_0)^2}{\sigma_{\text{stat}}^2(R)}, \quad (4.13)$$

where R_0 is the value of the fit variable R that minimises $-2 \ln \mathcal{L}(R)$. The value $\sigma_{\text{stat}}(R_0)$ represents the parabolic statistical error on R_0 . If $\sigma_{\text{stat}}(R)$ was constant, equal to $\sigma_{\text{stat}}(R_0)$, then the likelihood would have a Gaussian behaviour. However our formalism allows for a non Gaussian behaviour. The total uncertainty on the yield ratio is taken as the quadratic sum of the statistical uncertainty and the Gaussian additive systematic uncertainty σ_{syst} . The total uncertainty including statistical and Gaussian additive systematic errors can be written as:

$$\sigma_{\text{tot}}^2(R) = \sigma_{\text{stat}}^2(R) + \sigma_{\text{syst}}^2. \quad (4.14)$$

The resulting likelihood function, including systematics,

$$-2 \ln \mathcal{L}_{\text{tot}}(R) = \frac{(R - R_0)^2}{\sigma_{\text{tot}}^2(R)} = \frac{-2 \ln \mathcal{L}(R)}{1 - 2 \ln \mathcal{L}(R) \frac{\sigma_{\text{syst}}^2}{(R - R_0)^2}}, \quad (4.15)$$

is shown in Fig. 4.17 (after correction for the fit bias). Writing the branching fraction as $\mathcal{B} = Rc$, where c contains all the multiplicative factors of Eq. 4.12, we obtain the likelihood as

$$-2 \ln \mathcal{L}(\mathcal{B}) = -2 \ln \mathcal{L}_{\text{tot}}\left(\frac{\mathcal{B}}{c}\right) \times \frac{1}{1 - 2 \ln \mathcal{L}_{\text{tot}}\left(\frac{\mathcal{B}}{c}\right) \frac{R_0^2 \sigma_c^2}{(\mathcal{B} - \mathcal{B}_0)^2}}. \quad (4.16)$$

The obtained upper limits for the signal yield and the yield ratio, including the bias correction and systematic uncertainties, are

$$N(B_s^0 \rightarrow \eta' \phi) < 8.9 \text{ (10.9)} \quad \text{at 90\% (95\%) CL} \quad (4.17)$$

and

$$\frac{N(B_s^0 \rightarrow \eta' \phi)}{N(B^+ \rightarrow \eta' K^+)} < 8.0 \text{ (9.9)} \times 10^{-4} \quad \text{at 90\% (95\%) CL.} \quad (4.18)$$

The central value of the $B_s^0 \rightarrow \eta' \phi$ branching fraction is computed and found to be

$$\mathcal{B}(B_s^0 \rightarrow \eta' \phi) = (-0.18_{-0.36}^{+0.47}(\text{stat}) \pm 0.10(\text{syst})) \times 10^{-6}.$$

Using the likelihood integration method described above, the obtained limit is

$$\mathcal{B}(B_s^0 \rightarrow \eta' \phi) < 0.82 \text{ (1.01)} \times 10^{-6} \quad \text{at 90\% (95\%) CL.}$$

This is the first upper limit set on the $B_s^0 \rightarrow \eta' \phi$ branching fraction. This result favours the lower end of the range of predictions for this branching fraction. Comparisons with theoretical expectations for the different models will be discussed in the conclusions of this work.

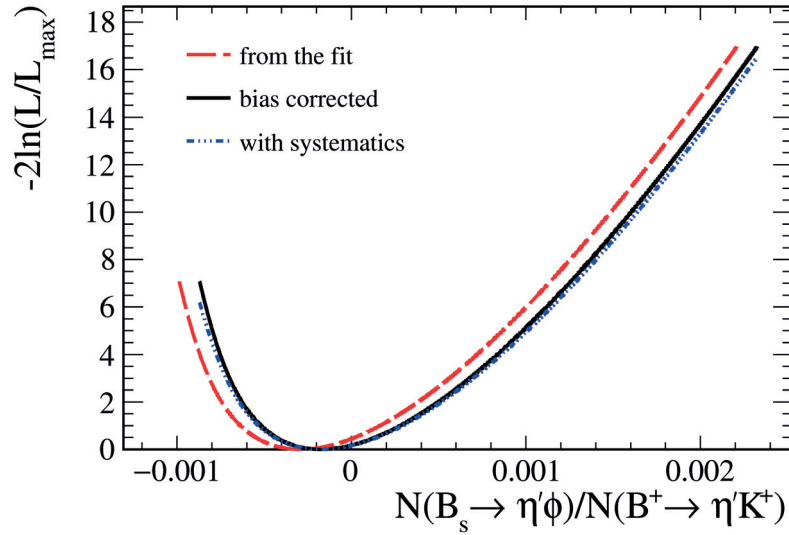


Figure 4.17 – $-2\ln(\mathcal{L}/\mathcal{L}_{\max})$ as a function of the yield ratio as obtained from the fit (red dashed), after correction for the fit bias (black solid), and accounting for systematic uncertainties (blue dot-dot-dashed).

5 Prospects for $B \rightarrow \phi X$ and $B \rightarrow \eta' X$ modes

As discussed in Chapter 1, the charmless B decays into light PV, VV or PP resonances are good probes to test the SM and study CP violation. However most of them have the disadvantage of being difficult to detect, either because their branching fraction is very small ($10^{-8} - 10^{-6}$) or because the reconstruction efficiency is low. The latter reason applies for example to the $B_s^0 \rightarrow \eta' \eta'$ decay, for which the inefficient photon reconstruction implies a modest detected yield despite the large branching fraction relative to other charmless modes, e.g. $B_s^0 \rightarrow \phi \phi$. While CP violation in $B_s^0 \rightarrow \phi \phi$ has been explored already, a first measurement of CP violation in $B_s^0 \rightarrow \eta' \eta'$ decays will necessitate more data than collected during Run 1. The addition of Run 2 data is therefore crucial to increase the statistics.

The primary goal of this chapter is to present a general quantitative picture of the possibilities for studying some of the $B \rightarrow \phi X$ and $B \rightarrow \eta' X$ decays at the end of Run 2 and beyond. In particular, we would like to examine the prospects for observing the rare $B^+ \rightarrow \phi \pi^+$ mode, for observing the $B_s^0 \rightarrow \eta' \phi$ mode, and for studying the already observed $B_s^0 \rightarrow \eta' \eta'$ decay. In order to predict future signal yields for the decays of interest, we rely on the two normalisation modes $B^+ \rightarrow \eta' K^+$ and $B^+ \rightarrow \phi K^+$, which have large yields and well known branching fractions.

The number of produced b hadrons of any species is proportional to both the integrated luminosity L and the $b\bar{b}$ production cross-section $\sigma_{b\bar{b}}$. The latter is known to be roughly proportional to the centre-of-mass energy of the pp collision, so is almost doubling from Run 1 at $\sqrt{s} = 7 - 8$ TeV to Run 2 at $\sqrt{s} = 13$ TeV. As a result the yield Y of any $B_{(s)}$ signal is expected to be proportional to $L \times \sqrt{s} \times \epsilon$, where ϵ is the reconstruction and selection efficiency. In other words, for decays modes where a yield Y can be measured, the quantity

$$Z = \frac{Y}{L \times \sqrt{s}}, \quad (5.1)$$

when compared between the different data-taking years, can give a useful indication of the actual evolution of the overall efficiency, while the quantity

$$W = \frac{Z}{\epsilon} = \frac{Y}{L \times \sqrt{s} \times \epsilon}, \quad (5.2)$$

Table 5.1 – Samples of fully-simulated events used in the prospect studies.

Decay chain	Year	(\sqrt{s})	Number of events
$B^+ \rightarrow \phi K^+, \phi \rightarrow K^+ K^-$	2011	7 TeV	0.27×10^6
$B^+ \rightarrow \phi K^+, \phi \rightarrow K^+ K^-$	2012	8 TeV	0.51×10^6
$B^+ \rightarrow \phi K^+, \phi \rightarrow K^+ K^-$	2015	13 TeV	0.21×10^6
$B^+ \rightarrow \phi K^+, \phi \rightarrow K^+ K^-$	2016	13 TeV	0.42×10^6
$B^+ \rightarrow \phi \pi^+, \phi \rightarrow K^+ K^-$	2011	7 TeV	0.27×10^6
$B^+ \rightarrow \phi \pi^+, \phi \rightarrow K^+ K^-$	2012	8 TeV	0.51×10^6
$B^+ \rightarrow \phi \pi^+, \phi \rightarrow K^+ K^-$	2015	13 TeV	0.19×10^6
$B^+ \rightarrow \phi \pi^+, \phi \rightarrow K^+ K^-$	2016	13 TeV	0.44×10^6
$B^+ \rightarrow \eta' K^+, \eta' \rightarrow \rho^0 \gamma, \rho^0 \rightarrow \pi^+ \pi^-$	2015	13 TeV	0.25×10^6
$B^+ \rightarrow \eta' K^+, \eta' \rightarrow \rho^0 \gamma, \rho^0 \rightarrow \pi^+ \pi^-$	2016	13 TeV	0.50×10^6
$B_s^0 \rightarrow \eta' \phi, \eta' \rightarrow \rho^0 \gamma, \rho^0 \rightarrow \pi^+ \pi^-, \phi \rightarrow K^+ K^-$	2015	13 TeV	0.25×10^6
$B_s^0 \rightarrow \eta' \phi, \eta' \rightarrow \rho^0 \gamma, \rho^0 \rightarrow \pi^+ \pi^-, \phi \rightarrow K^+ K^-$	2016	13 TeV	0.50×10^6
$B_s^0 \rightarrow \eta' \eta', \eta' \rightarrow \rho^0 \gamma, \rho^0 \rightarrow \pi^+ \pi^-$	2015	13 TeV	0.25×10^6
$B_s^0 \rightarrow \eta' \eta', \eta' \rightarrow \rho^0 \gamma, \rho^0 \rightarrow \pi^+ \pi^-$	2016	13 TeV	0.50×10^6

where ϵ is the MC estimate of the overall efficiency, is expected to be a constant, i.e. to take the same value when computed for different data-taking years. A secondary goal of this chapter is to investigate these Z and W quantities for $B^+ \rightarrow \eta' K^+$ and $B^+ \rightarrow \phi K^+$ decays to assess the improvement in efficiency from Run 1 to Run 2, as well as the reliability of the MC estimates of the efficiency.

5.1 Simulation

MC samples are needed to reproduce and optimise the selection requirements used in the data. Simulated samples are produced for the $B^+ \rightarrow \phi K^+$, $B^+ \rightarrow \phi \pi^+$, $B^+ \rightarrow \eta' K^+$, $B_s^0 \rightarrow \phi \eta'$ and $B_s^0 \rightarrow \eta' \eta'$ decays, using the four different data-taking conditions, corresponding to the years 2011, 2012, 2015 and 2016. The model used to generate these modes forces the particle to decay in the final state of interest. All the final state tracks are required to be within the LHCb acceptance. For the $B_s^0 \rightarrow \eta' \phi$ and $B^+ \rightarrow \eta' K^+$ decays, the MC samples emulating Run 1 conditions are the ones already presented in Sec. 3.2. Table 5.1 reports all the specifications for each of the MC samples used in the studies.

5.2 Projection for $B^+ \rightarrow \phi h^+$ modes

The $B^+ \rightarrow \phi K^+$ decay, detected in LHCb with a large yield, has been used as normalisation mode in the search of the rare $B^+ \rightarrow \phi \pi^+$ decay using only 2011 data, for which an upper limit of 1.5×10^{-7} has been set at 90% confidence level [86]. In the QCD factorisation approach, the $B^+ \rightarrow \phi \pi^+$ branching fraction is predicted to be in the range $(5 - 10) \times 10^{-9}$ [27], neglecting the contribution from $\omega - \phi$ mixing, which could enhance the branching fraction up to 0.6×10^{-7}

Table 5.2 – Preselection requirements applied on the B candidates passing the stripping selection to form $B^+ \rightarrow \phi K^+$ and $B^+ \rightarrow \phi \pi^+$ candidates.

Observable		Requirement
$\phi \rightarrow K^+ K^-$ meson		
– vertex quality	χ^2/ndf	< 9
– mass	m_{KK}	$\in [1.00, 1.05] \text{ GeV}/c^2$
– transverse momentum	p_T	$> 2.0 \text{ GeV}/c$
B^+ meson		
– transverse momentum	p_T	$> 1.5 \text{ GeV}/c$
– vertex quality	χ^2/ndf	< 9
– mass	m_B	$\in [5.0, 5.5] \text{ GeV}/c^2$

depending on the value of the mixing angle [87, 88].

5.2.1 $B^+ \rightarrow \phi h^+$ selection

We have developed a new selection strategy, optimised for the $B^+ \rightarrow \phi \pi^+$ decay mode. The same selection is applied to select $B^+ \rightarrow \phi K^+$ candidates, except for the PID requirement on the bachelor hadron (π^+ or K^+) accompanying the ϕ meson in the final state. After a first-stage filtering by the stripping algorithm `B2CharmlessQ2B3piSelectionLine`, the decay chain is fully reconstructed, assigning the desired mass to the charged particles (either pion or kaon). Several fiducial cuts, presented in Table 5.2, are applied to reduce the background, keeping the signal efficiency high.

The trigger requirements are listed in Table 5.3. The four-body topological line is not used (because there are only three particles in the final state) and is replaced, for Run 1 datasets, with two lines, `Hlt2IncPhi_TOS` and `Hlt2IncPhiSidebands_TOS`, which select ϕ candidates within two mass windows, a tight and a wider one. The trigger requirements used for the Run 2 datasets remain very similar at L0 and HLT2 level (for which only fine tuning of the lines is performed), except for the `Hlt2IncPhiSidebands_TOS` line which is not used. At HLT1 level, the `TrackAllL0_TOS` line is replaced with a new line using multivariate algorithms, as presented in Sec. 2.5.3. Due to a trigger requirement applied at the stripping level, it is not possible, at present, to benefit from other HLT1 lines, for example new lines selecting ϕ mesons more efficiently. This requirement has been modified in a new version of the stripping algorithm, which will allow a more efficient preselection in the full Run 2 dataset as soon as the new algorithm is applied on data.

BDT selection

A multivariate selection is applied to the reconstructed candidates, in order to reduce the contamination from uninteresting events and improve the signal significance. A single BDT

Table 5.3 – List of trigger lines used for the $B^+ \rightarrow \phi h^+$ preselection in Run 1 and Run 2 datasets.

L0	HLT1	HLT2
<u>Run 1:</u>		
Hadron_TOS	TrackAllL0_TOS	Topo2BodyBBBDT_TOS
Hadron_TIS		Topo3BodyBBBDT_TOS
Photon_TIS		IncPhi_TOS
Muon_TIS		IncPhiSidebands_TOS
Electron_TIS		
<u>Run 2:</u>		
Hadron_TOS	TrackMVA_TOS	Topo2Body_TOS
Hadron_TIS		Topo3Body_TOS
Muon_TIS		PhiIncPhi_TOS
Photon_TIS		
Electron_TIS		

algorithm is built for the two decays, since no PID variable is included as input and the two modes present the same topology. The BDT is optimised for the $B^+ \rightarrow \phi\pi^+$ mode, using fully-simulated signal events and Run 1 data events falling in the high-mass sideband, defined as $5460 < m_{KK\pi} < 5800 \text{ MeV}/c^2$. The decision to use background events from the high-mass sideband only is motivated by the fact that the BDT is designed to suppress the combinatorial background while significant partially reconstructed contributions are expected in the low-mass sideband. Since no PID requirement is applied at this stage of the analysis, the statistics in the high-mass sideband is sufficient to train and test the BDT algorithm. Figure 5.1 shows the distributions of the seven BDT input variables, which are defined in Table 5.4. The distributions of the output of the BDT algorithm for signal and combinatorial background are compared in Fig. 5.2 and show good separation power. The value of the cut on the BDT output variable that maximises the figure of merit of Eq. 3.2 [74] is found to be 0.

PID requirement

The PID requirement is crucial in this selection, and needs to be kept under control to avoid a large mis-identification rate in the $B^+ \rightarrow \phi\pi^+$ sample. For both the $B^+ \rightarrow \phi\pi^+$ and $B^+ \rightarrow \phi K^+$ candidates, the ProbNN_K variable is required to be greater than 0.1 for each of the two kaons forming the ϕ candidates. This cut is useful to reject fake ϕ mesons and, in particular, a partially reconstructed background where a charged pion is misidentified as a kaon, appearing in the high-mass sideband and peaking (with a wide bump) at $\sim 5420 \text{ MeV}/c^2$. A PID requirement is also applied on the bachelor particle h^+ of the $B^+ \rightarrow \phi h^+$ candidates in order to reduce the abundant contamination from the normalisation mode in the sample of $B^+ \rightarrow \phi\pi^+$ candidates. A combination of the two variables ProbNN_K and ProbNN_π is used: the difference $\text{ProbNN}_\pi - \text{ProbNN}_K$ is required to be greater than 0.3 for the $B^+ \rightarrow \phi\pi^+$ candidates and smaller

5.2. Projection for $B^+ \rightarrow \phi h^+$ modes

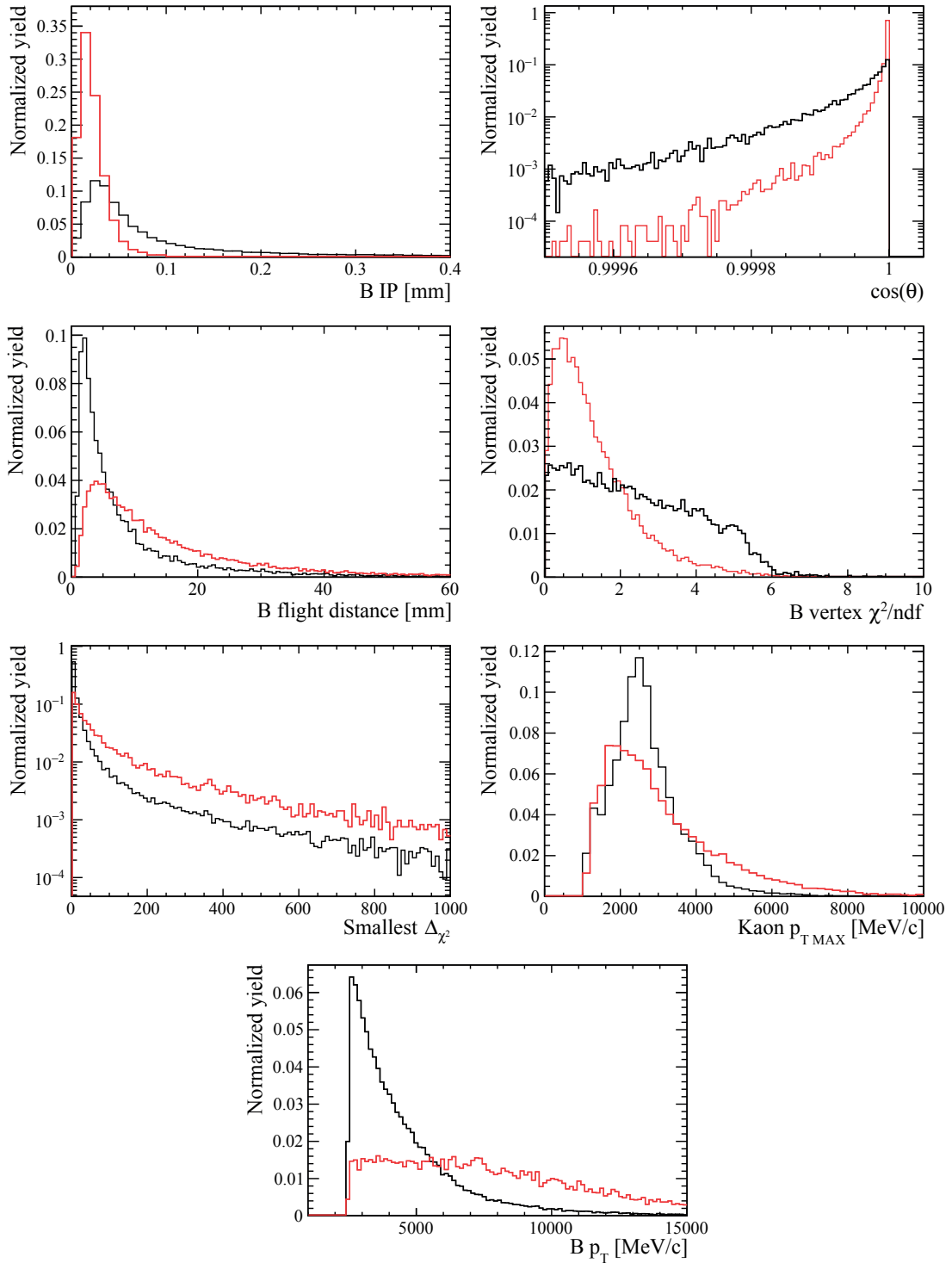


Figure 5.1 – Distributions of the seven BDT input variables defined in Table 5.4, for fully-simulated $B^+ \rightarrow \phi\pi^+$ signal decays (red) and high-mass combinatorial background in 2012 data (black).

Table 5.4 – Definition of the seven variables used as input to the $B^+ \rightarrow \phi h^+$ multivariate selection. The notation PV refers to the reconstructed primary vertex with respect to which the B^+ candidate has the smallest impact parameter χ^2 .

Variables related to geometry and vertexing:

1. B^+ impact parameter with respect to the PV
2. Cosine of the angle between the B^+ momentum direction and the vector from the PV to the B^+ decay vertex
3. Distance of flight of the B^+ candidate
4. χ^2/ndf of the B^+ vertex
5. Smallest increase in χ^2 when adding one track to the B^+ vertex

Kinematic variables:

6. Highest transverse momentum of the two ϕ daughters
7. Transverse momentum of the B^+ candidate

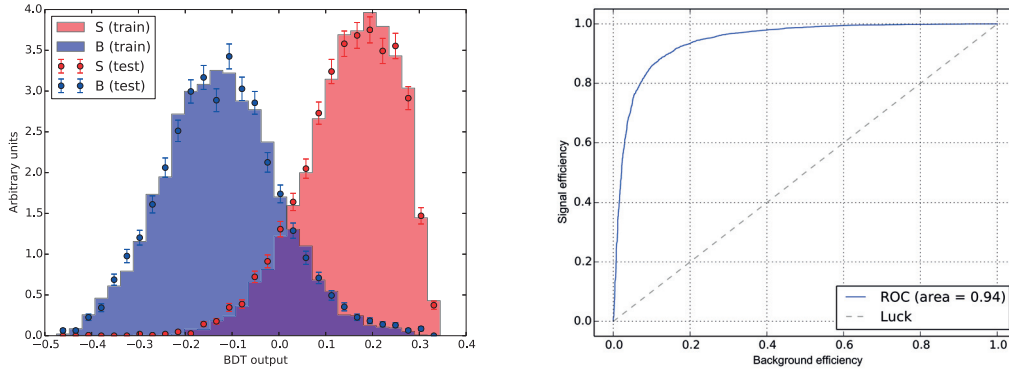


Figure 5.2 – Left: distributions of the BDT output for simulated $B^+ \rightarrow \phi\pi^+$ signal events (red) and the 2011 – 2012 data candidates in the high-mass sideband (blue). Right: signal efficiency for a given background efficiency when a requirement on the BDT output is applied.

than 0.3 for the $B^+ \rightarrow \phi K^+$ candidates.

5.2.2 $B^+ \rightarrow \phi K^+$ observed yield

The $B^+ \rightarrow \phi K^+$ yield is obtained from a two-dimensional fit of the data candidates passing the selection criteria. The two fitted variables are the reconstructed ϕ and B^+ masses, denoted m_{KK} and m_{KKK} . They are treated as independent and the joint PDF for each component is the product of two one-dimensional PDFs. The fit model, taken from Ref. [82], includes six components:

- The $B^+ \rightarrow \phi K^+$ signal yield is described in the m_{KKK} dimension with a double-tail CB function, defined in Sec. 4.2. A relativistic Breit-Wigner function convolved with a

Gaussian is used to describe the ϕ signal:

$$\begin{aligned}
 \text{BWG}(m_{KK}; m_\phi, \Gamma_\phi, \sigma_\phi) &= \int_{-\infty}^{\infty} \text{BW}(m'_{KK}; m_\phi, \Gamma_\phi) \text{G}(m_{KK} - m'_{KK}; \sigma_\phi) dm'_{KK}, \\
 \text{BW}(m_{KK}; m_\phi, \Gamma_\phi) &= N_{\text{BW}} \frac{m_{KK} m_\phi \Gamma(m_{KK}, m_\phi, \Gamma_\phi)}{(m_{KK}^2 - m_\phi^2)^2 + m_\phi^2 \Gamma(m_{KK}, m_\phi, \Gamma_\phi)^2}, \\
 \Gamma(m_{KK}, m_\phi, \Gamma_\phi) &= \Gamma_\phi \left(\frac{q(m_{KK})}{q(m_\phi)} \right)^{2L+1} \left(\frac{m_\phi}{m_{KK}} \right), \\
 q(m_{KK}) &= \frac{\sqrt{(m_{KK}^2 - (m_{K^+} + m_{K^-})^2)(m_{KK}^2 - (m_{K^+} - m_{K^-})^2)}}{2m_{KK}}, \\
 &= \sqrt{\frac{m_{KK}^2}{4} - m_K^2}.
 \end{aligned} \tag{5.3}$$

The three parameters are the mass resolution σ_ϕ , the ϕ mass m_ϕ and width Γ_ϕ ; N_{BW} is a normalisation factor which depends on the mass and width of the ϕ meson. The function $q(m_{KK})$ represents the kaon momentum in the mother rest frame, $L = 1$ is the relative angular momentum between the two kaons, and m_K is the kaon mass. Because of the correlation between the resolution and the ϕ width, the latter is fixed to its known value of $4.26 \text{ MeV}/c^2$ [13].

- The background from non-resonant $B^+ \rightarrow K^+ K^- K^+$ decays is described with a double-tail CB function and a linear function in the m_{KKK} and m_{KK} dimension, respectively.
- The partially-reconstructed background is described in m_{KKK} with an Argus function convolved with a Gaussian function:

$$\begin{aligned}
 \text{ARG}(m_{KKK}; m_0, p, c, \sigma) &= \int_{-\infty}^{\infty} f_{\text{ARG}}(m'; m_0, p, c) \text{G}(m_{KKK} - m'; \sigma) dm', \\
 f_{\text{ARG}}(m_{KKK}; m_0, p, c) &= N_{\text{ARG}} m_{KKK} \left(1 - \left(\frac{m_{KKK}}{m_0} \right)^2 \right)^p \exp \left(c \left(1 - \left(\frac{m_{KKK}}{m_0} \right)^2 \right) \right), \\
 \text{G}(m_{KKK} - m'; \sigma) &= \frac{1}{\sqrt{2\pi}\sigma} \exp \left(-\frac{1}{2} \left(\frac{m_{KKK} - m'}{\sigma} \right)^2 \right),
 \end{aligned} \tag{5.4}$$

where N_{ARG} is a normalisation factor, p is a fixed parameter, m_0 is the end-point of the partially-reconstructed distribution and c is a free parameter. A linear function or a relativistic Breit-Wigner function convolved with a Gaussian is used to describe the $K^+ K^-$ invariant mass, depending on the absence or presence of a real ϕ meson.

- The combinatorial background is described with a linear function in m_{KKK} and a linear function or a relativistic Breit-Wigner function convolved with a Gaussian in m_{KK} , depending on the absence or presence of a real ϕ meson.

The tail parameters of the CB functions are obtained from a fit on simulated events and are fixed in the fit on real data.

Four independent fits are performed for the four different datasets collected in the years 2011, 2012, 2015 and 2016. Table 5.5 shows the fit results, while Fig. 5.3 shows the mass distributions with the results of the fit superimposed. Despite the fact that the used selection

Chapter 5. Prospects for $B \rightarrow \phi X$ and $B \rightarrow \eta' X$ modes

Table 5.5 – $B^+ \rightarrow \phi K^+$ fit results for the four different datasets. The first six parameters are the signal and background yields.

Parameter	2011	2012	2015	2016
$B^+ \rightarrow \phi K^+$ signal yield	3938 ± 80	9776 ± 127	2712 ± 68	15315 ± 161
Non-resonant $B^+ \rightarrow K^+ K^- K^+$	879 ± 56	1898 ± 85	551 ± 47	3256 ± 119
Part. rec. $b \rightarrow \phi X$	852 ± 59	1717 ± 96	320 ± 54	2628 ± 122
Part. rec. without ϕ	320 ± 56	731 ± 90	301 ± 57	1419 ± 121
Combinatorial with true ϕ	89 ± 73	831 ± 127	395 ± 76	1129 ± 164
Combinatorial without ϕ	584 ± 73	1585 ± 119	600 ± 74	3353 ± 163
B^+ mass [MeV/ c^2]	5284.6 ± 0.3	5284.0 ± 0.2	5281.1 ± 0.4	5279.7 ± 0.2
B^+ mass resolution [MeV/ c^2]	19.3 ± 0.3	18.9 ± 0.2	18.9 ± 0.4	19.2 ± 0.2
ϕ mass [MeV/ c^2]	1019.76 ± 0.05	1019.75 ± 0.03	1019.79 ± 0.06	1019.73 ± 0.03
ϕ mass resolution [MeV/ c^2]	1.01 ± 0.11	0.91 ± 0.07	1.02 ± 0.12	0.98 ± 0.05
Argus c parameter	-12.3 ± 2.4	-9.0 ± 1.8	-7.3 ± 4.0	-8.2 ± 1.5

is not optimised for the Run 2 data, an improved signal-to-noise ratio is observed for 2016 sample with respect to Run 1 data. This is not the case for the 2015 data sample. However the level of noise can be further reduced in the future with a dedicated selection optimisation. The obtained yields, together with the selection efficiencies are compared in the first part of Table 5.8. The observed yield in 2016 data is more than a factor two larger than that in 2012 data despite the lower integrated luminosity, thanks not only to the increase in production cross-section but also to an improved detection efficiency. To ease the comparison between the different years of data-taking the quantity Z defined in Eq. 5.1 is also reported. This value gives information on the gain in efficiency directly observed in data. The ratio $Z/Z(2012)$ is observed to be larger than one for the two Run 2 datasets and smaller for 2011 data. This corresponds to the trend observed for the Run 2 selection efficiency in simulation, but not with the estimate for 2011. The consistency between the different years can be checked by computing the quantity W defined in Eq. 5.2. This quantity shows variations, indicating a discrepancy between data and MC, resulting in a wrong estimate of the absolute signal efficiency. This trend is even more pronounced for the mode with a photon as will be shown below.

5.2.3 $B^+ \rightarrow \phi \pi^+$ expected yield

The efficiency of the selection requirements described above are evaluated both for the $B^+ \rightarrow \phi \pi^+$ and the $B^+ \rightarrow \phi K^+$ decay modes using MC simulated signal samples for the four different data-taking conditions (2011, 2012, 2015, 2016). The values are presented in Table 5.8. For each year separately, the expected $B^+ \rightarrow \phi \pi^+$ yield is computed using the formula

$$N_{B \rightarrow \phi \pi} = N_{B \rightarrow \phi K} \times \frac{\mathcal{B}(B^+ \rightarrow \phi \pi^+)}{\mathcal{B}(B^+ \rightarrow \phi K^+)} \times \frac{\varepsilon_{B \rightarrow \phi \pi}}{\varepsilon_{B \rightarrow \phi K}}, \quad (5.5)$$

5.2. Projection for $B^+ \rightarrow \phi h^+$ modes

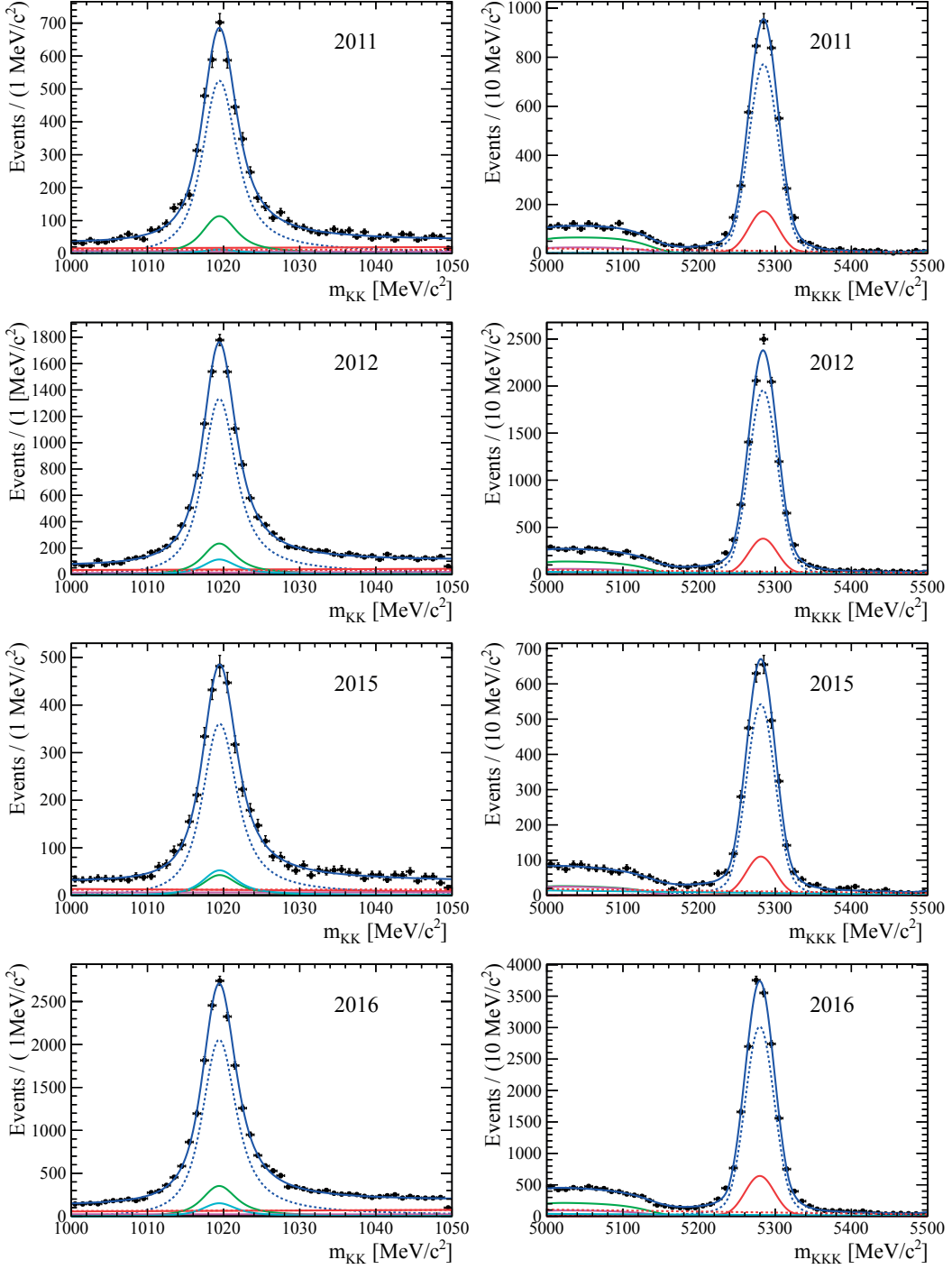


Figure 5.3 – $K^+ K^-$ (left) and $K^+ K^- K^+$ (right) mass distributions for the $B^+ \rightarrow \phi K^+$ candidates selected in the 2011, 2012, 2015 and 2016 datasets (from top to bottom). The solid blue curve represents the result of the two-dimensional fit described in the text, with the following components: $B^+ \rightarrow \phi K^+$ signal (blue dashed), non-resonant $B^+ \rightarrow K^+ K^- K^+$ (red), partially reconstructed $b \rightarrow \phi X$ background (green), partially reconstructed without a true ϕ (magenta), combinatorial background (red dashed) and combinatorial background with real ϕ (light blue). Some of the components are barely visible because the corresponding yields are small.

where $N_{B \rightarrow \phi K}$ is the $B^+ \rightarrow \phi K^+$ yield observed in data, $\frac{\epsilon_{B \rightarrow \phi \pi}}{\epsilon_{B \rightarrow \phi K}}$ is the ratio of efficiencies determined from simulation and $\mathcal{B}(B^+ \rightarrow \phi K^+) = (8.8 \pm 0.7) \times 10^{-6}$ [13] is the branching fraction of the $B^+ \rightarrow \phi K^+$ decay. Table 5.8 shows the $B^+ \rightarrow \phi \pi^+$ expected yields assuming arbitrarily $\mathcal{B}(B^+ \rightarrow \phi \pi^+) = 1 \times 10^{-8}$. The higher efficiency in the Run 2 dataset for the preselection and trigger selection is compensated by a lower PID efficiency, resulting in a almost constant efficiency across the different data-taking conditions. Therefore the expected yield mostly gains from the increased production cross-section at higher energy.

5.3 Projection for $B_{(s)} \rightarrow \eta' X$ modes

We use here the $B^+ \rightarrow \eta' K^+$ decay as reference to predict the yields for two modes of the $B_{(s)} \rightarrow \eta' X$ family. We focus on the prospects for the $B_s^0 \rightarrow \eta' \phi$ mode, which is the main topic of this thesis, and the $B_s^0 \rightarrow \eta' \eta'$ mode, already observed by LHCb [33], but for which only a relatively small yield could be measured so far.

5.3.1 $B^+ \rightarrow \eta' K^+$ observed yield

The selection strategy for the $B^+ \rightarrow \eta' K^+$ decay, developed for Run 1 and presented in Chapter 3, is applied to Run 2 data. The fit model used to extract the signal yield is the same as presented in Sec. 4.3.2. The obtained results for 2015 and 2016 data are presented in Table 5.6 and in Fig. 5.4. They can be compared with the results presented in Table 4.3 and Fig. 4.3 for 2011 and 2012 data. Summing up the four different datasets, a very large signal yield is obtained close to 30k events. The level of background with respect to the signal yield in Run 2 is approximately the same as in Run 1, although with a small improvement. As shown by the quantity Z displayed in Table 5.8, an improvement close to 50% in efficiency occurs between 2011 and Run 2. However, this improvement is not reflected in the MC estimate of the efficiencies. For instance, the lower efficiency computed for 2012 with respect to 2011 simulated events, is not compatible with the larger yield measured in data with respect to 2011 data. This trend is a hint of a discrepancy between data and MC simulation and has been carefully studied with Run 1 data.

In particular a comparison between the expected and the fitted events for the $B^+ \rightarrow \eta' K^+$ channel is performed. The study has been performed before applying the BDT selection requirements.

Table 5.7 shows the expected $B^+ \rightarrow \eta' K^+$ yields before applying the BDT selection. The yield can be computed from the integrated luminosity, $b\bar{b}$ production cross-section, fragmentation fraction, visible branching fraction and preselection efficiency (see Eq. 3.8), both for the 2011 and 2012 datasets, and then compared to the observed yields. The latter are obtained by one-dimensional fit to the $B^+ \rightarrow \eta' K^+$ mass distribution shown in Fig. 3.4, for which a cut on the $\pi^+ \pi^- \gamma$ mass is applied to reduce the background. The Monte Carlo efficiency for the tight $\pi^+ \pi^- \gamma$ mass requirement is taken into account. The expected yield is larger than the observed one by a factor 2.3 ± 0.5 (1.8 ± 0.2) for the 2011 (2012) conditions. No clear explanation for this

5.3. Projection for $B_{(s)} \rightarrow \eta' X$ modes

Table 5.6 – Results of the simultaneous fit of the $B^+ \rightarrow \eta' K^+$ candidates in the 2015 and 2016 datasets with different masses and resolutions parameters for the 2015 and 2016 conditions.

Parameter			Value and uncertainty	
			2015	2016
B^+ mass	m_B	[MeV/ c^2]	5279.0 ± 0.6	5278.7 ± 0.2
B^+ mass resolution (2016)	σ_B	[MeV/ c^2]	23.4 ± 0.6	22.0 ± 0.2
η' mass (2016)	$m_{\eta'}$	[MeV/ c^2]	954.5 ± 0.4	954.5 ± 0.2
η' mass resolution (2016)	$\sigma_{\eta'}$	[MeV/ c^2]	12.8 ± 0.3	13.0 ± 0.1
$B^+ \rightarrow \eta' K^+$ signal yield			2653 ± 63	14745 ± 148
Combinatorial background yield with true η'			156 ± 43	724 ± 107
Combinatorial background yield			2638 ± 70	14043 ± 166

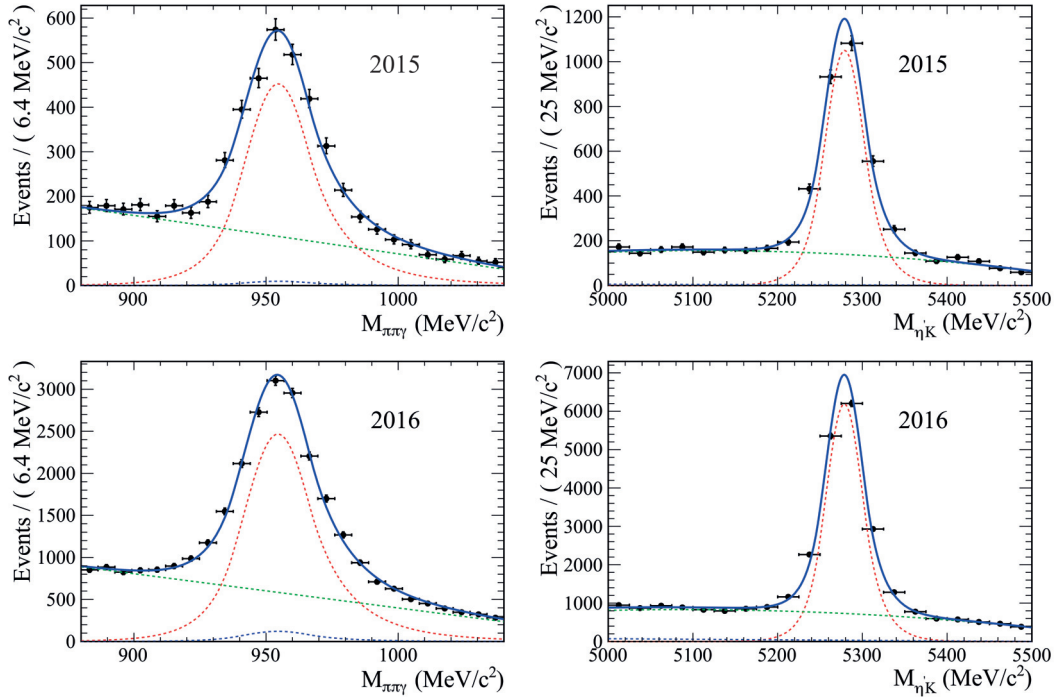


Figure 5.4 – $\pi^+ \pi^- \gamma$ (left) and $\eta' K^+$ (right) mass distributions of the $B^+ \rightarrow \eta' K^+$ candidates selected in 2015 (top) and 2016 (bottom) datasets. The superimposed fit results are indicated with the solid blue curves and the following components: $B^+ \rightarrow \eta' K^+$ signal (red dashed), combinatorial background (green dashed) and combinatorial background with real η' (blue dashed).

Table 5.7 – Calculation of the number of $B^+ \rightarrow \eta' K^+$ expected in Run 1 as obtained from Monte Carlo after preselection and comparison with the corresponding $B^+ \rightarrow \eta' K^+$ yield observed in data.

Quantity	Symbol	2011	2012
Integrated luminosity	\mathcal{L}	$1.017 \pm 0.036 \text{ fb}^{-1}$	$2.057 \pm 0.072 \text{ fb}^{-1}$
$b\bar{b}$ production cross-section	$\sigma(pp \rightarrow b\bar{b}X)$	$284 \pm 53 \mu\text{b}$ [89]	$298 \pm 36 \mu\text{b}$ [90]
Number of B^\pm per $b\bar{b}$	$2 \times f_u$	$2 \times (40.5 \pm 0.6)\%$ [13]	
Branching fraction	$\mathcal{B}(B^+ \rightarrow \eta' K^+)$	$(70.6 \pm 2.5) \times 10^{-6}$ [13]	
Sub-branching fraction	$\mathcal{B}(\eta' \rightarrow \pi^+ \pi^- \gamma)$	$(29.1 \pm 0.5)\%$ [13]	
Preselection efficiency	ϵ^{preSEL}	$(0.2353 \pm 0.0029)\%$	$(0.2122 \pm 0.0018)\%$
Expected yield (product of above)	$N_{\text{exp}}^{\text{preSEL}}$	$(11.3 \pm 2.2)\text{k}$	$(21.6 \pm 2.9)\text{k}$
Fitted yield (Fig. 3.4)	$N_{\text{fit}}^{\text{preSEL}}$	4151 ± 135	9987 ± 232
Efficiency of tight $m_{\pi\pi\gamma}$ requirement	$\epsilon^{\eta'}$	$(86.06 \pm 0.49)\%$	$(83.72 \pm 0.38)\%$
Yield in data	$N^{\text{preSEL}} = N_{\text{fit}}^{\text{preSEL}} / \epsilon^{\eta'}$	4823 ± 159	11929 ± 282
Ratio expected/observed	$N_{\text{exp}}^{\text{preSEL}} / N^{\text{preSEL}}$	2.3 ± 0.5	1.8 ± 0.2

data-MC discrepancy is found. Similar discrepancies were already encountered in a previous analysis [91], where the factors were found to be 1.63 ± 0.34 and 1.86 ± 0.37 (1.44 ± 0.22 and 1.40 ± 0.19) for the $B^+ \rightarrow \phi K^+$ and $B^+ \rightarrow \eta' K^+$ decay modes, respectively.

This discrepancy implies a difference in the values of W . However, the computation of the expected yields for the other modes is not affected, since only ratios per year are considered.

5.3.2 $B_s^0 \rightarrow \eta' \phi$ expected yield

As for the $B^+ \rightarrow \eta' K^+$, the same requirements used in Run 1 analysis are applied to Run 2 simulated signal events. The selection efficiencies are presented in Table 5.8. An increase observed in the Run 2 dataset is due to a more efficient trigger. The expected number of events for each dataset condition is obtained using Eq. 3.9. An arbitrary branching fraction of $\mathcal{B}(B_s^0 \rightarrow \eta' \phi) = 1 \times 10^{-6}$ is assumed, but values down to $\mathcal{B}(B_s^0 \rightarrow \eta' \phi) = 0.05 \times 10^{-6}$ are predicted by some theoretical models, as discussed in Chapter 1. However, taking into account the upper limit set in this thesis and therefore the low branching fraction expected, the predicted number events for the data collected so far remains small.

5.3.3 $B_s^0 \rightarrow \eta' \eta'$ observed and expected yield

The requirements used to select the $B_s^0 \rightarrow \eta' \eta'$ candidates, for which the resulting efficiencies are reported in Table 5.8, consists of square cuts for the most relevant kinematical and topological variables. The selection strategy is taken from Ref. [82]. An optimised selection is out of our scope, but for a future analysis a multivariate selection should be considered to improve the signal selection. The number of events expected for each of the different data

taking period is computed as

$$N_{B_s \rightarrow \eta' \eta'} = N_{B \rightarrow \eta' K^+} \times \frac{f_s}{f_u} \times \frac{\mathcal{B}(B_s^0 \rightarrow \eta' \eta')}{\mathcal{B}(B^+ \rightarrow \eta' K^+)} \times \mathcal{B}(\eta' \rightarrow \pi^+ \pi^- \gamma) \times \frac{\varepsilon_{B_s \rightarrow \eta' \eta'}}{\varepsilon_{B \rightarrow \eta' K}}, \quad (5.6)$$

where $\mathcal{B}(B_s^0 \rightarrow \eta' \eta') = (3.31 \pm 0.64(\text{stat}) \pm 0.28(\text{syst}) \pm 0.12(\text{norm})) \times 10^{-5}$ as measured in Ref. [82] and $\mathcal{B}(\eta' \rightarrow \pi^+ \pi^- \gamma) = 0.291 \pm 0.005$ [13]. Results are shown in Table 5.8. The increase in efficiency observed for Run 2 simulated signal events is attributed to larger preselection and trigger efficiencies. In particular the improvement in the preselection with respect to the previous analysis is due to the use of a more recent and efficient stripping algorithm and to an improved tuning of the CL_γ variable resulting in a more effective observable with a better signal-to-noise separation. This is promising in view of optimising the selection efficiency for this channel.

5.4 Discussion

The observed yields of $B^+ \rightarrow \eta' K^+$ and $B^+ \rightarrow \phi K^+$ decays and the expected yields for the rare modes are presented above. For the two normalisation channels large yields are measured, thanks not only to the increase of the production cross-section but also to an improved efficiency, with respect to Run 1. The predictions for the yields of the yet unobserved $B_s^0 \rightarrow \eta' \phi$ and $B^+ \rightarrow \phi \pi^+$ decays suggest that at least the full Run 2 dataset will be needed to aim at an observation of these modes, bearing in mind that the predictions for the branching fractions vary within two orders of magnitude.

Assuming the same efficiency as for the 2016 data for the rest of the Run 2 data-taking, and assuming that another 3 fb^{-1} will be collected, a factor 1.8 more events can be expected with respect to the 2016 predictions. The signal-to-noise ratio is expected to improve slightly, like for the normalisation modes in the comparison between Run 1 and Run 2. The extrapolation of the total number of events expected at the end of Run 2 (5 fb^{-1}) for each of the two modes is presented in Table 5.9. Regarding the already observed $B_s^0 \rightarrow \eta' \eta'$ decay, the number of collected events will be enough for a first measurement of the B_s^0 effective lifetime with this mode. Using as a reference the sensitivity of the recent $B_s^0 \rightarrow \mu^+ \mu^-$ effective lifetime measurement performed with 42 signal events [92], and assuming a central value of the $B_s^0 \rightarrow \eta' \eta'$ effective lifetime equal to the lifetime of the light B_s^0 mass eigenstate [13] decays, a statistical error of $\sim 0.13 \text{ ps}$ can be achieved with the full Run 2 statistics. On the other hand a flavour-tagged analysis will be out of reach, and the data collected with the upgraded detector [93] in Runs 3 and 4 ($\sim 50 \text{ fb}^{-1}$) will be needed (see Table 5.9 for the expected number of events). Despite an improvement in the tagging efficiency with respect to the algorithms used in the past (40% – 60% improvement) [94, 95], the statistical uncertainty on a $\phi_s^{s\bar{s}}$ measurement using the $B_s^0 \rightarrow \eta' \eta'$ sample collected by the end of Run 4 would not be competitive yet. As a comparison $7421 \pm 105 B_s^0 \rightarrow J/\psi \pi^+ \pi^-$ signal events with the CP-odd final state were needed to measure $\phi_s^{c\bar{c}s}$ with a statistical uncertainty of 0.17 rad [96]. A 300 fb^{-1} sample, which could be collected by ~ 2035 , in case of a Phase-2 upgrade of the detector (high-lumi LHC) [97] will be needed to

Chapter 5. Prospects for $B \rightarrow \phi X$ and $B \rightarrow \eta' X$ modes

Table 5.8 – Integrated luminosities L , centre-of-mass energies \sqrt{s} , observed or expected signal yields Y and MC selection efficiencies ϵ for the four different data-taking conditions and a few $B^+ \rightarrow h^+ X$ and $B_{(s)} \rightarrow \eta' X$ decay modes. For the normalisation modes, the quantities $Z = [Y/(L \times \sqrt{s})]$ and $W = [Y/(L \times \sqrt{s} \times \epsilon)]$ are quoted, normalised by their value in 2012 data. The uncertainty on the signal yields is only statistical and does not account for systematic effects. The quoted uncertainties are computed propagating the errors for all the quantities appearing, except for the centre-of-mass energy and the assumed branching fractions for $B_s^0 \rightarrow \eta' \phi$ and $B^+ \rightarrow \phi \pi^+$.

Integrated luminosity L (fb^{-1})	1.017 ± 0.036	2.057 ± 0.072	0.282 ± 0.011	1.710 ± 0.089
Centre-of-mass energy \sqrt{s} (TeV)	7	8	13	13
<u>$B^+ \rightarrow \phi K^+$ normalisation mode</u>				
Observed yield Y	3938 ± 80	9776 ± 127	2712 ± 68	15315 ± 161
Efficiency ϵ (10^{-6})	6894 ± 67	6480 ± 48	7860 ± 81	7798 ± 60
$Z/Z(2012)$	0.93 ± 0.05	1	1.24 ± 0.07	1.16 ± 0.07
$W/W(2012)$	0.87 ± 0.03	1	1.03 ± 0.05	0.96 ± 0.02
<u>$B^+ \rightarrow \phi \pi^+$ search mode</u>				
Efficiency ϵ (10^{-6})	6622 ± 66	5777 ± 44	6655 ± 74	6589 ± 50
Expected yield Y for $\mathcal{B} = 1 \times 10^{-8}$	4.3 ± 0.4	9.9 ± 0.8	2.6 ± 0.2	14.7 ± 1.2
<u>$B^+ \rightarrow \eta' K^+$ normalisation mode</u>				
Observed yield Y	3203 ± 67	7886 ± 108	2653 ± 63	14745 ± 148
Efficiency ϵ (10^{-6})	1502 ± 24	1275 ± 15	1596 ± 32	1631 ± 23
$Z/Z(2012)$	0.94 ± 0.05	1	1.51 ± 0.09	1.38 ± 0.09
$W/W(2012)$	0.80 ± 0.04	1	1.21 ± 0.08	1.08 ± 0.02
<u>$B_s^0 \rightarrow \eta' \phi$ search mode</u>				
Efficiency ϵ (10^{-6})	782 ± 16	711 ± 12	912 ± 25	925 ± 18
Expected yield Y for $\mathcal{B} = 1 \times 10^{-6}$	3.0 ± 0.2	7.9 ± 0.6	2.7 ± 0.2	15.0 ± 1.1
<u>$B_s^0 \rightarrow \eta' \eta'$ study mode</u>				
Observed yield Y [82]	36.4 ± 7.8	(full Run 1)	–	–
Efficiency ϵ (10^{-6})	130 ± 5	125 ± 4	273 ± 13	253 ± 9
Expected yield Y for $\mathcal{B} = 33.1 \times 10^{-6}$	9.8 ± 0.8	27.3 ± 2.2	16.0 ± 1.5	80.8 ± 6.7

Table 5.9 – Expected yields for the $B_s^0 \rightarrow \eta' \phi$, $B^+ \rightarrow \phi \pi^+$ and $B_s^0 \rightarrow \eta' \eta'$ decay modes assuming an integrated luminosity of 5 fb^{-1} (full Run 2), 50 fb^{-1} and 300 fb^{-1} . The same branching fractions as in Table 5.8 are assumed. The propagated uncertainties account for correlations.

Decay mode	Run 2 (5 fb^{-1})	Runs 3 & 4 (50 fb^{-1})	High-lumi (300 fb^{-1})
$B^+ \rightarrow \phi \pi^+$	43 ± 3	432 ± 35	2595 ± 210
$B_s^0 \rightarrow \eta' \phi$	44 ± 3	441 ± 32	2651 ± 195
$B_s^0 \rightarrow \eta' \eta'$	239 ± 20	2376 ± 198	14265 ± 1186

start to obtain a comparable $B_s^0 \rightarrow \eta'\eta'$ yield.

All the predictions for end of Run 2, Runs 3–4 and the high-lumi phase assume the same efficiency equal to the one computed for the 2016 data-taking conditions. While this assumption is realistic for the full Run 2 projections, it is quite pessimistic for the longer term projections. Indeed significant improvements are expected during and after the upgrade phase, where for instance the removal of the hardware trigger is expected to boost the efficiency of hadronic decay modes.

Conclusion

The work presented in this thesis focuses on a specific topic of the physics programme of the LHCb experiment: the study of charmless B decays.

Charmless B decays, proceeding predominantly through $b \rightarrow u$ and $b \rightarrow s$ transitions, are an interesting sector of the B physics field to test the Standard Model and look for new physics effects. Indeed the amplitude of the tree-level transition (proportional to V_{ub}) is small and therefore loop or higher-order diagrams can compete in strength. New particles can enter the loop diagrams and give a contribution to observables that can be measured precisely. Of particular interest are the B_s^0 charmless decays, which are still poorly known. Precise measurements of these decays are also important to constrain the large theoretical uncertainties that still affect the predictions of the branching fractions and CP violation observables.

Time-dependent CP violation measurements can be performed by studying the decays of the family $B_s^0 \rightarrow XY$, where X and Y are each either a η , η' or ϕ meson. Among these modes, mostly dominated by the $b \rightarrow s\bar{s}s$ gluonic penguin diagram, the $B_s^0 \rightarrow \phi\phi$ decay has been used to measure the CP-violating phase $\phi_s^{s\bar{s}s}$. Because of its vector-vector nature, the final state is a mixture of CP-even and CP-odd components, requiring an angular analysis, in addition to flavour tagging and proper time fitting. The analysis of Run 1 data yielded $\phi_s^{s\bar{s}s} = -0.17 \pm 0.15$ (stat) ± 0.03 (syst) [35]. No large CP violation is present either in $B_s^0 - \bar{B}_s^0$ mixing or in the $b \rightarrow s\bar{s}s$ decay amplitude, as expected in the Standard Model. In principle $\phi_s^{s\bar{s}s}$ can be measured with all the other decays of the family, without the need for an angular analysis, since the final state is a pure CP eigenstate. So far, among the other modes only the $B_s \rightarrow \eta'\eta'$ has been observed by LHCb [33], but the detected yield is still too small for performing CP violation measurements.

In this thesis the search for the $B_s^0 \rightarrow \eta'\phi$ decay mode is presented. The final state of this decay is CP-even, like for $B_s \rightarrow \eta'\eta'$. However, this advantage is diluted by the inefficiency in the reconstruction of the photon in the final state of the η' decay. While CP measurements are not possible at the moment with these modes, it is important to establish their existence and measure their branching fraction in view of future studies, when more data will be available. The decay $B_s^0 \rightarrow \eta'\phi$ has been studied theoretically in the framework of QCD factorisation [27, 37], perturbative QCD [38, 39], soft-collinear effective theory (SCET) [40], SU(3) flavour symmetry [41], and factorisation-assisted topological (FAT) amplitude approach [30]. The predictions for its branching fraction cover a range of three order of magnitudes, from 0.05×10^{-6} to 20×10^{-6} . All predictions have large uncertainties due to the limited knowledge

Conclusion

of form factors, the $\omega - \phi$ mixing angle, or penguin contributions.

The search for the $B_s^0 \rightarrow \eta' \phi$ is performed using the full Run 1 data sample of LHCb which includes 1 fb^{-1} of data collected at a centre-of-mass energy $\sqrt{s} = 7 \text{ TeV}$ in 2011 and 2 fb^{-1} of data collected at $\sqrt{s} = 8 \text{ TeV}$. The $B^+ \rightarrow \eta' K^+$ decay is used as normalisation channel in the computation of the branching fraction. The $B_s^0 \rightarrow \eta' \phi$ signal yield is obtained by performing a simultaneous two-dimensional fit of the reconstructed B and η' invariant mass distributions, for the events selected as $B_s^0 \rightarrow \eta' \phi$ and $B^+ \rightarrow \eta' K^+$ candidates. No significant signal is found. Using a Bayesian approach, an upper limit on the $B_s^0 \rightarrow \eta' \phi$ branching fraction is obtained:

$$\mathcal{B}(B_s^0 \rightarrow \eta' \phi) < 0.82 (1.01) \times 10^{-6} \quad \text{at 90\% (95\%) CL.}$$

This is the first upper limit set on the $B_s^0 \rightarrow \eta' \phi$ branching fraction. Although the theoretical predictions are characterised by large uncertainties, which make all of them compatible with the experimental result obtained from this analysis, the central values of the predictions in Refs. [39, 30] are significantly larger than the obtained upper limit. The result indeed favours the lower end of the range of predictions, and in particular seems to indicate an agreement with form factors consistent with the light-cone sum-rule calculations used for instance in Ref. [37], or with the hypotheses used in Refs. [27, 38]. The new stringent upper limit could therefore help constraining the theoretical models used in the prediction of branching fractions and CP asymmetries for hadronic charmless B decays. The results of this analysis are published by the LHCb collaboration in the Journal of High Energy Physics [1].

Many other interesting charmless B decays have or are expected to have very low branching fractions. For this reason these modes have been either not observed, or established with a small yield, using the dataset collected by LHCb during Run 1. In the case of $B_s \rightarrow \eta' \eta'$, the relatively high branching fraction is compensated by a low reconstruction efficiency. Additional statistics is crucial to increase the modest yields measured so far or to lead to first observations. With the start of the new data taking in 2015, LHCb has already collected $\sim 2 \text{ fb}^{-1}$ at $\sqrt{s} = 13 \text{ TeV}$, and $\sim 3 \text{ fb}^{-1}$ will be added by the end of 2018, to complete the Run 2 phase.

The last part of this thesis presents prospect studies for a few selected decays, using the available Run 2 data. Projections are made for the $B_s^0 \rightarrow \eta' \phi$, $B_s^0 \rightarrow \eta' \eta'$ and $B^+ \rightarrow \phi \pi^+$ decay modes. The latter is a strongly suppressed mode. A measurement of its decay rate is essential to test the Standard Model and to understand $\omega - \phi$ mixing. It has been searched for by LHCb using 2011 data, and an upper limit of 1.5×10^{-7} has been set at 90% confidence level [86].

Prospect studies for these decays are performed using the $B^+ \rightarrow \eta' K^+$ and $B^+ \rightarrow \phi K^+$ decay modes as normalisation channels. Using the large yields in data and the corresponding well known branching fractions, projections are made for the rarer decays. The studies show that the entire Run 2 data will be needed to repeat the search analyses for $B_s^0 \rightarrow \eta' \phi$ and $B^+ \rightarrow \phi \pi^+$, in order to increase the possibility of an observation, while the statistics collected at the end of Run 2 should allow the measurement of the B_s^0 effective lifetime with the $B_s^0 \rightarrow \eta' \eta'$. The projections are then extrapolated for the two following data-taking periods, Run 3 and Run 4, in which 50 fb^{-1} of data will be collected. Such statistics should allow a first time-dependent CP violation measurement with $B_s^0 \rightarrow \eta' \eta'$ decays.

Bibliography

- [1] LHCb collaboration, R. Aaij *et al.*, *Search for the $B_s^0 \rightarrow \eta' \phi$ decay*, JHEP **05** (2017) 1, arXiv:1612.08110.
- [2] LHCb collaboration, *LHCb Tracker Upgrade Technical Design Report*, Tech. Rep. LHCb-TDR-015, CERN-LHCC-2014-001, CERN, February 2014.
- [3] N. Cabibbo, *Unitary symmetry and leptonic decays*, Phys. Rev. Lett. **10** (1963) 531.
- [4] M. Kobayashi and T. Maskawa, *CP-violation in the renormalizable theory of weak interaction*, Prog. Theor. Phys. **49** (1973) 652.
- [5] L. Wolfenstein, *Parametrization of the Kobayashi-Maskawa matrix*, Phys. Rev. Lett. **51** (1983) 1945.
- [6] J. C. Hardy and I. S. Towner, *Superallowed $0^+ \rightarrow 0^+$ nuclear beta decays: A new survey with precision tests of the conserved vector current hypothesis and the Standard Model*, Phys. Rev. **C79** (2009) 055502, arXiv:0812.1202.
- [7] D. Poganic *et al.* *Precise measurement of the $\pi^+ \rightarrow \pi^0 e^+ \nu$ branching ratio*, Phys. Rev. Lett. **93** (2004) 181803, arXiv:hep-ex/0312030.
- [8] CCFR collaboration, A. O. Bazarko *et al.*, *Determination of the strange quark content of the nucleon from a next-to-leading order QCD analysis of neutrino charm production*, Z. Phys. **C65** (1995) 189, arXiv:hep-ex/9406007.
- [9] P. Vilain *et al.* *Leading-order QCD analysis of neutrino-induced dimuon events*, Eur. Phys. J. **C11** (1999) 19.
- [10] Belle collaboration, L. Widhalm *et al.*, *Measurement of $D^0 \rightarrow \pi l \nu (K l \nu)$ form factors and absolute branching fractions*, Phys. Rev. Lett. **97** (2006) 061804, arXiv:hep-ex/0604049.
- [11] CLEO collaboration, D. Besson *et al.*, *Improved measurements of D meson semileptonic decays to π and K mesons*, Phys. Rev. **D80** (2009) 032005, arXiv:0906.2983.
- [12] FlaviaNet working group on kaon decays, M. Antonelli *et al.*, *Precision tests of the Standard Model with leptonic and semileptonic kaon decays*, arXiv:0801.1817.

Bibliography

- [13] Particle Data Group, C. Patrignani *et al.*, *Review of Particle Physics*, Chin. Phys. **C40** (2016) 100001.
- [14] Belle collaboration, A. Zupanc *et al.*, *Measurements of branching fractions of leptonic and hadronic D_s^+ meson decays and extraction of the D_s^+ meson decay constant*, JHEP **09** (2013) 139, arXiv:1307.6240.
- [15] BaBar collaboration, P. del Amo Sanchez *et al.*, *Measurement of the absolute branching fractions for $D_s^- \rightarrow \ell^- \bar{\nu}_\ell$ and extraction of the decay constant f_{D_s}* , Phys. Rev. **D82** (2010) 091103, arXiv:1008.4080, [Erratum: Phys. Rev. **D91** (2015) 019901].
- [16] CDF collaboration, D. Acosta *et al.*, *Measurement of $B(t \rightarrow Wb)/B(t \rightarrow Wq)$ at the Collider Detector at Fermilab*, Phys. Rev. Lett. **95** (2005) 102002, arXiv:hep-ex/0505091.
- [17] D0 collaboration, V. M. Abazov *et al.*, *Precision measurement of the ratio $B(t \rightarrow Wb)/B(t \rightarrow Wq)$ and extraction of V_{tb}* , Phys. Rev. Lett. **107** (2011) 121802, arXiv:1106.5436.
- [18] CMS collaboration, S. Chatrchyan *et al.*, *Measurement of the single-top-quark t -channel cross section in pp collisions at $\sqrt{s} = 7$ TeV*, JHEP **12** (2012) 035, arXiv:1209.4533.
- [19] ATLAS collaboration, G. Aad *et al.*, *Measurement of the t -channel single top-quark production cross section in pp collisions at $\sqrt{s} = 7$ TeV with the ATLAS detector*, Phys. Lett. **B717** (2012) 330, arXiv:1205.3130.
- [20] C. Jarlskog, *Commutator of the quark mass matrices in the standard electroweak model and a measure of maximal CP nonconservation*, Phys. Rev. Lett. **55** (1985) 1039.
- [21] CKMfitter group, J. Charles *et al.*, *CP violation and the CKM matrix: Assessing the impact of the asymmetric B factories*, Eur. Phys. J. **C41** (2005) 1, arXiv:hep-ph/0406184, and updates available at <http://ckmfitter.in2p3.fr>.
- [22] P. Koppenburg and S. Descotes-Genon, *The CKM Parameters*, arXiv:1702.08834.
- [23] J. H. Christenson, J. W. Cronin, V. L. Fitch, and R. Turlay, *Evidence for the 2π decay of the K_2^0 meson*, Phys. Rev. Lett. **13** (1964) 138.
- [24] A. J. Buras, M. Jamin, M. E. Lautenbacher, and P. H. Weisz, *Effective hamiltonians for $\delta s = 1$ and $\delta b = 1$ non-leptonic decays beyond the leading logarithmic approximation*, Nucl. Phys. **B370** (1992) 69.
- [25] G. Buchalla, A. J. Buras, and M. E. Lautenbacher, *Weak decays beyond leading logarithms*, Rev. Mod. Phys. **68** (1996) 1125.
- [26] H.-n. Li and H.-L. Yu, *Perturbative QCD analysis of B meson decays*, Phys. Rev. **D53** (1996) 2480, arXiv:hep-ph/9411308.
- [27] M. Beneke and M. Neubert, *QCD factorization for $B \rightarrow PP$ and $B \rightarrow PV$ decays*, Nucl. Phys. **B675** (2003) 333, arXiv:hep-ph/0308039.

-
- [28] M. Beneke, *Soft-collinear factorization in B decays*, Nucl. Part. Phys. Proc. **261-262** (2015) 311, arXiv:1501.07374.
- [29] S. Cheng, A. Khodjamirian, and J. Virto, *B → ππ form factors from light-cone sum rules with B-meson distribution amplitudes*, arXiv:1701.01633.
- [30] S.-H. Zhou, Q.-A. Zhang, W.-R. Lyu, and C.-D. Lü, *Analysis of charmless two-body B decays in factorization assisted topological amplitude approach*, arXiv:1608.02819.
- [31] Belle and BaBar collaborations, A. J. Bevan *et al.*, *The physics of the B factories*, Eur. Phys. J. **C74** (2014) 3026, arXiv:1406.6311.
- [32] M. Beneke and M. Neubert, *Flavor singlet B decay amplitudes in QCD factorization*, Nucl. Phys. **B651** (2003) 225, arXiv:hep-ph/0210085.
- [33] LHCb collaboration, R. Aaij *et al.*, *Observation of the $B_s^0 \rightarrow \eta' \eta'$ decay*, Phys. Rev. Lett. **115** (2015) 051801.
- [34] LHCb collaboration, R. Aaij *et al.*, *Measurement of the $B_s^0 \rightarrow \phi\phi$ branching fraction and search for the decay $B^0 \rightarrow \phi\phi$* , JHEP **10** (2015) 053, arXiv:1508.00788.
- [35] LHCb collaboration, R. Aaij *et al.*, *Measurement of CP violation in $B_s^0 \rightarrow \phi\phi$ decays*, Phys. Rev. **D90** (2014) 052011, arXiv:1407.2222.
- [36] LHCb collaboration, R. Aaij *et al.*, *Measurement of CP violation and the B_s^0 meson decay width difference with $B_s^0 \rightarrow J/\psi K^+ K^-$ and $B_s^0 \rightarrow J/\psi \pi^+ \pi^-$ decays*, Phys. Rev. **D87** (2013) 112010, arXiv:1304.2600.
- [37] H.-Y. Cheng and C.-K. Chua, *QCD factorization for charmless hadronic B_s^0 decays revisited*, Phys. Rev. **D80** (2009) 114026, arXiv:0910.5237.
- [38] A. Ali *et al.*, *Charmless non-leptonic B_s decays to PP, PV and VV final states in the pQCD approach*, Phys. Rev. **D76** (2007) 074018, arXiv:hep-ph/0703162.
- [39] X.-f. Chen, D.-q. Guo, and Z.-j. Xiao, *$B_s^0 \rightarrow (\rho, \omega, \phi)\eta^{(\prime)}$ decays in the perturbative QCD approach*, arXiv:hep-ph/0701146.
- [40] W. Wang, Y.-M. Wang, D.-S. Yang, and C.-D. Lu, *Charmless two-body $B_{(s)} \rightarrow VP$ decays in soft collinear effective theory*, Phys. Rev. **D78** (2008) 034011, arXiv:0801.3123.
- [41] H.-Y. Cheng, C.-W. Chiang, and A.-L. Kuo, *Updating $B \rightarrow PP, VP$ decays in the framework of flavor symmetry*, Phys. Rev. **D91** (2015) 014011, arXiv:1409.5026.
- [42] F.-G. Cao, *Determination of the η - η' mixing angle*, Phys. Rev. **D85** (2012) 057501, arXiv:1202.6075.
- [43] C. Lefèvre, *The CERN accelerator complex. Complexe des accélérateurs du CERN*, <https://cds.cern.ch/record/1260465>, 2008.

Bibliography

- [44] LHCb collaboration, A. A. Alves Jr *et al.*, *The LHCb detector at the LHC*, JINST **3** (2008) S08005.
- [45] LHCb collaboration, *Production angle plot at 8 TeV*,
https://lhcb.web.cern.ch/lhcb/speakersbureau/bb_ProductionAngles.html.
- [46] LHCb collaboration, *LHCb Technical Proposal*, Tech. Rep. CERN-LHCC-98-004, CERN, March 1998.
- [47] LHCb collaboration, R. Aaij *et al.*, *Measurement of the b -quark production cross-section in 7 and 13 TeV pp collisions*, Phys. Rev. Lett. **118** (2017) 052002, arXiv:1612.05140.
- [48] LHCb collaboration, *LHCb integrated luminosity plot*,
<http://LHCb-public.web.cern.ch/LHCb-public/Images2016/LumiAll.png>.
- [49] LHCb collaboration, R. Aaij *et al.*, *LHCb detector performance*, Int. J. Mod. Phys. **A30** (2015) 1530022, arXiv:1412.6352.
- [50] LHCb collaboration, *LHCb detector public page*,
<http://LHCb-public.web.cern.ch/LHCb-public/en/detector/Detector-en.html>.
- [51] B. Storaci, *Optimization of the LHCb track reconstruction*, J. Phys. Conf. Ser. **664** (2015) 072047.
- [52] LHCb collaboration, R. Aaij *et al.*, *Measurement of the track reconstruction efficiency at LHCb*, JINST **10** (2015) P02007, arXiv:1408.1251.
- [53] A. Papanestis and C. D'Ambrosio, *Performance of the LHC RICH detectors during the LHCb Run II*, Nucl. Instrum. Meth. **A** (2017) , arXiv:1703.08152.
- [54] LHCb RICH group, M. Adinolfi *et al.*, *Performance of the LHCb RICH detector at the LHC*, Eur. Phys. J. **C73** (2013) 2431, arXiv:1211.6759.
- [55] LHCb collaboration, S. Amato *et al.*, *LHCb calorimeters: Technical Design Report*, Tech. Rep. LHCb-TDR-002, CERN-LHCC-2000-036, CERN, September 2000.
- [56] A. A. Alves, Jr. *et al.*, *Performance of the LHCb muon system*, JINST **8** (2013) P02022, arXiv:1211.1346.
- [57] F. Archilli *et al.*, *Performance of the Muon Identification at LHCb*, JINST **8** (2013) P10020, arXiv:1306.0249.
- [58] LHCb collaboration, M. Ferro-Luzzi, *The LHCb trigger strategy and performance*, eConf **C0304052** (2003) FO003, arXiv:hep-ex/0306051.
- [59] V. V. Gligorov, C. Thomas, and M. Williams, *The HLT inclusive B triggers*, Tech. Rep. LHCb-PUB-2011-016, CERN-LHCb-PUB-2011-016, CERN, September 2011.

-
- [60] LHCb collaboration, B. Sciascia, *LHCb Run 2 trigger performance*, PoS, **BEAUTY2016** (2016) 029.
- [61] S. Benson, V. Gligorov, M. Vesterinen, and M. Williams, *The LHCb Turbo Stream*, J. Phys. Conf. Ser. **664** (2015) 082004.
- [62] G. Barrand *et al.*, *Gaudi — a software architecture and framework for building hep data processing applications*, Comput. Phys. Commun. **140** (2001) 45 .
- [63] T. Sjöstrand *et al.*, *An introduction to PYTHIA 8.2*, Comput. Phys. Commun. **191** (2015) 159, arXiv:1410.3012.
- [64] A. Ryd *et al.*, *EvtGen: A Monte Carlo Generator for B physics*, , <http://evtgen.warwick.ac.uk>; D. J. Lange, *The EvtGen particle decay simulation package*, Nucl. Instrum. Meth. **A462** (2001) 152.
- [65] P. Golonka and Z. Was, *PHOTOS Monte Carlo: A precision tool for QED corrections in Z and W decays*, Eur. Phys. J. **C45** (2006) 97, arXiv:hep-ph/0506026.
- [66] GEANT4 collaboration, S. Agostinelli *et al.*, *GEANT4: A Simulation toolkit*, Nucl. Instrum. Meth. **A506** (2003) 250.
- [67] LHCb collaboration, *LHCb Trigger and Online Upgrade Technical Design Report*, Tech. Rep. LHCb-TDR-016, CERN-LHCC-2014-016, CERN, May 2014.
- [68] LHCb collaboration, *LHCb VELO Upgrade Technical Design Report*, Tech. Rep. LHCb-TDR-013, CERN-LHCC-2013-021, CERN, November 2013.
- [69] LHCb collaboration, *LHCb PID Upgrade Technical Design Report*, Tech. Rep. LHCb-TDR-014, CERN-LHCC-2013-022, CERN, November 2013.
- [70] W. D. Hulsbergen, *Decay chain fitting with a Kalman filter*, Nucl. Instrum. Meth. **A552** (2005) 566, arXiv:physics/0503191.
- [71] B. P. Roe *et al.*, *Boosted decision trees, an alternative to artificial neural networks*, Nucl. Instrum. Meth. **A543** (2005) 577, arXiv:physics/0408124.
- [72] F. Pedregosa *et al.*, *Scikit-learn: Machine learning in Python*, J. Mach. Learn. Res. **12** (2011) 2825, see also <http://scikit-learn.org>.
- [73] M. Pivk and F. R. Le Diberder, *sPlot: A statistical tool to unfold data distributions*, Nucl. Instrum. Meth. **A555** (2005) 356, arXiv:physics/0402083.
- [74] G. Punzi, *Sensitivity of searches for new signals and its optimization*, eConf **C030908** (2003) MODT002, arXiv:physics/0308063.
- [75] S. S. Wilks, *The large-sample distribution of the likelihood ratio for testing composite hypotheses*, Ann. Math. Stat. **9** (1938) 60.

Bibliography

- [76] LHCb collaboration, *PIDCalib packages*,
<https://twiki.cern.ch/twiki/bin/view/LHCb/PIDCalibPackage>.
- [77] LHCb collaboration, *L0 hadron trigger efficiency*, <https://twiki.cern.ch/twiki/bin/viewauth/LHCbPhysics/CalorimeterObjectsToolsGroupDOC>.
- [78] J. Wess and B. Zumino, *Consequences of anomalous ward identities*, Phys. Lett. **B37** (1971) 95.
- [79] M. Benayoun *et al.*, *Anomalous η/η' decays: the triangle and box anomalies*, Eur. Phys. J. **C31** (2003) 525.
- [80] V. Belyaev, V. Egorychev, E. Govorkova, and D. Savrina, *Study of π^0/γ reconstruction efficiency*, Tech. Rep. CERN-LHCb-INT-2014-045, CERN, March 2015.
- [81] LHCb collaboration, *LHCb tracking efficiencies*,
<https://twiki.cern.ch/twiki/bin/view/LHCb/LHCbTrackingEfficiencies>.
- [82] J. Prisciandaro, *Study of charmless $B_{(s)}$ meson decays involving η' and ϕ intermediate states at the LHCb experiment*, PhD Thesis n°6493, Ecole Polytechnique Fédérale de Lausanne, January 2015.
- [83] LHCb collaboration, R. Aaij *et al.*, *Measurement of the fragmentation fraction ratio f_s/f_d and its dependence on B meson kinematics*, JHEP **04** (2013) 001, arXiv:1301.5286, f_s/f_d value updated in LHCb-CONF-2013-011.
- [84] W. Verkerke and D. Kirkby, *The RooFit toolkit for data modeling*, eConf **C0303241** (2003) MOLT007, arXiv:physics/0306116.
- [85] K. S. Cranmer, *Kernel estimation in high-energy physics*, Comput. Phys. Commun. **136** (2001) 198, arXiv:hep-ex/0011057.
- [86] LHCb collaboration, R. Aaij *et al.*, *Measurement of the charge asymmetry in $B^\pm \rightarrow \phi K^\pm$ and search for $B^\pm \rightarrow \phi \pi^\pm$ decays*, Phys. Lett. **B728** (2014) 85, arXiv:1309.3742.
- [87] Y. Li, C.-D. Lu, and W. Wang, *Revisiting $B \rightarrow \phi \pi$ decays in the Standard Model*, Phys. Rev. **D80** (2009) 014024, arXiv:0901.0648.
- [88] M. Gronau and J. L. Rosner, *B decays dominated by $\omega - \phi$ mixing*, Phys. Lett. **B666** (2008) 185, arXiv:0806.3584.
- [89] LHCb collaboration, R. Aaij *et al.*, *Measurement of $\sigma(pp \rightarrow b\bar{b}X)$ at $\sqrt{s} = 7$ TeV in the forward region*, Phys. Lett. **B694** (2010) 209, arXiv:1009.2731.
- [90] LHCb collaboration, R. Aaij *et al.*, *Production of J/ψ and Y mesons in pp collisions at $\sqrt{s} = 8$ TeV*, JHEP **06** (2013) 064, arXiv:1304.6977.

-
- [91] J. Prisciandaro, F. Blanc, and O. Schneider, *Search for $B_s^0 \rightarrow \eta' \eta'$ decays and measurement of the charge asymmetry in $B^\pm \rightarrow \eta' K^\pm$ and $B^\pm \rightarrow \phi K^\pm$ decays*, CERN-LHCb-ANA-2014-062, CERN, June 2014.
- [92] LHCb collaboration, R. Aaij *et al.*, *Measurement of the $B_s^0 \rightarrow \mu^+ \mu^-$ branching fraction and effective lifetime and search for $B^0 \rightarrow \mu^+ \mu^-$ decays*, Phys. Rev. Lett. **118** (2017) 191801, arXiv:1703.05747.
- [93] LHCb collaboration, I. Bediaga *et al.*, *Framework TDR for the LHCb Upgrade: Technical Design Report*, Tech. Rep. LHCb-TDR-12, CERN-LHCC-2012-007, CERN, April 2012.
- [94] LHCb collaboration, R. Aaij *et al.*, *A new algorithm for identifying the flavour of B_s^0 mesons at LHCb*, JINST **11** (2016) P05010, arXiv:1602.07252.
- [95] LHCb collaboration, R. Aaij *et al.*, *Measurement of the CP-violating phase ϕ_s in $\bar{B}_s^0 \rightarrow J/\psi \pi^+ \pi^-$ decays*, Phys. Lett. **B736** (2014) 186, arXiv:1405.4140.
- [96] LHCb collaboration, R. Aaij *et al.*, *Measurement of the CP-violating phase ϕ_s in $\bar{B}_s^0 \rightarrow J/\psi \pi^+ \pi^-$ decays*, Phys. Lett. **B713** (2012) 378, arXiv:1204.5675.
- [97] LHCb collaboration, R. Aaij *et al.*, *Expression of Interest for a Phase-II LHCb Upgrade: Opportunities in flavour physics, and beyond, in the HL-LHC era*, Tech. Rep. CERN-LHCC-2017-003, CERN, February 2017.

Sebastiana Gianì

Curriculum Vitae

Ch. de la Combe, 4
1131 Tolochenaz, Switzerland
☎ +41 (0)76 6244734
✉ sebastiana.giani@alumni.epfl.ch

EDUCATION

- 2017 **Ph.D. in Particle Physics**, under the supervision of Prof. O. Schneider and Dr F. Blanc, EPFL, Lausanne, Switzerland.
Title of the thesis: "Search for the $B_s^0 \rightarrow \eta' \phi$ decay and prospects for the study of selected charmless B decays at LHCb".
- 2012 **Master Degree in Physics**, University of Catania, Italy.
Title of the thesis: "Study of the properties of the fragments emitted in $^{64}\text{Ni} + ^{124}\text{Sn}$ and $^{58}\text{Ni} + ^{112}\text{Sn}$ nuclear reactions at 35 AMeV using the 4π detector CHIMERA".
Final grade: 110/110 cum laude.
- 2009 **Bachelor Degree in Physics**, University of Catania, Italy.
Title of the thesis: "Study of global variables for heavy-ion reactions at Fermi energy".
Final grade: 110/110 cum laude.

WORK EXPERIENCE

- 2013-2017 **Ph.D. student**, EPFL, Switzerland.
- I led a full analysis in the field of b physics at the LHCb experiment. I was responsible for each step of the analysis from the data skimming to statistical interpretation and publication. The results are published in a paper by a major journal. Furthermore I developed prospect studies for several decay modes, exploiting the possibility for future measurements at LHCb.
 - Editor of all the documentation for my analyses (internal notes and paper).
 - Collaborated to the R&D studies for the development of a scintillating fibre tracker for the LHCb upgrade. I contributed to the characterisation of the first silicon photomultiplier prototypes and I realised a fast simulation used to predict the detector behaviour in different conditions.
 - Trigger Liaison, acting as a go-between for the charmless physics working group and the trigger group of LHCb.
 - Teaching and assistant duties: laboratory assistant (3 semesters), assistant for particle physics lectures (3 semesters).
- 2013 **Short-term employee**, INFN, Catania, Italy.
Contribution to the the development of the FARCOS detector.
- 2011-2012 **INFN scholarship for master students**, Laboratori Nazionali del Sud, Catania, Italy.
Initiation to scientific research, within the CHIMERA collaboration.
- 2009-2010 **Laboratory assistant**, University of Catania, Italy.

COMPUTER SKILLS

Operating systems
Linux, Mac OS, Windows

Software Office, OpenOffice, Photoshop, GIMP, Latex, Adobe Acrobat
VCS Git
Programming Python, C, C++
Languages
Ability to use Machine Learning algorithms and concepts

SCIENTIFIC SCHOOLS

CHIPP PhD winter school 2015, *Grindelwald, Switzerland, January 2015.*

CONFERENCES

SPS - OPG 2017, *Geneva, Switzerland, August 2017.*

Talk presented: "Charmless hadronic B decays at LHCb: results and prospects".

LHCC 2017, *Geneva, Switzerland, February 2017.*

Poster presented: "Search for the $B_s^0 \rightarrow \eta' \phi$ decay at LHCb".

CKM 2016, *Mumbai, India, December 2016.*

Talk presented: "Results from LHCb in quasi-two-body charmless B meson decays".

SPS 2016, *Lugano, Switzerland, August 2016.*

Talk presented: "Search for the $B_s^0 \rightarrow \eta' \phi$ decay at LHCb".

SELECTED PUBLICATIONS

LHCb collaboration, R. Aaij et al., "Search for the $B_s^0 \rightarrow \eta' \phi$ decay", **JHEP 05** (2017), arXiv:1612.08110.

S. Gianì, on behalf of the LHCb collaboration, "Results from LHCb in quasi-two-body charmless B meson decays", **PoS(CKM2016)**, 107.

S. Gianì, G. Haefeli, C. Joram, M. Tobin and Z. Xu, "Digitization of SiPM signals for the LHCb Upgrade SciFi tracker", LHCb-PUB-2014-025.

LANGUAGES

English	Proficient User	<i>C1</i>
French	Independent User	<i>B2</i>
Italian	Mother tongue	

INTERESTS

Reading, cooking, music, volunteering

